3D printing of microfluidic chips with different modules for point-of-care testing applications

Ojha, A.

Award date:
2019

3D printing of Microfluidic Chips with different modules for Point-of-Care testing Applications

Master Thesis Final Report

Submitted by:
Akshit Ojha, 1276018

TU/e Supervisor
Dr. J.M.J Den Toonder

Fontys Supervisors
Dr. Jan Bernards and Dr. Karel Planken

Abstract

POC diagnostics is becoming a really promising real world application for microfluidic devices. Microfluidic platforms program small-amount of liquid to execute a bio-protocol, this can literally shift a whole lab onto a device. Microfluidic capillary systems employ surface tension effects which are dominant at micro-scale to manipulate the flow of liquids, and thus they are self-powered and self-regulated. This property of passively transporting the liquid to different locations on the device can be used for fabricating a microfluidic device used for POCT applications. With advancement in 3D printing technologies highly complex microfluidic devices can be fabricated via a single-step, rapid, and cost-effective protocols, making microfluidics more accesible to users.

This thesis illustrates that liquid flow can be manipulated with simple geometrical variations, different microfluidic elements like transport microchannels, flow resistors, stop valves, delay valves, meniscus trigger valves, soft valves and phaseguides are designed, fabricated and tested with experiments. These experiments illustrate that with simple variation in geometry which is easily possible with 3D printing, microfluidic elements can be made and with combining these elements a capillary circuit can be built similar to an electronic circuit. The design freedom and uniform features with lesser deviation from design for microfluidic features along with the advantage of batch printing makes 3D printing technology a promising fabrication technique for future use in the microfluidics field. For this project the microfluidic devices are fabricated with Objet30 Pro printer by Stratasys Ltd. (USA), a polyjet printer with high resolution and transparent Veroclear resin.

Preface

This is the final project report for the Master's Graduation Project. The project is a joint collaboration between Fontys University of Applied Science and Eindhoven University of Technology. This project is carried out under the RAAK-pro funded project "Printing Makes Sense". The project is carried in supervision of Dr. J.M.J Den Toonder (Chair Microsystems Research Group, TU/e), Dr. Jan Bernards (Lector Thin Films Department, Fontys University of Applied Science) and Dr. Karel Planken (Thin Films Department, Fontys University of Applied Science). In this report the aim of the project along with introduction, background theory, materials and method, results obtained and discussion followed by conclusion and recommendations are explained with the project workflow and adopted approach. I would like to thank my colleagues Harm Visscher, Emma Moonen and Matthijs Boidin for having countless brainstorming sessions and helping me out whenever needed. Moreover, I want to thank Dr. Jan Bernards for making the equipment available and guiding me with adopting the best approach. Dr. Karel Planken for his endless feedback sessions and motivation to strive for better results in the smartest way possible and lastly my TU/e mentor Dr. J.M.J Den Toonder for understanding my interests, approach and guiding me to exhibit the results in the most insightful way.

Abbreviations used: POC = Point-of-care
POCT= Point=of-care testing
LOC= Lab-on-a-chip

PDMS= Polydimethylsiloxane
SLA= Stereolithography

Contents

Chapter 1

Introduction

1.1 About the project:

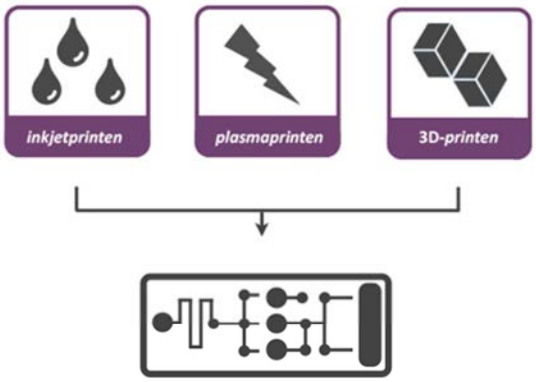

Figure 1.1: Printing Makes Sense- The project involves use of different printing techniques under one goal

The aim of the Master's Graduation project is to fabricate a Microfluidic device using 3D printing technology for Point-of-Care testing application and to develop a proof-of-concept for integrating a Microfluidic toolbox on the device itself and to test various microfluidic functionalities like microchannels for passive transport, passive valves, delay channels, phaseguides etc. The device is to be used in future for measuring the antibody concentration in blood plasma with the help of biological sensors (LUMABS system) which change their configuration in the presence of an antibody resulting in a shift of emitted wavelengths [1](Arts et al, 2017). The working is explained in detail in the section A.1.

Microfluidic devices have been gaining a lot of importance in Point-of-Care Testing projects because of its numerous advantages. In a nutshell, the aim of the project would be to fabricate a microfluidic device using 3D printing with different microfluidic elements that can potentially be used for one-step immunoassay. The functionality of the microfluidic elements need to be tested and validated

so that further researchers can use different functions for different applications.

The first chapter comprises of the introduction in which the use of microfluidic devices for POCT applications is given along with insight into various advantages and applications of 3D printed microfluidic devices. In the next chapter 2 the background theory helpful in understanding working of various microfluidic modules is explained in brief. The materials and methods chapter 3 explains the experimental setup, designs used for experiments along with the fabrication of devices. The printing material, model liquid, sealants along with the approach adapted for designing the devices is explained in chapter 3. The results are shown in chapter 4, these results are analysed and discussed in brief. The report ends with deriving a conclusion for this project along with recommendations for improvements in future.

1.2 Lab-on-Chip devices for Point of Care Testing (POCT)

Lab-on-a-Chip (LOC) technology aims to miniaturize laboratory measuring techniques. These miniaturization techniques have great advantages like the need of smaller sample sizes, less reagents, high throughput, portability and inexpensive chips (Daniel Mark et al, 2010 [5]). These properties are quite beneficial for Point-of-Care applications, which is a technique used to do medical diagnosis and therapeutic drug monitoring in an environment outside the laboratory (S.Mukherji et al,2017 [4]). The main idea of POCT is to decentralize the laboratories and to do on the spot measurement of disease antibodies in the body using biomarkers or protein cells [6](Mitra.D, 2013). The most critical parameter for getting accurate results on the minimized scale is the technique used for detections. Since, the devices are portable and to be used at e.g. home or at doctor's office so the detection should be done with an inexpensive general equipment like a smartphone. The signals generated due to biochemical reactions between the disease antibodies and the biological sensor protein can be detected optically where the camera can record the change in the optical properties [1]-[3]. This would be better as no other expensive sensors need to be incorporated into the device and this would simplify the device a lot.

1.3 Microfluidic Toolbox for POCT applications

At the micro-scale the surface forces dominate and effect the wetting property of the solid. The flow at micro-scales is laminar as the Reynolds number, $R_e \leq 2300$. The Reynolds number is given as:

$$R_e = \frac{\rho u L}{\mu}$$

Where, μ = dynamic visosity of the fluid, ρ = density of the fluid, L= the characteristic length and u= velocity of the fluid with respect to an object.
For a common scenario in microfluidic devices with water as the fluid moving forward with velocity 1cm/s in a rectangular channel of Hydraulic diameter (D_h)=$2.5e^{-4}m$ will give R_e=2.8. This indicates that at micro-scale the viscous forces dominate and the inertial forces are negligible. The liquid is driven forward by the capillary pressure developed at the liquid-air interface.
Passive microfluidics circumvent the need for peripheral equipment and exploit the surface energy

effects to move the liquid through the system, thus requiring minimal user interventions. Research papers by Delamarche and colleagues [30] and by Juncker et al [31] show the application of self-filling autonomous capillary systems with different microfluidic elements joined together to form a capillary circuit used for measuring antibody concentration in blood plasma. The ideal devices to conduct immunoassays and POC diagnostics would only require single manipulation being the addition of sample to complete the assay; this is called one-step immunoassay. The liquid driven by capillary forces can be manipulated with different microfluidic elements. The driving pressure can be changed by abruptly changing the geometry or by introducing a hydrophobic patch (Delamarche et al [32]) to create a pressure barrier which will prevent the liquid-air interface to advance further. Flow resistors decrease the flow velocity of the liquid and can be used to incubate the antibodies with the biological sensor or for chemical reactions to occur between the reagents and the sample liquid. Similarly other features for timing the liquid flow and to pin the liquid at a certain position for a specific time can be done with liquid-triggered microvalves as discussed later in sections 2.2.3 and 4.5. So, with changes in the driving capillary pressure, the hydraulic resistance and area of the liquid-air interface the flow can be manipulated, this manipulation can be done with simple changes in the geometry of the microfluidic paths. These phenomenons are described in the theory chapter 2 and the results studied in chapter 4.

1.4 3D printed microfluidic devices

Microfluidic devices are tiny chips that perform chemical, biological etc analyses of very small (in μLs) volumes of fluids like blood, saliva, river-water etc. Microfluidic devices have enabled a wide range of biochemical and clinical applications, such as cancer screening, micro-physiological system engineering, high-throughput drug testing, and point-of-care diagnostics. 3D printers are used as manufacturing tool for wide variety of applications be it diagnosis, implants or external prostheses. With the continuously improving resolution, the design freedom, easy interface, availability of 3D CAD design software, low cost, mass manufacturing and new materials, 3D printing has become accessible manufacturing tool in bioanalytical research laboratories. The parts can be printed with different materials with varying density, stiffness, opacity and chemical properties. 3D printed microfluidic devices have been successfully used for recapturing tumour cells [25] and to detect neurochemical changes in human brain [27]. Using 3D printing fabrication techniques, the alteration of design features is significantly faster and easier as compared with the traditional fabrication methods. Biocompatible resins for 3D printing are now available that, contrary to PDMS (Polydimethylsiloxane), feature very low drug absorption and are thus very good material candidates for building complex 3D organ-on-a-chip systems in the future. Highly fluorinated perfluoropolyether (PFPE) methacrylates were used for making photopolymer used for 3D printing of transparent and chemically-resistant microfluidic devices [40]. These advances will make microfluidic technology more accessible to researchers in various fields and will accelerate innovation in the field of microfluidics [33]. 3D printed Biosensor Arrays have been successfully tested by Sharafeldin et al [34], an article by Macdonal et al. [35] compares the performance of the microfluidic devices printed with different 3D printing platforms.

Demand for inexpensive prototyping and fabrication of lab-on-a-chip (LOC) devices has stimulated the need to seek for alternative fabrication methods. In this regard, Additive manufacturing (3D printing) has attracted interest within the LOC community, which aims to reduce the cost and

complexity of prototyping and developing bespoken devices. In a review [26], it was documented that the cost to fabricate a batch of complex microfluidic particle separator was under eleven pounds and another article [35] showed that for devices made with an economical 3D printer the cost can be around 0.1 USD only. 3D printing does not require a cleanroom environment and offers to shrink the time between design to device to an hour or less. Rogers et al [37] demonstrates a 3D printed microfluidic device with integrated valves. Channel sizes of $350\mu m$ width by $250\mu m$ depth were printed successfully using an economical 3D priter. In the article by Castro et al [41], $200\mu m$ thick membrane with $25\mu m$ layers was printed with a SLA 3D printer used as a porous membrane barrier in microchannels . With latest development in 3D printing with CLIP (Continous Liquid Interface Production) printing, 2-photon printing and advancements in Stereolithography printing the resolution has gone from micro-scale to nano-scale. An article by Gowers et al [38] shows that rigid and soft-material can be printed simultaneously to print different features for the microfluidic device used for online analysis of subcutaneous human microdialysate. In the article by Van Den Driesche et al [39], microfluidic chip-holders with reliable electrical and fluidic connections were fabricated with 3D printing. This development trend indicates that in coming future a lot of potential applications would be explored using 3D printed microfluidic devices.

Chapter 2

Theory

2.1 Capillary flow

Capillary microfluidics can deliver liquids in a pre-programmed way without using additional equipment like digital pumps etc. The fluid is transported by exploiting the surface tension effects, these effects depend on the geometry and the surface chemistry of the microchannels. Self-filling capillary microfluidics that use negative capillary pressure for fluid flow and regulation has been discussed (Y. Zhu et al,2009 [10]). The key parameters which govern the capillary flow are discussed in this chapter.

2.1.1 Wettability and Contact Angle

Young's Law

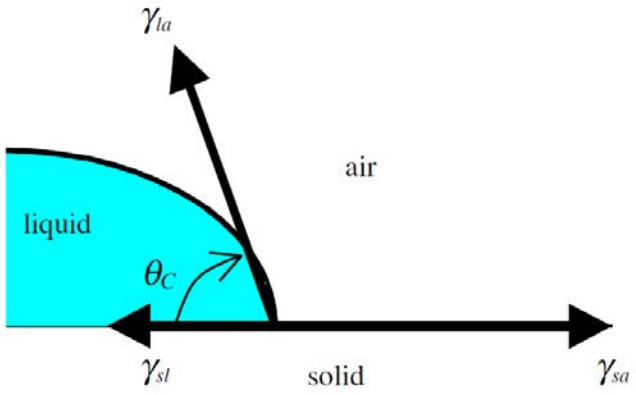

Figure 2.1: Liquid droplet on solid surface

In the figure 2.1, the three surface tensions namely γ_{la},γ_{sa} and γ_{sl} at the three interfaces are shown. The equilibrium contact angle θ_c made by the liquid droplet balances these forces as-

$$\gamma_{sa} = \gamma_{la} cos\theta_c + \gamma_{sl} \tag{2.1}$$

In equation 2.1, γ_{la},γ_{sa} and γ_{sl} are the forces acting at the liquid-air, solid-air and solid-liquid interface. A surface is considered wetting if the contact angle with the liquid is less than 90°, the material is then considered hydrophilic and in this case the adhesive forces between the liquid-solid interface are higher than the cohesive forces between the liquid-liquid interactions. A surface having contact angle more than 90° with a liquid is considered hydrophobic and this means that the cohesive forces between the liquid molecules are higher than the adhesive forces between the liquid-solid interface. Microchannels with wettable surfaces generate a concave liquid-air interface and a negative capillary pressure which drives the flow forward into the microchannels (wicking effect). Similarly, non-wettable surfaces form a convex liquid-air interface which develops positive capillary pressure pushing liquid out of the Microchannel. From equation 2.1 it can be interpreted that hydrophilic surfaces will have $\gamma_{sa} > \gamma_{sl}$. Though this equilibrium contact angle shown as θ_c above is different from the advancing contact angle but for simplicity in measuring contact angles and modelling the pressures, flow rate and meniscus position over time the two angles (equilibrium and advancing) are approximated to be same. This is done because the calculation of the pressures is done using the cosine term of the angles as shown in equation 2.6 later, the difference in cosine values for small differences in angles is minute. So for convenience $\theta_e \approx \theta_c$. In the equations θ_c is the advancing contact angle but when contact angle measurements are taken on printed parts and top sealant the equilibrium contact angle is taken as the advancing contact angle (θ_c).

2.1.2 Surface Energy of a capillary microchannel

When a liquid enters a capillary microchannel through the reservoir it wicks in the channel due to the capillary pressure being developed in the system which drives the liquid-air interface forward. This phenomenon can be explained with the energy changes taking place as derived by Man et al. (1998) [15]:

$$U_T = A_{sl}\gamma_{sl} + A_{sa}\gamma_{sa} + A_{la}\gamma_{la} \tag{2.2}$$

Here U_T is the total energy of the system, A_{sl} is the solid-liquid wetted area, A_{sa} is the area on the solid covered by air and A_{la} is the complicated area of the liquid-air interface. In figure 2.2, these symbols for the surface tensions and the area are depicted. In figure 2.2, A_X denotes the area covered by the liquid which will increase over time due to the advancement of the liquid-filling front. It should be noted that the total area of the system will remain constant. Hence, $A_{sl} + A_{sa} = A_T$. Thus, the total surface energy of the system as shown in equation 2.2 reduces to:

$$U_T = U_o - A_{sl}\gamma_{la} cos\theta_c \tag{2.3}$$

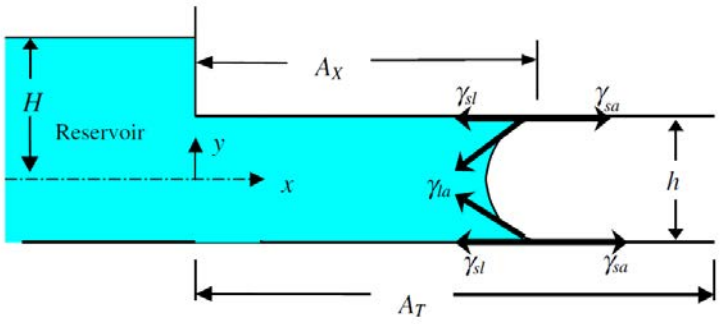

Figure 2.2: different interfaces in a capillary microfluidic channel

2.1.3 Capillary Pressure-

The Young-Laplace equation describes the relation between the contact angle, Microchannel size, surface tension of the liquid and the capillary pressure (Jean Berthier et al, 2014 [8]). This capillary pressure is the difference in pressures between points at different lengths of the Microchannels and thus is referred to as the pressure drop. This pressure drop in terms of the derivative of the surface energies (dU_T) with respect to the injected volume change (dV_l) is given as:

$$\Delta P = \frac{-dU_T}{dV_l} \tag{2.4}$$

Using the relation from 2.3 in the above equation,

$$\Delta P = -\gamma_{la}(cos\theta_c \frac{\partial A_{sl}}{\partial V_l} - \frac{\partial A_{la}}{\partial V_l})$$

In uniform hydrophilic channels as mentioned earlier $\gamma_{sa} > \gamma_{sl}$, A_{sa} is minimized and A_{sl} increases with time as the meniscus advances forward with the capillary force. Thus, the liquid wets more area of the solid substrate.
Since, rectangular Microchannels are common with the fabrication techniques so an equation depicting the relation between the capillary pressure drop depending upon the contact angles, dimensions of the rectangular Microchannel and the surface tension of the liquid using the relations given by David Juncker et al.(2018) [7] and Y. Zhu et al.(2009) [10] which is derived from the laplace pressure equation

$$\Delta P = -\gamma_{la}(\frac{1}{R_1} + \frac{1}{R_2}) \tag{2.5}$$

From equation 2.5 the pressure drop generated in the rectangular microchannel is derived as shown below in equation 2.6 where $R_1 = \frac{h}{\cos\theta_t} + \frac{h}{\cos\theta_b}$ and $R_2 = \frac{w}{\cos\theta_l} + \frac{w}{\cos\theta_r}$.

$$\Delta P = -\gamma_{la}[\frac{[\cos\theta_t + \cos\theta_b]}{h} + \frac{[\cos\theta_l + \cos\theta_r]}{w}] \tag{2.6}$$

ΔP = The Capillary Pressure difference over the channel length

θ_t = The angle made by fluid with the top surface

θ_b = The angle made by fluid with the bottom surface

θ_r = The angle made by fluid with the right edge surface

θ_l = The angle made by fluid with the left edge surface

γ_{la} = The surface tension of the fluid

h = The height of the rectangular microchannel

w = The width of the rectangular microchannel

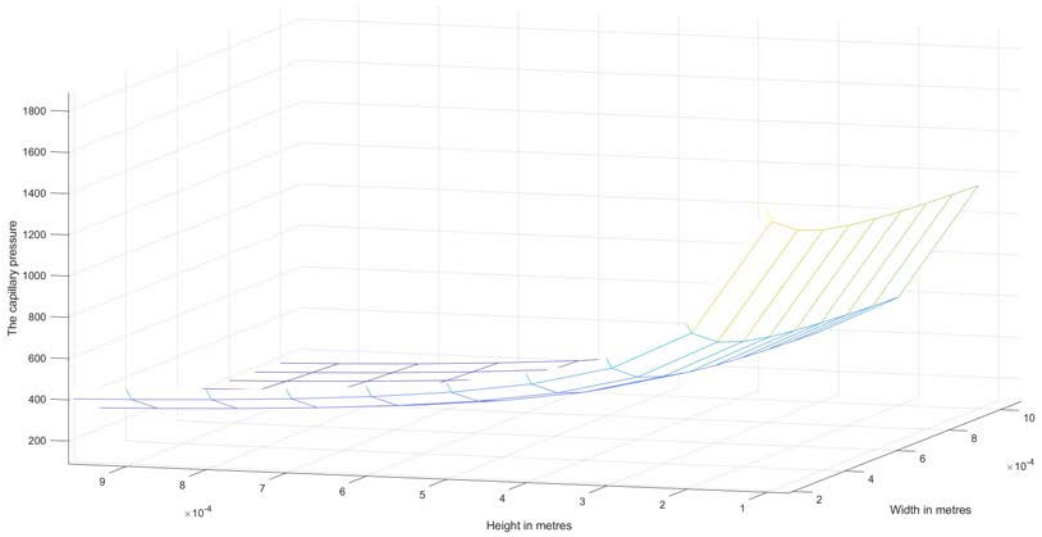

Figure 2.3: Capillary pressure with respect to height and width of the microchannel

Figure 2.3 shows the dependence of the capillary pressure drop in rectangular microchannels on the aspect ratio (height/width), high aspect ratios (height/width) lead to more pressure drop which enhances the flow.The plot is obtained using water as fluid with contact angle 40° at all surfaces. Pressure drop at z-axis, width at x-axis and height at y-axis. The graph shows that narrower channels (with less width) have maximum negative pressure which would enhance the capillary flow. The contact angle should be significantly less than 90°, to enhance the flow in microchannels. For the proper tapping of the capillary pressure and making the liquid meniscus progress evenly the device material should be uniform to ensure that the flow does not behave abnormally anywhere in the microchannel. For the case of shallow microchannels, the fluid flow is driven primarily by interaction of liquid between the top and the bottom surfaces. If the top surface is made of PDMS(Polydimethylsiloxane) which is hydrophobic and the Microfluidic device is made of glass (hydrophilic) then this may lead to stoppage of the flow in case of low aspect ratios (shallow channels). Similarly, there is also a concept of corner flow which will be discussed later. Capillary pressure developed in narrow channels is higher compared to wider channels of the same depth but it may be noted that the hydraulic resistance is much more for narrow channels and hence, the

flow rate decreases making the liquid progress slowly in narrow channels. The expressions for the hydraulic resistance and flow rate are given later in equations 2.8-2.10.

It is always a desired property to have the contact angle of the wetted surface less than 60° for better flow speeds (Arman Javadi et al, 2013 [11]).

2.1.4 Corner Flows and Concus-Finn condition

If the material is super hydrophilic having a contact angle less than 45°, then the fluid tends to travel faster at the interfaces (e.g. left and bottom, right and bottom etc.). Corner flow becomes significant at low contact angles (between $0 < \theta < 30°$) and can significantly precede bulk flow in the microchannel depending on channel aspect ratio. A phenomenon where the liquid is absorbed more by the solid surface causing an enormous increase in volume called surface imbibition is observed for contact angles approaching 0°. These effects could result in deviations from the pressure predicted in the Young–Laplace equation for capillary pressure which is described above in equation 2.4. To avoid this problem the edges have to be made rounder. Corner flow leads to air bubble inclusions as the fluid flow is not uniform and there are voids due to difference of fluid speeds on top, bottom and the edges. Hence, corner flow is not a desired feature for Microfluidic devices but is quite hard to counter with conventional fabrication techniques. Advanced fabrication techniques like SLA 3D printing would be best suited to counter this problem as straight edges become rounder due to stray light affect. Any voids in the channels or chambers might lead to air bubble inclusions which are undesired properties. Proper sealing is also a factor that comes into play when the phenomenon of corner flows is inspected. Most of the times in microfluidic devices the sealing material is different as compared to the device material and hence, the top contact angle θ_{top} is different.

2.1.5 Flow rate and Distance travelled by liquid interface

The flow rate is a crucial parameter to consider when designing the capillary circuits as it determines the flow time and also which dimensions of the Microchannel would be best suited for transporting the fluid passively. For laminar, steady state flows and in the absence of gravitational effects the flow rate Q of liquid in rectangular channels is given by Juncker et al.(2018) [7] as:

$$Q = \frac{h^3 w \Delta P}{12 \eta L} * [1 - \sum_{n,odd}^{\infty} \frac{1}{n^5} * \frac{192}{\pi^5} \tanh(\frac{n\pi w}{2h})] \tag{2.7}$$

Q = The Flow rate of the fluid in microchannels

h = The height of the microchannels

w = The width of the microchannels

ΔP = The Capillary Pressure Difference

η = The Kinematic viscosity of the fluid

L = The length of Microchannels

The simplified form of the expression 2.7 is given by taking the consideration $\tanh h/w \approx h/w$, at small scales.

$$Q = \frac{h^3 w \Delta P}{12\eta X(t)} * [1 - 0.63\frac{h}{w}] \tag{2.8}$$

Here X(t) is the distance travelled by the liquid interface which is a function of time. The Hydraulic resistance of the channel is given by:

$$R = \frac{1}{\eta}\frac{\Delta P}{Q} \tag{2.9}$$

$$R = \frac{12X(t)}{h^3 w(1 - 0.63\frac{h}{w})} \tag{2.10}$$

The simplified form for the travelling distance X(t) as given by Zhu et al.(2009) [10] that will be used to compare the experimental results given in chapter 4 is:

$$X(t)^2 = a_0 \frac{r^2 \Delta P t}{8\mu} \tag{2.11}$$

here, $a_0 = \frac{64}{\pi^4}(1 - \frac{2h}{\pi w}\frac{tanh\pi w}{2h})$,$r = \frac{wh}{w+h}$, ΔP is the capillary pressure derived from equation 2.6 and μ = viscosity of the liquid. This equation is different from the one obtained earlier for calculating the flow rate of the channel.
This has the classic square root relationship between filled length and time first described by Washburn (1921),[24]. These results are also verified with a different approach using the force balance equation which is very well described in the paper by John Ralston et al [6].

2.1.6 Flow resistors

For dissolution and controlled release of reagents a flow resistor network proves handy in timing the liquid interface advancement in a capillary network containing delay structures. Meandering channels which are a combination of straight and curved channel paths are used for this purpose. Microchannels with high hydraulic resistance depicted in equation 2.10 are used. Narrow channels have more resistance and hence, the flow rate is less. In meandering channels the curved profile has more pressure losses due to continuous bending and dragging of the liquid making the flow rate slower. Flow resistor structures can be used in parallel microchannels where the flow is split into two paths namely the fast channel with low hydraulic resistance (R_{fast}) and the other with delay structures having higher hydraulic resistance (R_{slow}). This network can be used for triggering the pinned meniscus at the valve as discussed later in chapter 4 which will prove to be beneficial for timing the dissolution, mixing and for incubating the analyte mixture for POCT applications as described by B.Eker et al.[16]. Figure 2.4 shows a meandering flow resistor capillary channel fabricated with PDMS (Polydimethylsiloxane) used for mixing two liquids.

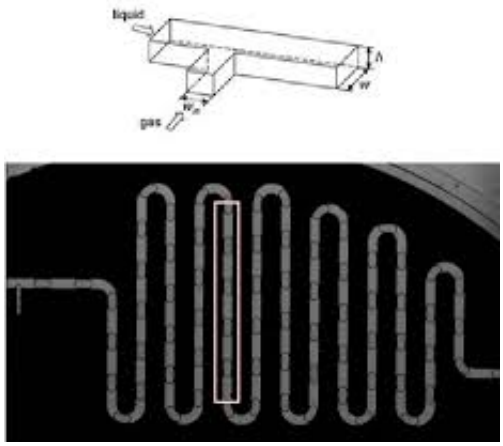

Figure 2.4: Meandering microchannels used as flow resistors. Fabricated with PDMS

2.2 Capillary Valves

Passive valves have proven to be really important feature in microfluidic devices as an abrupt change in geometry of the flow path is used to delay or stop the liquid filling front. In microfluidic systems,valves are significant to control the release of reagents, chemical reactions and sequencing and timing of bio/chemical analyses.Passive valves are easy to fabricate with rapid prototyping techniques and hold promise to control the route of the liquid in complicated microfluidic channel networks without any external actuation.

2.2.1 Pressure Difference across the liquid meniscus

As, given in the paper by Hasang Cho et al. [17] the pressure difference across the liquid meniscus, ΔP is derived from the laplace equation 2.5.

$$\Delta P = P_i - P_o = \gamma(\frac{1}{R_1} + \frac{1}{R_2})$$

Here, P_i= is the internal pressure in the microsystem and P_o is the external pressure outside the system. The liquid is driven forward due to this negative pressure difference. R_1 and R_2 are radii of curvatures of the liquid-air interface.

The large enlargement of the flow path makes it energetically unfavorable for the liquid meniscus to advance forward into the wider region. As, the liquid-air interface area increases as the meniscus reaches the expansion shown in figure 2.5, contact angle increases from θ_c to $\theta_c + \beta$ (Man et al.1998 [15]). This develops a positive pressure barrier that needs to overcome for the liquid filling front to advance forward into the wider channel/chamber. As shown in figure 2.5, the area of advancing liquid-air interface increases when it reaches an expansion in both depth and width. The contact angle transitions from θ_c to $min(\theta_c + \beta, 180°)$ over different transition phases. At x=L(expansion)

the pinning pressure is given as:

$$\Delta P_{pin} = -\gamma_{la} * [\frac{[\cos\theta_t + \cos\theta_b]}{h} + \frac{[\cos(\theta_l + \beta) + \cos(\theta_r + \beta)]}{w}] \tag{2.12}$$

When this positive pressure is overcome by applying an external pressure into the system or by a trigger mechanism, the liquid advances into the diverging channels (X>L). The pressure difference upon the valve bursting at the post-pinned state ($X > L$) is given as:

$$\Delta P = -\gamma_{la} * [\frac{[\cos\theta_t + \cos\theta_b]}{h} + \frac{[\cos(\theta_l + \beta) + \cos(\theta_r + \beta)]}{W}] \tag{2.13}$$

Here, β is the expansion angle and W is the width of expansion. In figure 2.5 given below a geometrical expansion where the depth of the channel is abruptly increased. The liquid meniscus pins at the expansion and the phenomenons observed are as shown in figure 2.6. In figure 2.6, w=width of the channel, β=expasnion angle and W=width of the expansion after channels diverge fully.

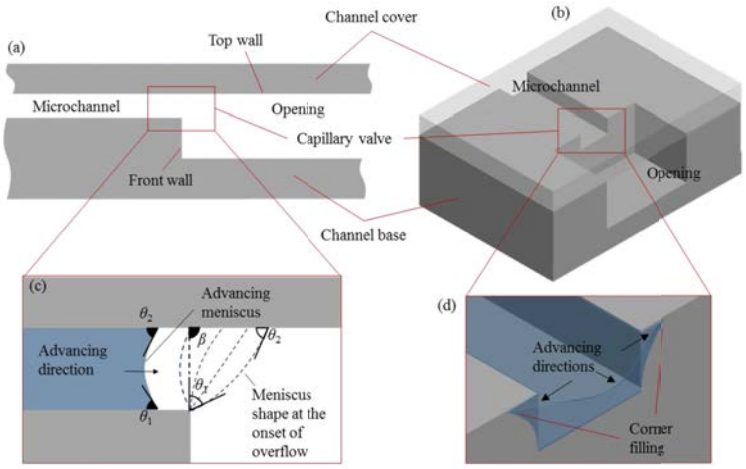

Figure 2.5: Liquid meniscus at the geometrical expansion, courtesy Yildirim et al. (2016) [23]

Figure 2.6 shows the three phenomenons observed at the geometrical expansion where the microchannel expands from width w to width W.

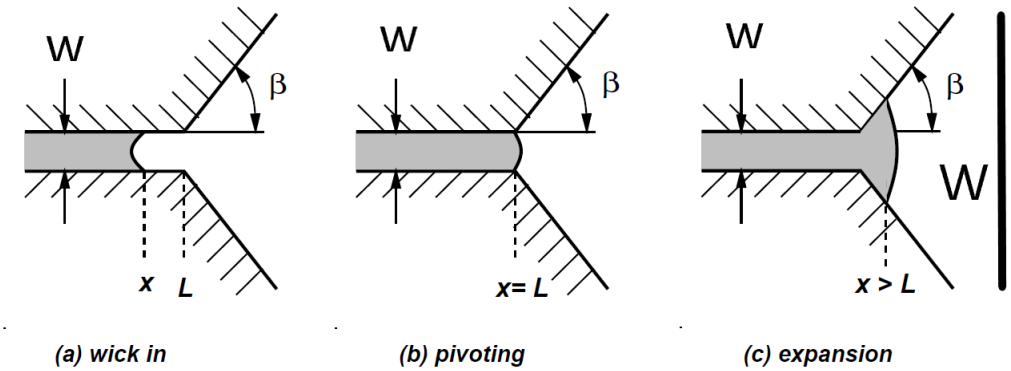

Figure 2.6: Wicking, pivoting and expansion of the liquid meniscus when it reaches an abrupt geometrical expansion, source Man et al.(1998) [15]

2.2.2 Soft valve trigger

As mentioned above the working principle of a capillary valve is based on the wetting properties and dimensions of the microchannel that strongly influence the driving capillary pressure. The abrupt expansion of geometry induces a pressure barrier that pins the liquid front. Thin elastomeric or stretchable membranes used as sealants can be used to trigger the pinned liquid meniscus to advance further into the expansion. Pressing the top of the valve using a PDMS puncher or the tip of a pen reduces the pressure barrier and the liquid can proceed. This is well documented and a lot of publications have documented this phenomena as done by Martina Hitzbleck and Emmanuel Delamarche (2013) [18] and figure 2.7 shows this phenomena.

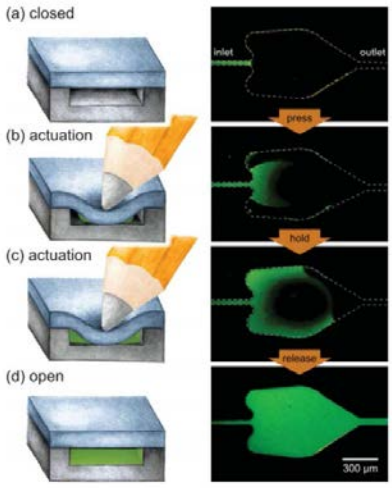

Figure 2.7: actuation of soft valve, courtesy Hitzbleck et al. (2013), [18]

2.2.3 Meniscus trigger with parallel flow paths

Liquid-triggered liquid microvalving allows one liquid sample to pin at one location and wait for the other sample to arrive and trigger the pinned interface. The two liquids then merge and advance together. By designing a parallel flow path where the liquid is initially split into two channels one being fast with lesser hydraulic resistance (R_f) and the other having meandering time delay paths integrated with higher hydraulic resistance (R_s) is used. The liquid filling front in the fast channel pins at a microvalve which is a geometrical expansion and then waits for the liquid advancing slowly in the slow channel. This phenomenon is critical for mixing of reagents in a microfluidic device, especially if mixing time is equivalent to the reaction or incubation time. Bubble-free merging of the liquids is important for avoiding channel blockage without altering the internal geometry of the device. This is well documented by Melin (2004) [19] and B.Eker et al.[16]. The most significant property of using liquid-triggered liquid microvalves is that it does not require any external actuation technique and the flow in the microfluidic device can be timed and controlled. In figure 2.8, the pinned liquid waits for the liquid advancing through the meandering channels. The liquid then triggers the pinned interface and then the two liquids merge and advance together.

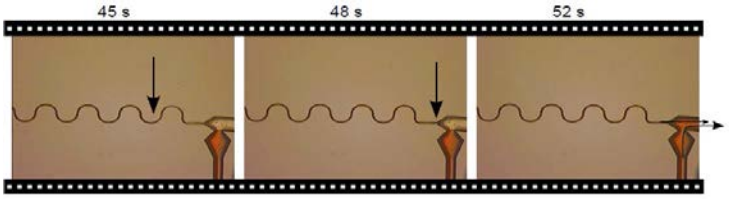

Figure 2.8: Meniscus trigger microvalve using two parallel flow paths, Courtesy B.Eker et al. [16]

2.3 Phaseguides

To step-wise control the progress of the liquid-air interface, stripes in the surface are patterned. These act as pressure barriers and can be placed perpendicular or aligned at a certain angle to the advancement direction of the liquid-air interface. These stripes/ridges guide the flow of the liquid and hence, are named as pressure barriers [20]. An advancing liquid meniscus aligns itself along the phaseguide and remains in that position till sufficient pressure is build up to overcome the pinning pressure of the phaseguide structure. The liquid overflows at the weakest point as explained by Yildirim et al (2014) [22]. The angle between the phaseguide ridge and the side-wall α decides the weakest point where the liquid will overflow once this pressure is built up. This pressure barrier as investigated by Garbarino et al for $\alpha = 90°$ and different ridge angles β as shown in figure 2.9. (2017) [21] can be calculated as:

$$P_{pin} = -\gamma(2\frac{\cos\theta_c}{w} + \frac{\cos(min(\theta_c + \beta, 180°)) + \cos\theta_{top}}{H - h}) \tag{2.14}$$

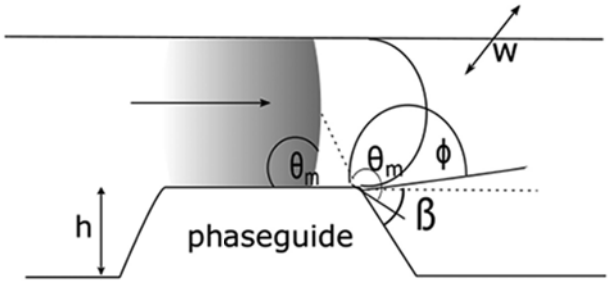

Figure 2.9: Parameters determining the burst pressure of a phaseguide with angle β

As, seen in equation 2.14 the pinning pressure depends on the phaseguide ridge angle β and the height of the phaseguide ridge. These phaseguide ridges come handy for detection and reaction chambers where the liquid needs to be guided to pin at a certain position where optical or chemical detections need to be done which is quite common scenario in POCT microfluidic devices.

2.4 Surface Energy of solid and Wetting Envelope

The surface energy of a liquid is identical to its surface tension, and a variety of techniques exist to measure the liquid surface tension. However, the surface energy of a solid is calculated from a set of liquid/solid contact angles,developed by bringing various liquids in contact with solid. This is shown in earlier in section 2.1.1. The relation between these terms using a force balance in an equilibrium state is given by the Young-Laplace equation which is as follows as shown in equation 2.1.

However, determining the Interfacial Surface Energies of the Solid-Liquid interface is hard. The Owens/Wendt Theory (a two component model for solid surface energy) was developed to account for specific (Polar type) interactions between the solid surfaces and liquids. In this theory the surface energy of the solid is envisioned as being comprised of two components- a dispersive component and a polar component (Kruss Scientific,1999 [13]). The dispersive component is due to the Vander Waal interactions (London Forces) which are the forces between a like molecules. The Polar component is bonded due to the ionic interactions as the molecules are charged or obtain charge. The forces are dipole-dipole, dipole-induced dipole, hydrogen bonding, and other site-specific interactions which a surface is capable of having with deposited liquids.

Mathematically, the theory is based on two fundamental equations which describe between the three interfaces given in Zisman et al,1964 [12].

$$\sigma_{SL} = \sigma_S + \sigma_L - 2(\sigma_L^D \sigma_S^D)^{1/2} - 2(\sigma_L^P \sigma_S^P)^{1/2} \tag{2.15}$$

Using the equation 2.15 and the relation obtained from the previous equation **??**, the simplified equation looks like:

$$\sigma_L \frac{(\cos\theta + 1)}{2(\sigma_L^D)^{1/2}} = (\sigma_S)^{1/2} \frac{(\sigma_L^P)^{1/2}}{(\sigma_L^D)^{1/2}} + (\sigma_S^D)^{1/2} \tag{2.16}$$

This equation is used to calculate the Polar and Dispersive components of the surface energy of the solid. Using the reverse relation a wetting envelope is plotted which determines from the properties of the liquid (The Polar and Dispersive Surface Tensions) whether it would fully wet the surface or not. This will be prove to be a good approximation for selecting a suitable substrate for the microfluidic devices needed for testing specific liquids whose polar and dispersive surface tension component values will be known. With advancement in coating techniques the surface can also be modified for increasing its wetting properties.

Chapter 3

Materials and Methods

3.1 Fabrication of devices using 3D printing

With latest developments in Additive Manufacturing and a lot of research being done for adapting new techniques having better resolution, it is possible to print intricate features onto a chip at Micro and even Nano scale. The layer-by-layer creation of solid objects using the sliced images from a CAD file is a promising approach for fabricating microfluidic devices. Accessible and portable print technologies and availability of material that can exhibit diverse mechanical and optical properties make additive manufacturing (AM) practical for many applications in MEMS and Microfluidic systems sector.([25] [26]). The advantages it offers over conventional microfluidic devices made from PDMS (Polydimethylsiloxane) are:

- Wide range of materials
- Multi-material features
- Monolithic devices (no assembly needed)
- High robustness and stiffness. The channel walls do not collapse or deform under pressure
- Batch printing enables many microfluidic devices to be printed at once

One of the technologies which has been successfully tapped for printing microfluidic 'Lab on a Chip' devices is 'SLA (Stereolithography) 3D Printing'. With this printing technique it was possible to successfully print microchannels $50\mu m$ deep and $150 - 200\mu m$ wide, Beckwith et al (2018) [25]. These dimensions would be ideal to transport the sample fluid to various chambers for detection and analysis, however this needs to be verified both experimentally and theoretically. The other printing technique which is also the one used in this project for fabricating microfluidic devices is Polyjet printing. These, print techniques are explained in brief next.

SLA (Stereolithography) 3D printing A UV lamp projected onto the resin VAT containing photopolymeric resin selectively polymerizes the uncured(liquid) resin into a solid device. Unlike other printing techniques there are no line like features on the surfaces which would hinder the flow of the fluid. Thus, the finishing of SLA printing is quite fine. The materials used for printing are

acrylate photopolymeric resins which are readily available. Biocompatibel resins are also manufactured by Resin Manufacturers and the printed products can be made more hydrophilic with surface treatments.

PolyJet printing involves jetting a photopolymer using linearly arranged nozzles, then spraying Micro-droplets onto the build surface, where the material is polymerized using an integrated UV light source. Voids in the model are filled with a support material, which is removed with post-treatment after the printing process has been completed. The soluble support gets dissolved in an alkaline solution ($2-4\%w/v$ NaOH solution). The advantages, limitations, errors in dimensions, print orientations etc. for parts printed with Objet30 have been explained in section B in the appendix. The microfluidic devices were designed in Solidworks 2018, CAD software and the STL (standard triangular language) file was converted and sent to OBJET30 printer. The Objet Studio software was used to position and orient the print jobs on the printer bed. This has been explained in section B. The parts are optically transparent and the accuracy in attaining the desired dimensions is quite well with $6-10\%$ error (deviation from design) in the microfluidic channel and chamber widths. It was also observed that the trapped resin in printed microfluidic channels with width less than $200\mu m$ was hard to clear from some areas so the channels were clogged. So, for experiments channel width was kept above $300\mu m$(lower limit for channels). In article by Samper et al. (2019) [27] monolithic objet30 prints were used as microfluidic devices for POCT application. Microchannels of $150\mu m$ depth and $130\mu m$ width were successfully printed and the trapped resin was later removed with the help of a $50\mu m$ diameter tungsten wire along with immersion of prints in an $2-4\%$ w/v alkaline NaOH solution. The print quality ,orientations and the resolution of the printer are explained briefly in sections B.1, B.3 and B.4.

3.1.1 Surface Treatment of prints

The parts printed with Objet30 Pro are made with VeroClear resin (refer B.1). The contact angle measurements on parts printed with VeroClear material were recorded with Dataphysics OCA-30 measurement setup. Only the first instantaneous measurements were taken, as the contact angle decreased over time due to the droplet spreading on the surface indicating that the surface is rough and the drop cannot stabilise (refer B.4.1). The average contact angle of VeroClear material with water is 74.5° with a standard deviation of 3.65°. Though material is Hydrophilic ($\theta_c < 90^\circ$) but for fast transport and more wetting of the solid surface with the liquid $\theta_c \leq 60^\circ$ is desired. Here θ_c is the contact angle of the liquid with the solid. It should be noted that from theory in section 2.1.1, the angle in that instance is the equilibirum contact angle θ_e which is different from the advancing contact angle θ_c. However, the variation in the cosine of the angles which is used to calculate the driving capillary pressure for the liquid-air interface as shown in equation 2.6 is very minute so the two values are taken to be same. This will be discussed in the later sections chapter 4 and 5.

Treatment: Since the VeroClear material is similar to PMMA (B.1) the coatings used on PMMA for making it Hydrophilic can be used on VeroClear parts as well. A Batch of Pluronic-F127 coating is prepared by mixing 4g of Pluronic F-127 powder (Sigma-Aldrich,USA) with 40ml of De-ionized water using a vortex mixer. The printed parts are immersed in this Pluronic Solution. The contact angles were measured after treating the printed parts for different time periods. In figure 3.1, the

contact angle of Water (De-mineralized) on VeroClear with Pluronic treatment done for 2-hours and 2-days is shown along with contact angles on untreated VeroClear part.

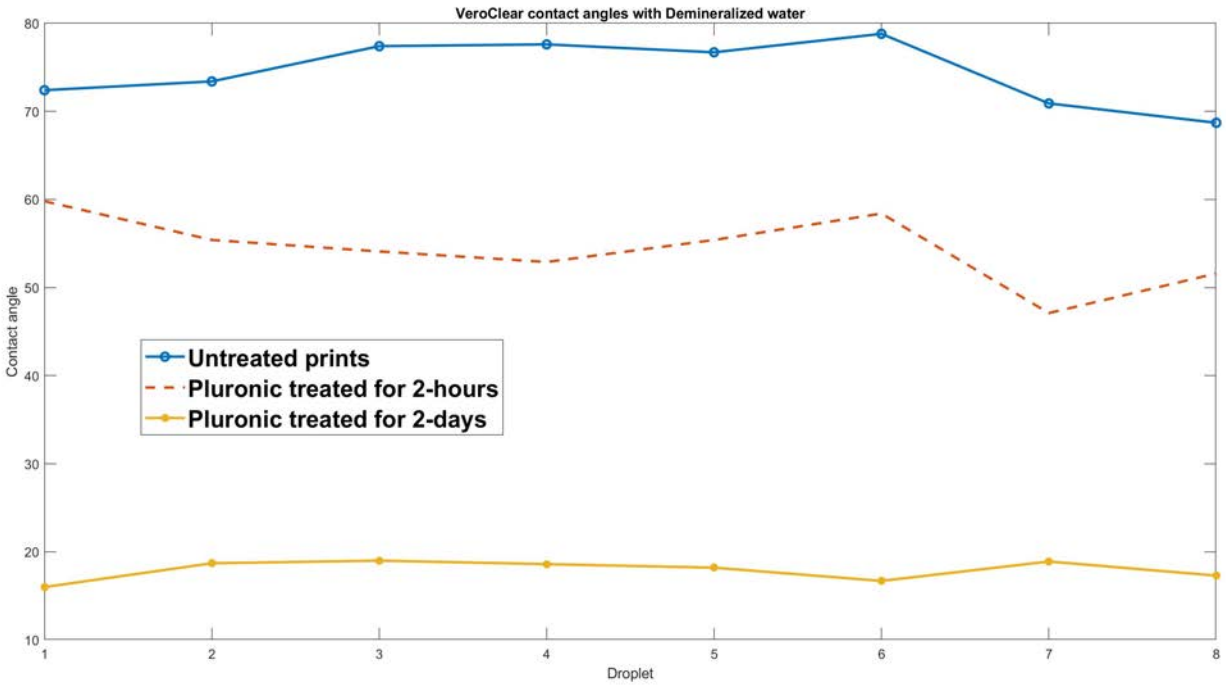

Figure 3.1: Contact angle of demineralized water on Veroclear parts. The three curves represent untreated, treated for 2-hours and treated for 2-days with Pluronic coating.

The average contact angle of water on VeroClear parts after dipping the parts in Pluronic solution for 2-hours is 54.3° with a standard deviation of 4° and when treated with Pluronic for 2-days the contact angle becomes 17.9° with a standard deviation of 1°. It is also observed that the droplets are really stable on the pluronic coated VeroClear parts and the contact angle does not decrease over time as was the case for untreated parts (refer B.4.1).

Wetting Envelope for VeroClear The wetting envelopes for Pluronic treated VeroClear for 2-days and untreated VeroClear were plotted. The theory behind this is given in section 2.4, using equations 2.15 and 2.16 a MATLAB program is used to plot the envelopes as shown in figure 3.2. The two fluids De-ionized water and Diiodomethane (Sigma-Aldrich,99%) are used for this purpose as we know the polar and dispersive components of surface tension for them (refer section 2.4). The figure 3.2 shows the comparison between the full wetting curve of treated Veroclear and untreated Veroclear material. The span of the treated VeroClear material is much bigger than the untreated material.

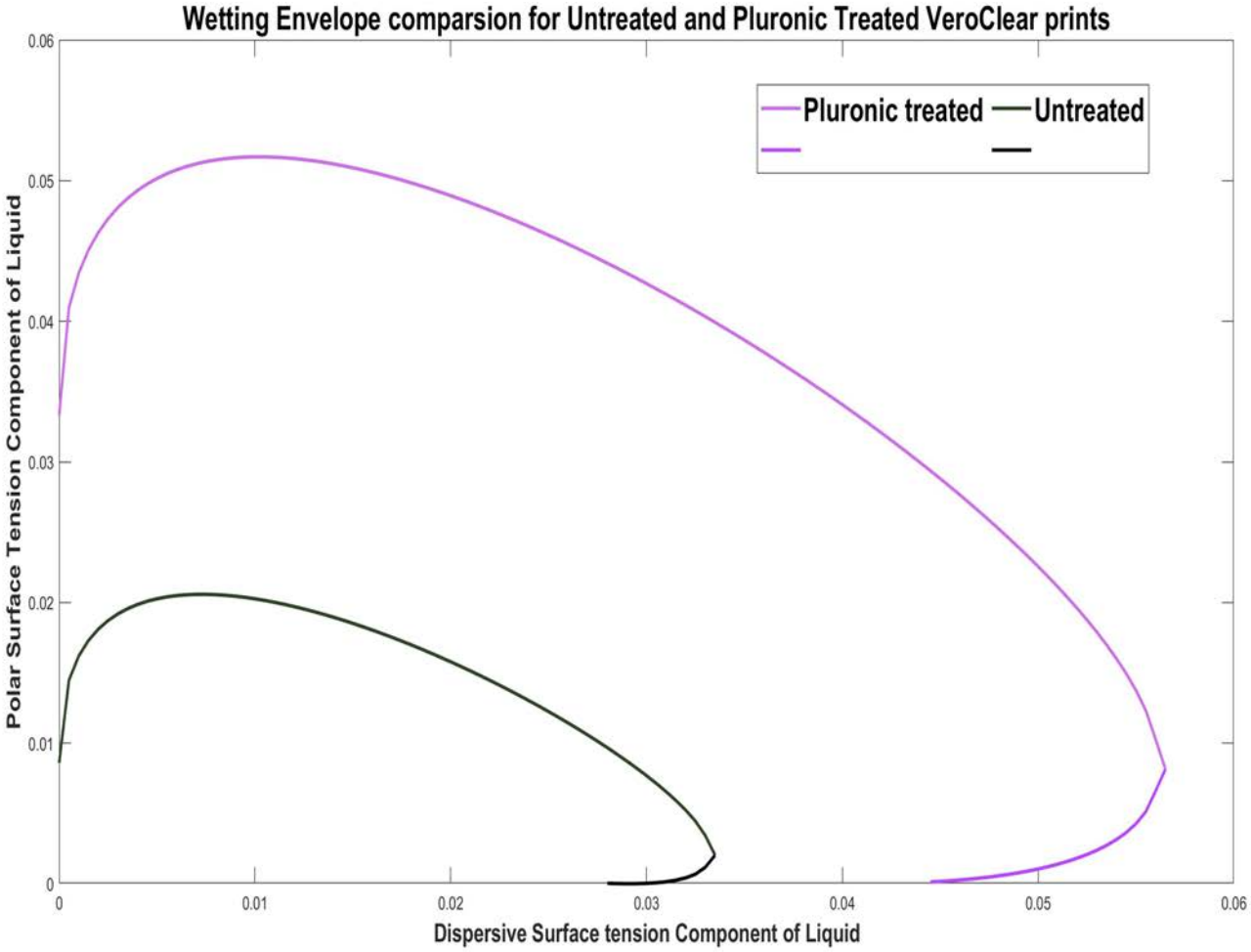

Figure 3.2: Full wetting Curve ($\theta_c = 0$) for Treated and untreated Veroclear

3.2 Model Fluid

Water mixed with a dye is used as model fluid for conducting the experiments. 3g of Methyl Violet B base 85% dye is mixed with $500ml$ of Deionized water to prepare the solution. Contact angle measurements using Dataphysics OCA-30 are recorded on the VeroClear surface treated with pluronic F-127 coating as discussed in section B.4. The angles obtained are sown in table 3.1: The average contact angle on Pluronic treated VeroClear material is 20.4° with a standard deviation of 2.34°. It should be noted that the average contact angle measured here is the equilibrium contact angle (θ_e) and not the advancing contact angle (θ_c), however for theoretical calculations θ_e is taken equal to θ_c as the variation in the cosines of these angles used for calculating the developed capillary pressure using equation 2.6 is quite less.

Table 3.1: Contact angles with VeroClear prints

Droplet no.	Contact Angle
1	18.8°
2	18.4°
3	23.8°
4	21.6°
5	23.8°
6	19.9°
7	18.8°
8	18.3°

3.3 Sealing

The printed devices are kept open since the reagents are to be incorporated into the device for POCT applications where the detection would be a one step process where the model fluid is just inserted and after sometime the signals/results can be obtained. So, the reagents are incorporated in the device after printing and to avoid leakage and contamination a proper sealant is required. Different methods were used to assemble the open microfluidic device with a cover-plate. Figures 3.3b and 3.3a show the designs for the microfluidic device and the cover-plate which are bolted together, similarly figures 3.3c and 3.3d show the designs which are bonded together using double-sided tape.

(a) Microfluidic device for bolting

(b) Cover Plate for bolting

(c) Microfluidic device bonded with double-sided tape

(d) Cover-plate bonded with double-sided tape

As, leakage was observed for devices which were sealed using mechanical bolts and that by using double-sided tape as seen in figures 3.4a and 3.4b, so a new method involving selective curing of the cover plate with the microfluidic device was used.

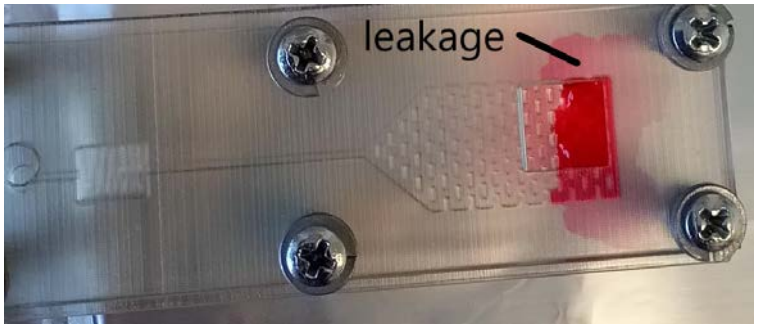

(a) leakge in bolted assembly

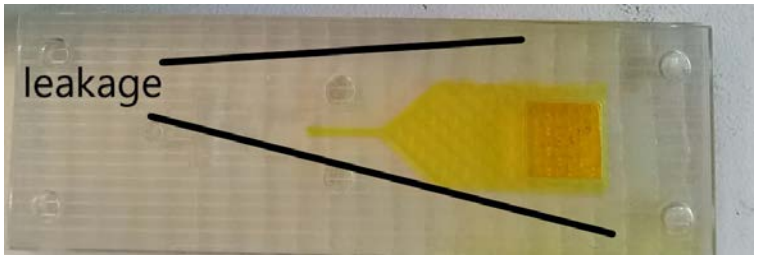

(b) leakage in double-sided taped assembly

Figure 3.4: leakage in the devices

Unpolymerized liquid veroClear resin was used as sealant to bond the coverplate with the microfluidic device. The cover was smeared with unpolymerized liquid VeroClear resin with the help of a flat spatula on the edges and then is aligned and put on top of the microfluidic device. The assembly is then put in a UV treatment box for approximately 90 minutes at $35°C$. As, seen in figure 3.5 the device is sealed with the help of selective UV curing using the acrylic VeroClear resin. However, for small volumes this didn't prove to be a reliable method as microchannels were clogged with the resin as it escaped into the openings which upon UV exposure solidifies, completely blocking the channels. Also with the UV exposure, the colour of the devices changes. A yellow tint is observed on the device which is not desired as the devices need to be optically transparent for proper optical detection as done in various POCT devices. Over-curing also causes some unwanted deformation and warpage creating residual stresses in the device, this would hamper the uniform fluid flow in the devices, so the idea of sealing with selective UV curing did not prove to be promising.

Figure 3.5: UV cured binding of cover-plate with the device

Well plate tape A rather simple method for sealing the devices with an optically transparent sealant was that of using a well plate tape. This tape was used to cover and seal the microfluidic devices used for experiments in chapter 4. The tape is transparent, hydrophobic, biocompaible, pressure sensitive and inert. The contact angle on the sticky part of the tape with the model fluid as explained above in 3.2 is recorded with DataPhysics OCA-30 equipment. Due to the limitation of the printer, the edges of the rectangular microchannel become curved due to the stray light effect. Due to this the well plate does not stick properly on the top edges of the channel giving rise to small voids. When the fluid flow is studied it is observed that the fluid enters the voids and this is also considered as one of the reasons for the error between theoretical predictions and experimental results. This is discussed in results and discussion chapter 4. The well plate tape is a simple solution for covering and sealing the device because of its transparency and biocompatibility which is a desired property for device usend in POCT applications. This tape is used for sealing the devices tested in chapter 4. Table 3.2 shows the contact angle of the water-dye micture on the sticky part of the tape. Figure 3.6 shows the droplets on tape after contact angle measurements with OCA-30 by DataPhysics.

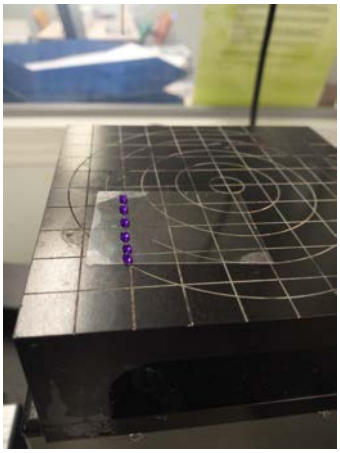

Figure 3.6: Droplets on Well plate tape (sticky part)

Table 3.2: Contact angle on well plate tape

Droplet no.	**Contact Angle**
1	120.1°
2	120.4°
3	112.8°
4	112.4°
5	117.8°
6	117.2°
7	120.6°
8	119.9°

The average contact angle obtained is 117.65° with standard deviation of 3.35°.

3.4 Design of Microfluidic Elements

In this section the various designs used for testing the microfluidic features are explained. The devices are fabricated with Objet30 Pro 3D printer and designed with Solidworks ,2018 software.

3.4.1 Flow in rectangular Channels

In figure 3.7, a rough estimation of the meniscus position of the liquid with respect to time when flowing in a rectangular microchannel having different widths ($300\mu m$, $500\mu m$, $600\mu m$ and $800\mu m$) and a constant depth of $500\mu m$ is predicted. The liquid modelled is a water-dye solution (refer section 3.2), with contact angle taken as $\theta_c = 20.4°$ with VeroClear material on 3-sides (left,right and bottom) and $\theta_{tape} = 117.6°$ with the top sealing tape (refer section 3.3). This rough prediction

is done considering the model fluid used for experiments (refer chapter 4) which is a water-dye fluid (refer section 3.2). The angles taken for this experiment are also shown in section 3.2.

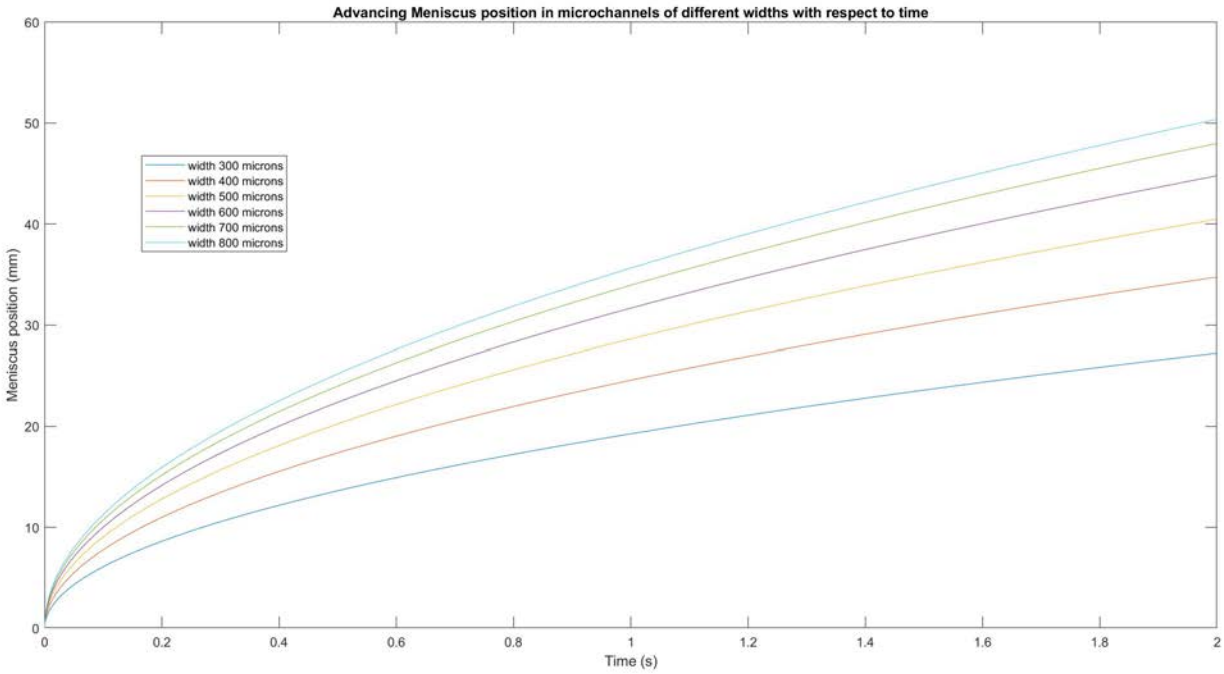

Figure 3.7: Meniscus position in Rectangular Microchannels with different widths

The theoretical estimation using equation 2.6 for the Capillary Pressure developed in the liquid-air interface in rectangular microfluidic channels with different widths is given as:

Capillary Pressure Developed	**Width of Microchannels**
$1432Pa$	$100\mu m$
$750Pa$	$200\mu m$
$523Pa$	$300\mu m$
$410Pa$	$400\mu m$
$342Pa$	$500\mu m$
$296Pa$	$600\mu m$
$264Pa$	$700\mu m$
$239Pa$	$800\mu m$

The layer thickness of Objet30 printer is $30\mu m$ and channels having width less than $200\mu m$ can be successfully printed but it requires complicated cleaning process. Removing trapped support material and uncured resin is quite hard for channels having width less than $300\mu m$. Hence, this $300\mu m$ is taken as the lower limit for microchannels. One of the design with width $300\mu m$ used for testing the flow of liquid in microchannels having rectangular cross-section with a constant depth of $500\mu m$ is shown in figure 3.8. The time taken for the liquid to cover the entire length of the microchannel (L=30mm) is measured in the experiments shown in section 4.2 . In the experiments

4 different widths of $300\mu m$, $500\mu m$, $600\mu m$ and $800\mu m$ are tested. The designs for other widths can be seen in appendix section C.2.

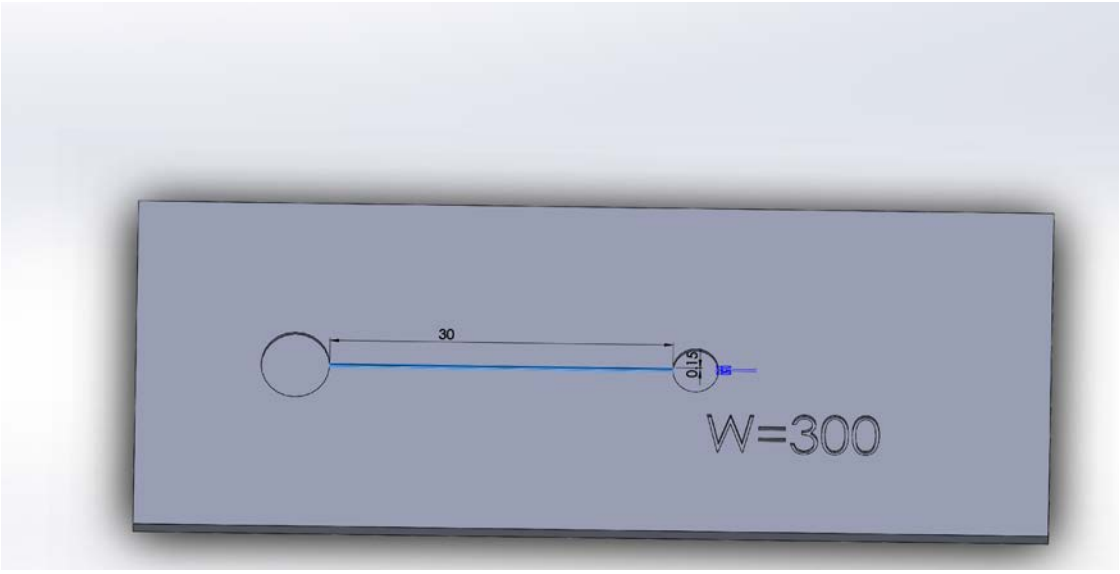

Figure 3.8: 30mm long microchannel with width=$300\mu m$ and depth $500\mu m$

A drop of $30\mu L$ is deposited in the inlet and then the liquid is wicked in and is driven by the capillary pressure developed in the liquid-air interface enhanced by the hydrophilic surface.
Another set of experiments was carried out with designs in which the width of the microchannel is kept constant at $600\mu m$ and the depth varied. The depths used for these experiments are $500\mu m$, $750\mu m$ and $1000\mu m$. The design used for the experiments with varying depths and constant width of $600\mu m$ is shown in figure C.8a. The liquid is timed till it covers the entire channel length of $20mm$ (refer section 4.2). The liquid pipetted into the reservoir is around $35\mu L$. It may be noted that with the addition of a reservoir and increasing the depth of the channels the total volume of the microfluidic system will increase. However, the total length of the channels is $20mm$ as compared to $30mm$ for devices having a constant depth and varying width as discussed before.

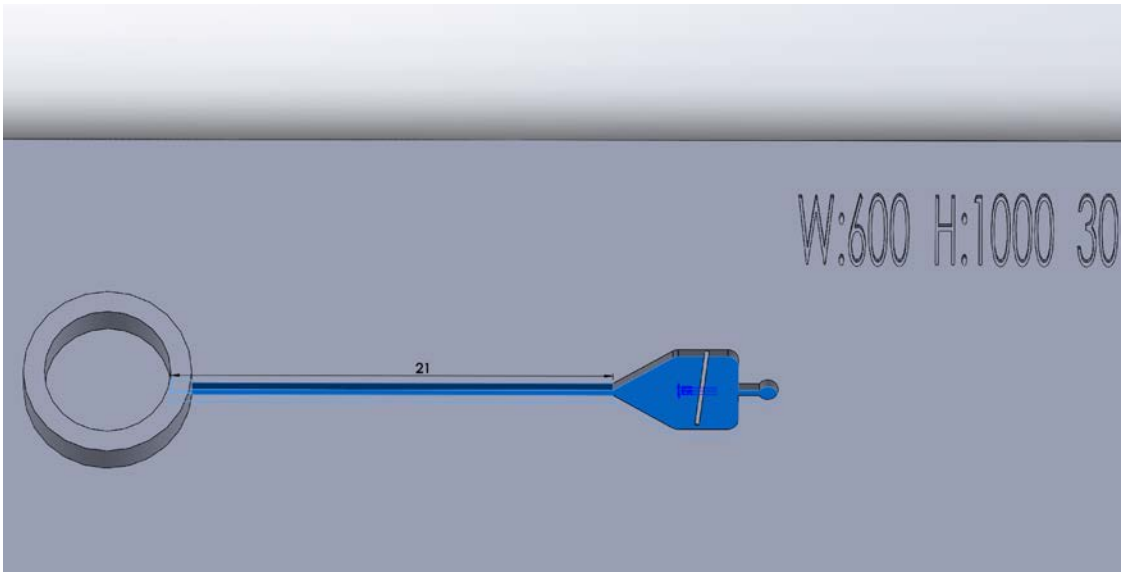

Figure 3.9: 20mm long microchannel (1mm inside reservoir) with width=600μm and depth 1000μm

3.4.2 Flow Resistors

The resistance or the friction inside the channel due to viscous forces can be increased by decreasing the width of the channels. As, discussed in section 2.1.5 and represented in equation 2.9 the flow rate depends on the driving pressure and the hydraulic resistance in the channels. The hydraulic resistance in rectangular microchannel depends on the width of the channels as shown in equation 2.10. With reference from the experiments done by B.Eker et al. [16] and Berthier et al [28], flow resistors are designed and later tested with experiments as shown in section 4.3. The progression of the liquid-air interface was timed as it travelled between the measurement points as shown in figure 3.10b. The length covered by the interface between these points is known and is compared with the theoretically calculated length in that time for a straight microchannel with the same width and depth.
The figures 3.10a and 3.10b show the design used for measuring the advancing meniscus positions with respect to time. The time measured from the experiment will be used to calculate the meniscus positions in a straight rectangular channel of the same path length and then a comparison will be drawn to validate the phenomena of decreasing the flow rate of the liquid in flow resistors.
Figure 3.10b also shows the path of the microchannel. The profile is a combination of straight and curved paths. There is more pressure loss in curved paths due to bend-losses as described by Akbari et al (2009) [42]. This decreases the flow speed and the liquid-air interface progresses slowly. The comparison is done with that of a straight channel where the length of the path is taken as:

$$L_{experimental} = 2 + 4 + \pi * 1 + 8 + \pi * 1 + 8 = 39.5mm \tag{3.1}$$

The length is the combination of the length of straight paths and the perimeter of the semi-circular arcs.
A droplet of 40μL volume of the water-dye solution (refer 3.2) is pipetted into the reservoir. The advancing meniscus position is timed when it progresses through the known lengths as given in

equation 3.1. This time is used to calculate the meniscus position of the liquid-air interface if the channel had a straight path. The plots are compared in the result and discussion chapter 4.3 4.

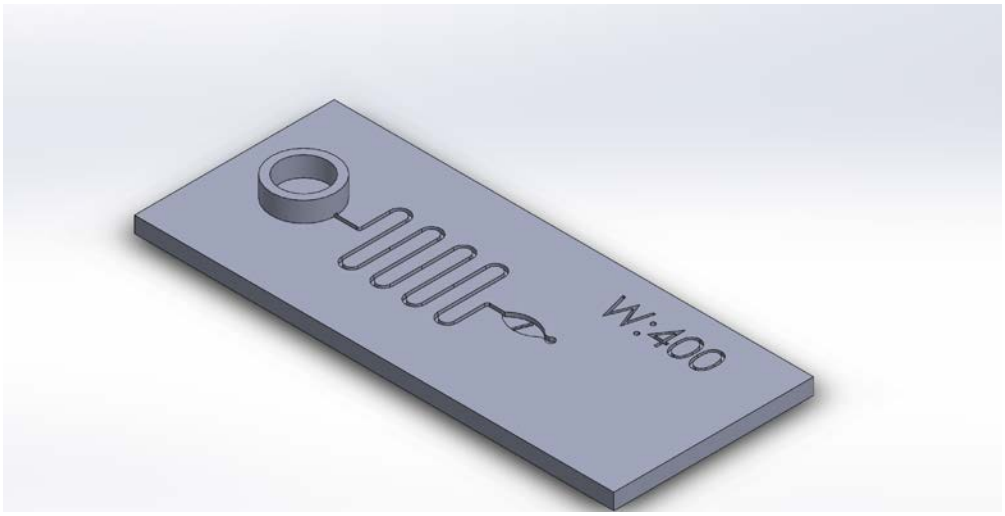

(a) Flow resistor device with $400\mu m$ width and $500\mu m$ depth of rectangular cross-section

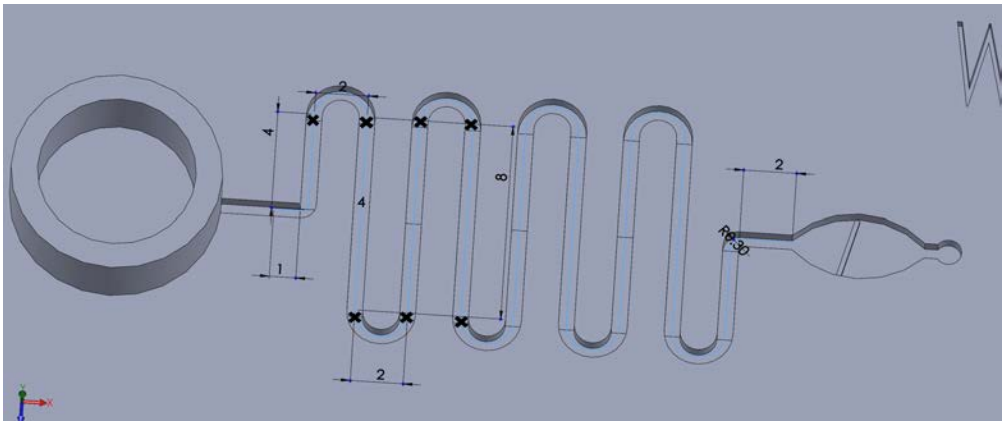

(b) The flow path for the liquid with the crosses representing the known points where the time measurements are taken

The time is measured for flow resistors with the design shown in figure 3.10a. Devices with this design and having different widths ($400\mu m$, $50mum$ and $600\mu m$) and constant depth of $500\mu m$ are tested (refer 2.1.6).

3.4.3 Valves

Passive Valves are used to give stops and delays to the flowing liquid. This is really useful in POCT applications as the model fluid can be pinned at specific locations where the reagents are present for chemical reactions to occur over time. The theory behind the functioning of the valves is explained before in section 2.2. Different actuation methods like soft-valves, meniscus trigger and

burst pressure application can be used to make the liquid flow further again. In this way valves can be used to time the progression of the flow as well. Incubation steps can be controlled with the use of these passive valves.
Certain geometrical expansions in the width or height changes the apparent contact angle (θ_c) of the liquid with the solid. The contact angle of the liquid with the solid material changes from θ_c to $\theta_c + \beta$ giving rise to a positive pinning pressure which opposes passive flow. Here θ_c is the contact angle with the solid and β is the expansion angle as explained in section 2.2. External pressure needs to be applied to overcome this pinning pressure. An approximate estimation of how the driving pressure varies with the channel length X for a microfluidic channel having width $800\mu m$ and depth $500\mu m$ as shown in figure 3.17 is plotted in MATLAB. This design was later also tested with experiments (refer section C.3). The length of the channel is 3mm and then it expands into a chamber of width $4mm$ with the expansion angle $\beta = 90°$. The maximum Pinning pressure when the liquid-air interface just reaches the expansion and the burst pressure when the interface enters the chamber has also been depicted in figure 3.12 using equation 2.12.

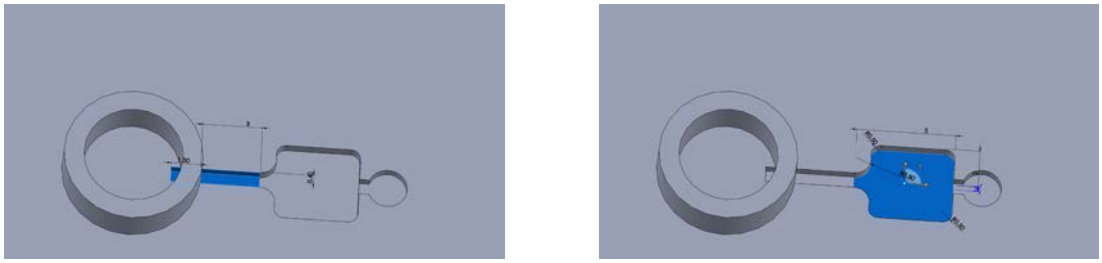

(a) highlighted channel of width $800\mu m$ (b) highlighted chamber with $\beta = 90°$

Figure 3.11: Valve design with expansion at X=3mm

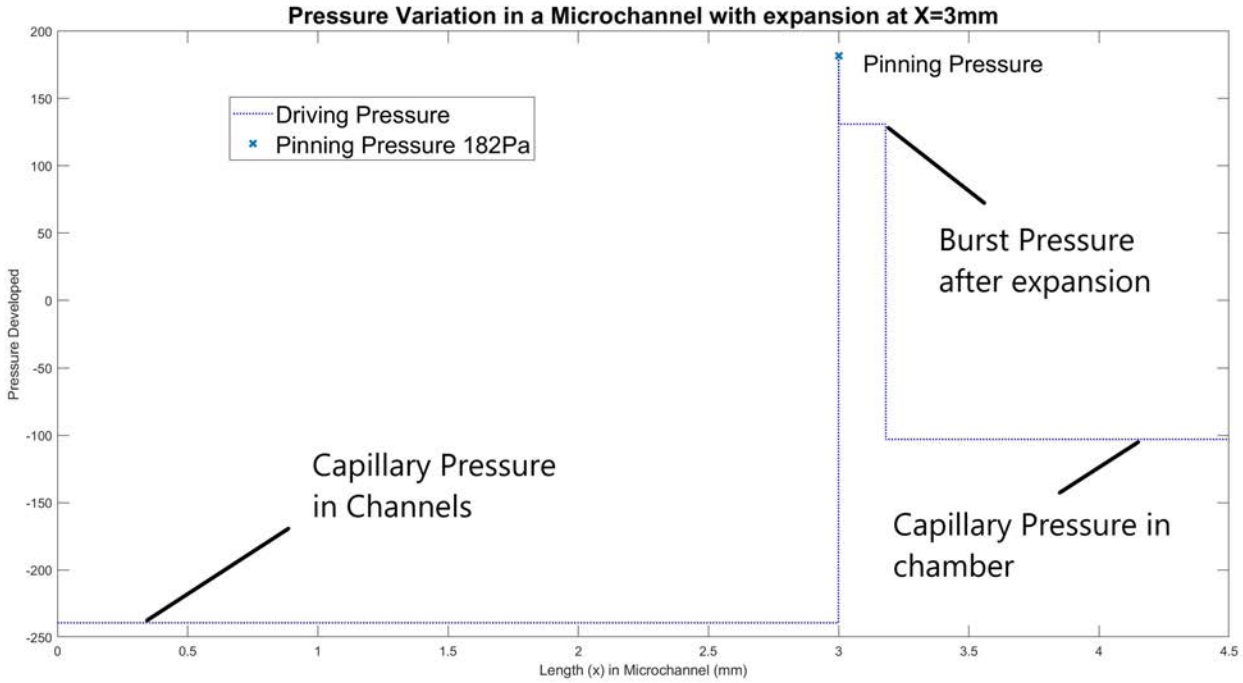

Figure 3.12: Different phenomenons observed in passive valve with pressure variations(geometrical expansion at X=3mm)

Valve designs with reservoir The designs for the valves have been split into ones where the liquid is pipetted into a reservoir and one where the liquid is pipetted into an inlet/loading-pad. The design used with reservoir is depicted in figure 3.13. The reservoir is a feature that makes sure enough liquid is present in the system. The liquid in the reservoir also adds to the hydro-static pressure with the developed capillary pressure that drives the liquid-air interface forward. Though this pressure is really minute at micro-scale but still the impact of the reservoir would be interesting to observe. The design features a rectangular microchannel of fixed width $600\mu m$ and depth $500\mu m$ with different expansion angles β for the valve. For these experiments, β=30°, 60°, 90° and 120° are tested. The geometrical expansion occurs at X=20mm.

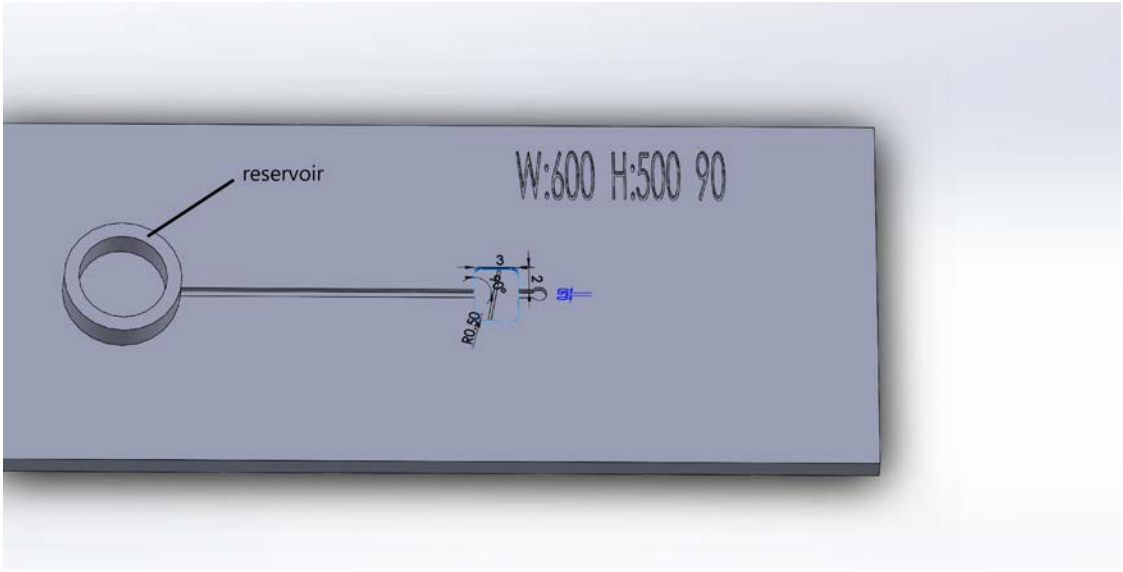

Figure 3.13

Valve designs without reservoir The next set of experiments require a design without the reservoir feature. The inlet is a $500\mu m$ deep circular well. This does not add up to any hydrostatic pressure and the liquid wicks in with only the Capillary pressure developed in the liquid-air interface. The designs used for the experiments with varying channel widths of $300\mu m$, $500\mu m$ and $800\mu m$ wit constant depth of $500\mu m$ are tested with different expansion angle β (30°, 60°, 90° and 120°. The designs used for these experiments have a geometrical expansion at X=30mm, where the channel expands into a chamber acting as valve as can be seen in figure 3.14.

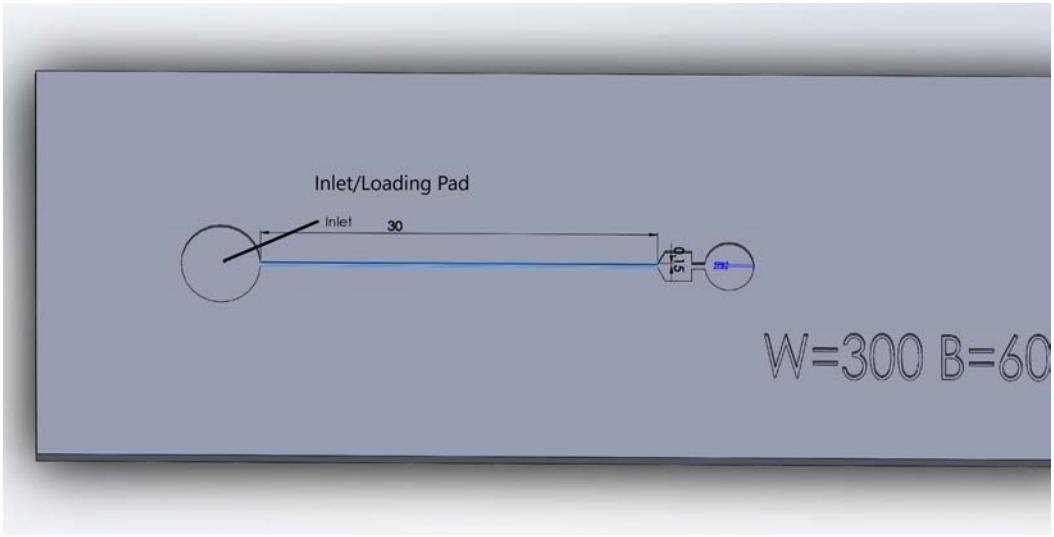

Figure 3.14: one of the design used for testing valve feature without the reservoir

3.4.4 Parallel flow paths with time delay channels for Meniscus trigger microvalves

Delay Channels are significant in POCT devices where some time delay is required for proper mixing of the reagents with the model fluid via diffusion in the microchannels similar to the application of flow resistors as explained above in section 2.1.6. The property of friction factor or hydraulic resistance in the microchannels is used for designing these delay structures. The theory behind this can be found in section 2.1.6.
The liquid travels faster in channels which has higher flow rate Q as explained in theory 2.1.6. The use of delay channels can be used for actuating microvalves. In this way pinned liquid-air interface can progress further without any external actuation method.
For testing this delay structure, the flow is split into two channels. Initially the fluid will flow faster in the wider channels having less hydraulic resistance (refer section 2.2.3). Once, the liquid reaches the delay structure then the fluid will progress in the channel with more magnitude of flow rate $Q \propto \frac{\Delta P}{R}$. After covering the full length of the fast channel, the liquid is pinned at the expansion acting as a valve. The valve expands more from fast channels as compared to slow channels as seen in figure 3.17a and 3.17b.After that the liquid propagates through the delay channel as the driving pressure is more in channels as compared to positive pressure built in at the expansion. The liquid arriving later then triggers the pinned liquid with the meniscus. This acts as a meniscus trigger valve and does not require any actuation. The results for these experiments are given in section 4.5.
The designs used for carrying these experiments are shown in figure 3.15 and 3.16.In figure 3.15, the delay structures have a width of $300\mu m$ and that of straight channel which carries the fluid fast is $500\mu m$. In figure 3.16, the upper channel has delay structures of $300\mu m$ width and the lower fast channel is $600\mu m$ wide.

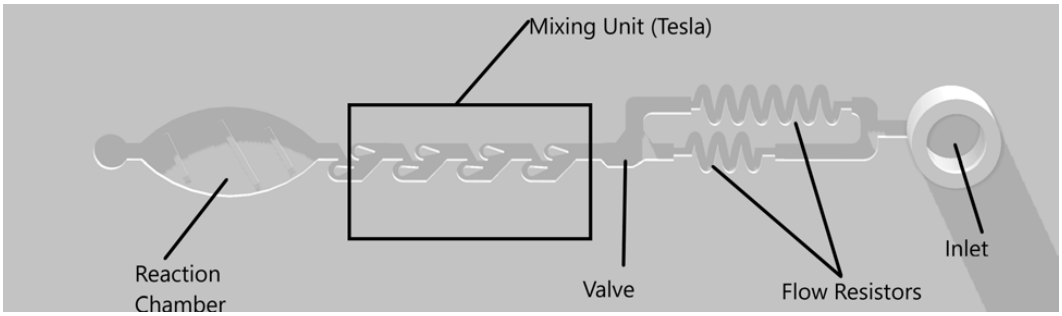

Figure 3.15: Time delay structure with mixing unit

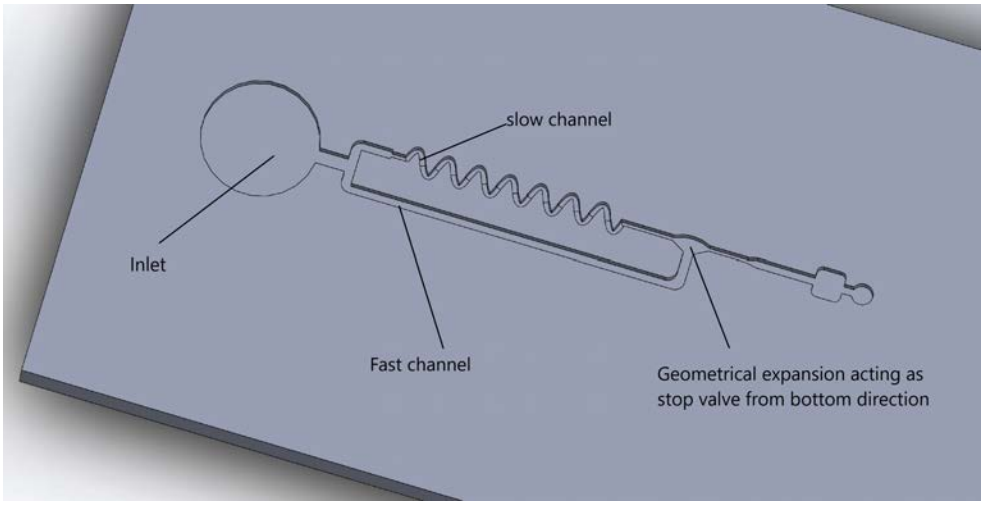

Figure 3.16: Time delay structure with fast and slow channel

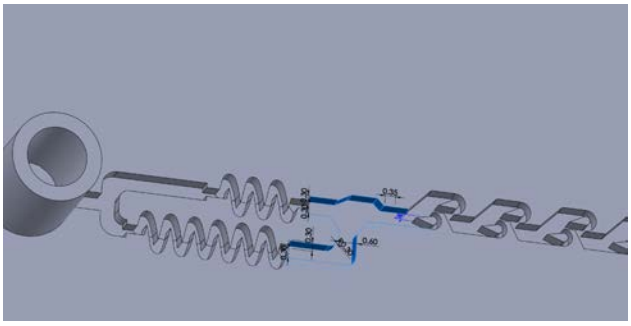

(a) Micro-valve for design 1

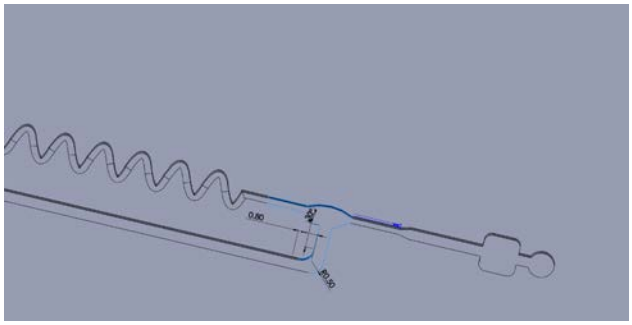

(b) microvalve for design 2

Figure 3.17

3.4.5 Phaseguides

Phaseguides are ridges on the bottom surface of the chamber or channel as explained in section 2.3. These patterned stripes act as capillary pressure barrier almost perpendicular to the direction of the advancing liquid-air meniscus. These stripes or ridges force the liquid to align itself against the length of the stripes and the liquid-air interface advances forward once the pinning pressure developed due to these phaseguides is build up. These structures are helpful for complete filling of the chambers and also to avoid air bubble inclusions. These are helpful in reaction or detection chambers in POCT devices where complete chamber filling is essential and any sort voids or gaps due are undesired. In a lot of POCT devices the detection is done optically so a uniform volume of the fluid is desired in the detection chamber so phaseguides can be useful in that application. The pinning pressure and the factors effecting it have been explained in the theory section 2.3.
Some of the designs used for testing this phenomena are shown in figures 3.18 and 3.19. The proper theory behind the functioning of these phaseguides is explained in section 2.3.

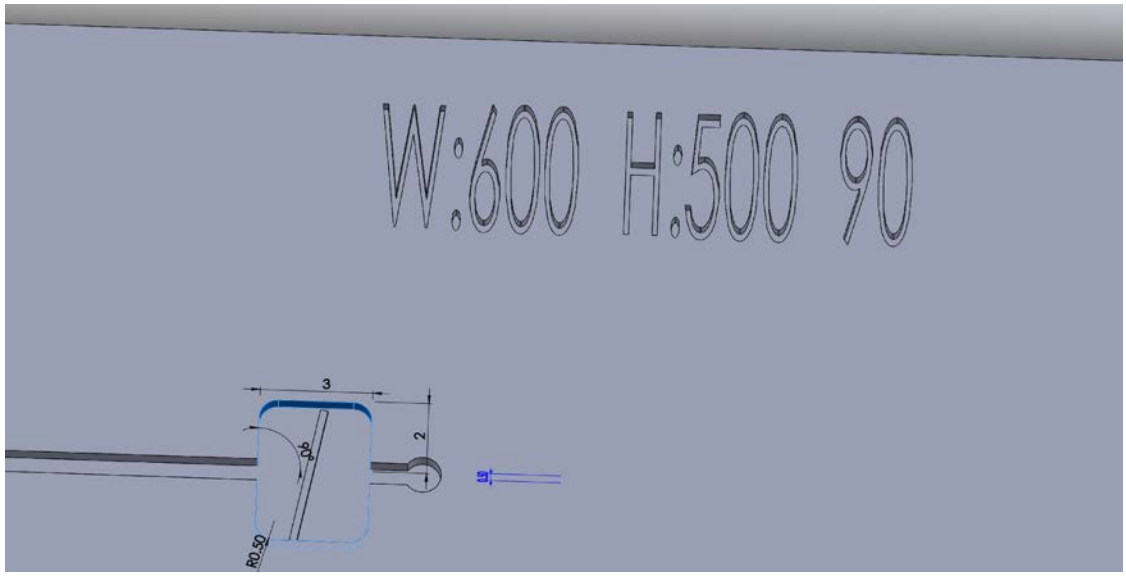

Figure 3.18: Phaseguide in the chamber

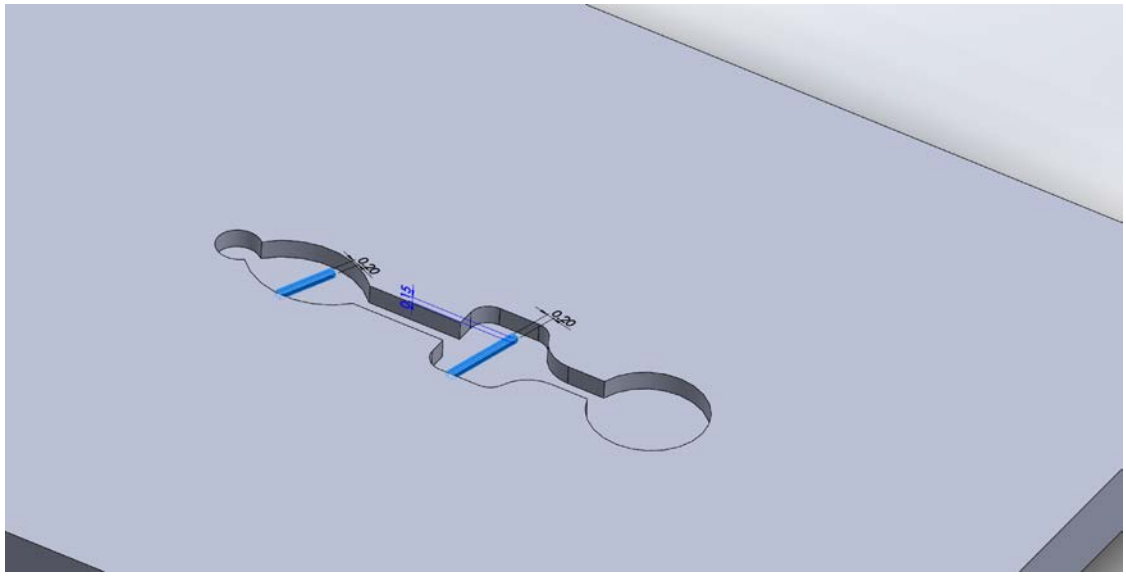

Figure 3.19: Phaseguide structures on the surface of the chambers

Chapter 4

Results and discussion

4.1 Parts printed with Objet30 Printer

Devices fabricated with Objet30 printer were observed and analysed for mismatch in dimensions and variations in the characteristics compared to the CAD designs (refer B). Transparent and rigid microfluidic devices which can be sealed with a well plate cover as explained in section 3.3 are used for doing experiments. One key observation with printing is that the corners of the top edge of the microfluidic devices become round due to the stray light effect of the 3D printer which causes uncontrolled polymeirzation of the resin resulting in over-curing. This is also documented by Samper et al [27]. Figure 4.1a shows the designed CAD model with straight rectangular edge viewed from the front and 4.1b shows the front view of how the printed part would look like due to this effect.

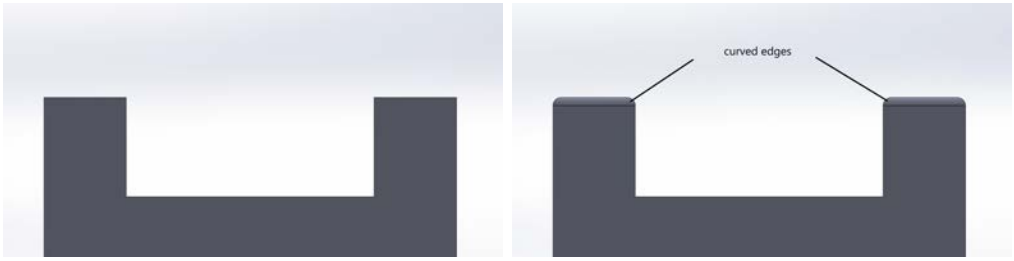

(a) How the edges should look like (b) How the edges appear when printed

Figure 4.1: Design variations

This effect results in some voids being developed when the hydrophobic tape is used to seal the devices. The tape does not adhere well on the curved corners leaving some voids. The liquid enters these voids as they act as small capillaries and this phenomena also leads to mismatch in the flow time from theoretical predictions in microchannels as will be discussed next in section 4.2. The voids also lead to air-inclusions which is not a desired characteristic for POCT microfluidic devices. Figure 4.2 shows the liquid escaping in voids along with the bubble entrapped in the microchannel of 600μm width (error 2% from the designed dimension) and 500μm depth.

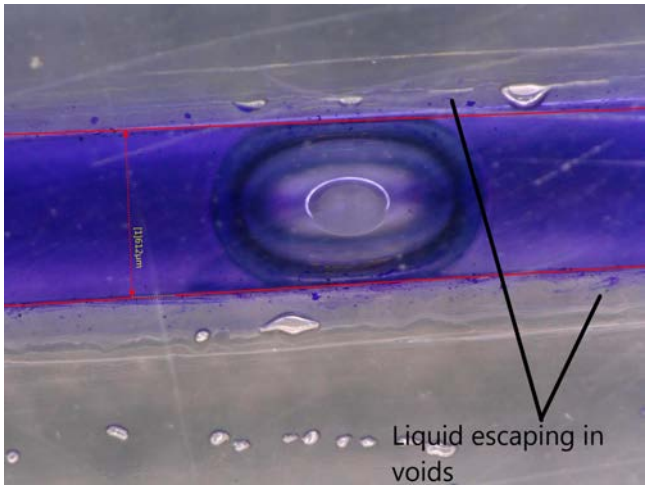

Figure 4.2: Liquid in the voids along with the bubble being trapped in the channels of width $600\mu m$

4.2 Passive Flow in rectangular microchannels

For studying the flow in rectangular channels the design shown in section 3.4 is used for the experiments. The time required to cover the entire length of the microchannel is measured and then compared with the theoretically calculated distance covered by the liquid filling front in that time period using equation 2.11. Error bar graphs are plotted indicating the variation from the theoretical prediction (refer section 2.1.5) in microchannels with the same dimensions as the devices used for experiments. These microchannels are used for transporting the model fluid and reagents to different locations in the microfluidic device. So, a rough estimation of the flow time and fluid behavior would be important in these microchannels when designing for POCT microfluidic devices.

4.2.1 Depth=$500\mu m$ and different widths

Widths of $300\mu m$, $500\mu m$, $600\mu m$ and $800\mu m$ have been tested in experiments and the time taken to cover the length of the entire microchannel is noted. The plot shown in figure 4.3 depicts the theoretical model for the length covered with respect to time using equation 2.11. It shows that the liquid-air interface should progress the fastest in $800\mu m$ wide channel and the slowest in $300\mu m$ wide channels. From the figure 4.3, in table 4.1 shown below the theoretically calculated time required to cover $30mm$ length of microchannel for different widths is given. This time is also indicated in the plot shown in figure 4.3 with a '*' marker.

Table 4.1: table indicating predicted time to cover 30mm length

Width	**Calculated time**
$300\mu m$	$2.4s$
$500\mu m$	$1.1s$
$600\mu m$	$0.9s$
$80\mu m$	$0.7s$

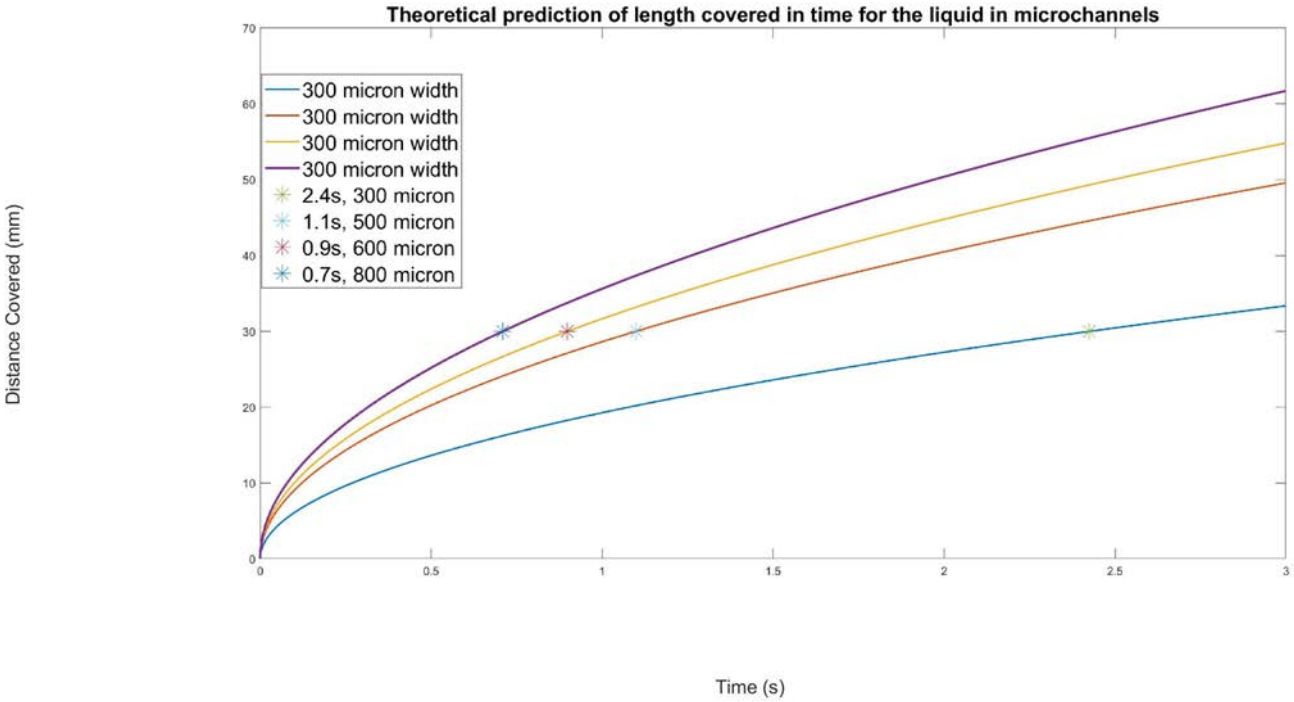

Figure 4.3: In the plot the solid lines represent the distance covered by the liquid with passive flow in microchannels of different width and the asterisk sign '*' represents the time taken to cover 30mm of length in microchannels for these channels

The results for the average time, average error percentage which is calculated by taking the difference between the theoretically calculated distance(using equation 2.11) covered by the liquid with the experimentally observed distance and the experimental distance itself for microchannels of different widths and same depth of $500\mu m$ is shown in table 4.2 below.

Table 4.2

Width	**Experimental Length**	**Average Time**	**Average Error percentage**
$300\mu m$	$30mm$	$2.6s$	6.3%
$500\mu m$	$30mm$	$2.9s$	38.4%
$600\mu m$	$20mm$	$1.2s$	42.3%
$800\mu m$	$30mm$	$2.8s$	46.5%

The errorbar graphs depicting the standard deviation from the theoretical prediction for different widths of microchannels tested by carrying 4 experiments per device are shown in figure 4.4. It can be seen that the error increases with increase in the width of the channels. The average error percentage for $300\mu m$ wide channels is the minimum at 6.3% and that for $800\mu m$ wide channels is the maximum at 46.5%. This trend can also be observed with the errorbar graphs shown in figure 4.4.

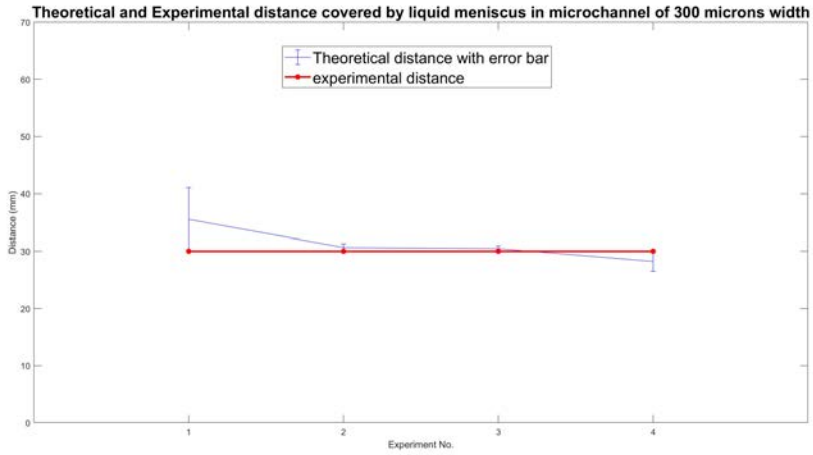

(a) Errorbar graph for channels with width $300\mu m$

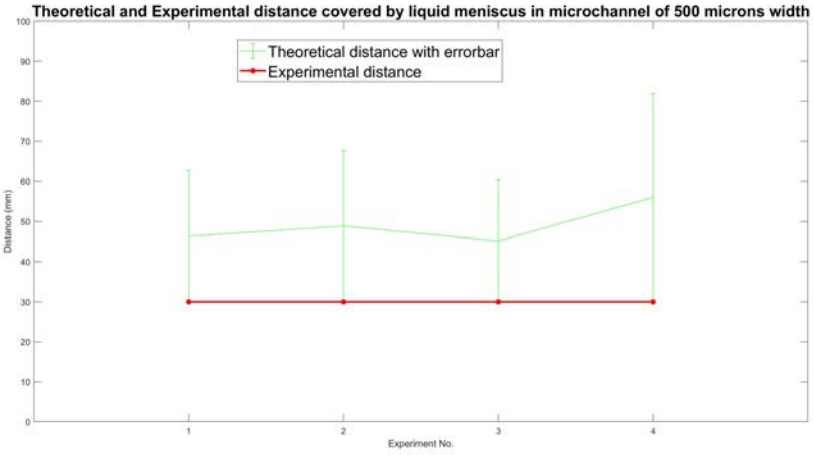

(b) Errorbar graph for channels with width $500\mu m$

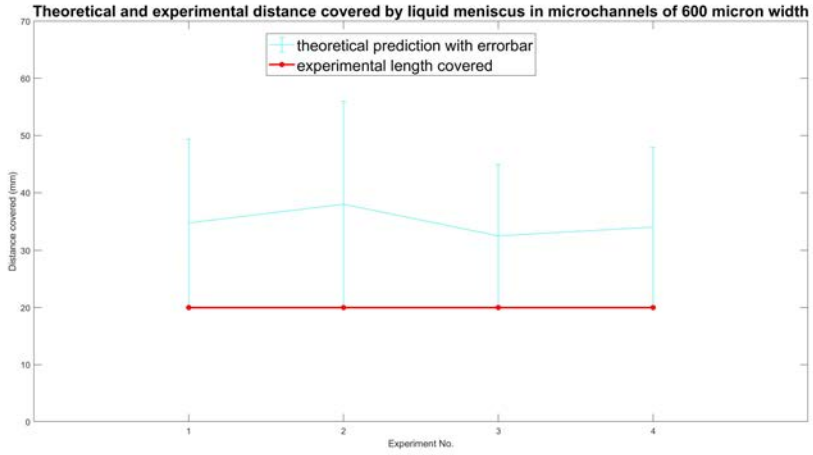

(c) Errorbar graph for channels with width $600\mu m$

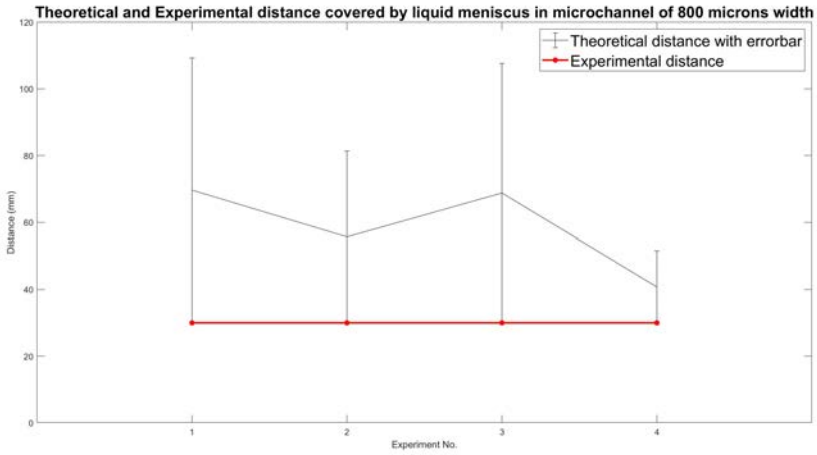

(d) Errorbar graph for channels with width $800\mu m$

Figure 4.4

The error percentage increases with the width of the channels. Theoretically the fluid travels faster in wide microchannels since the hydraulic resistance is much less as compared to narrow channels despite more driving capillary pressure developed in the latter case (refer section 2.1. The wider channels have more surface area that the liquid wets and the mismatch can be possible because of the following reasons:

- Variation in Contact angles with the solid surface is high when the surface area is increased leading to driving pressure variations as well
- The area of the liquid-air interface with the hydrophobic top sealant also increases which would result in pressure that opposes passive flow. Viscous forces will oppose the liquid progression
- The liquid also fills the voids developed due to curved corners of the rectangular microchannels due to limitation of the 3D printer

4.2.2 Width=$600\mu m$ and different depths

The results obtained by keeping the width of the channels constant at $600\mu m$ and varying the depths are discussed in this subsection. The depths used for these experiments are $500\mu m$, $750\mu m$ and $1000\mu m$. The design for the devices used for these experiments have been shown in section 3.4. Theoretical prediction for the devices show that the liquid-air interface will progress the slowest in the channel with the maximum depth and faster in shallow channels.

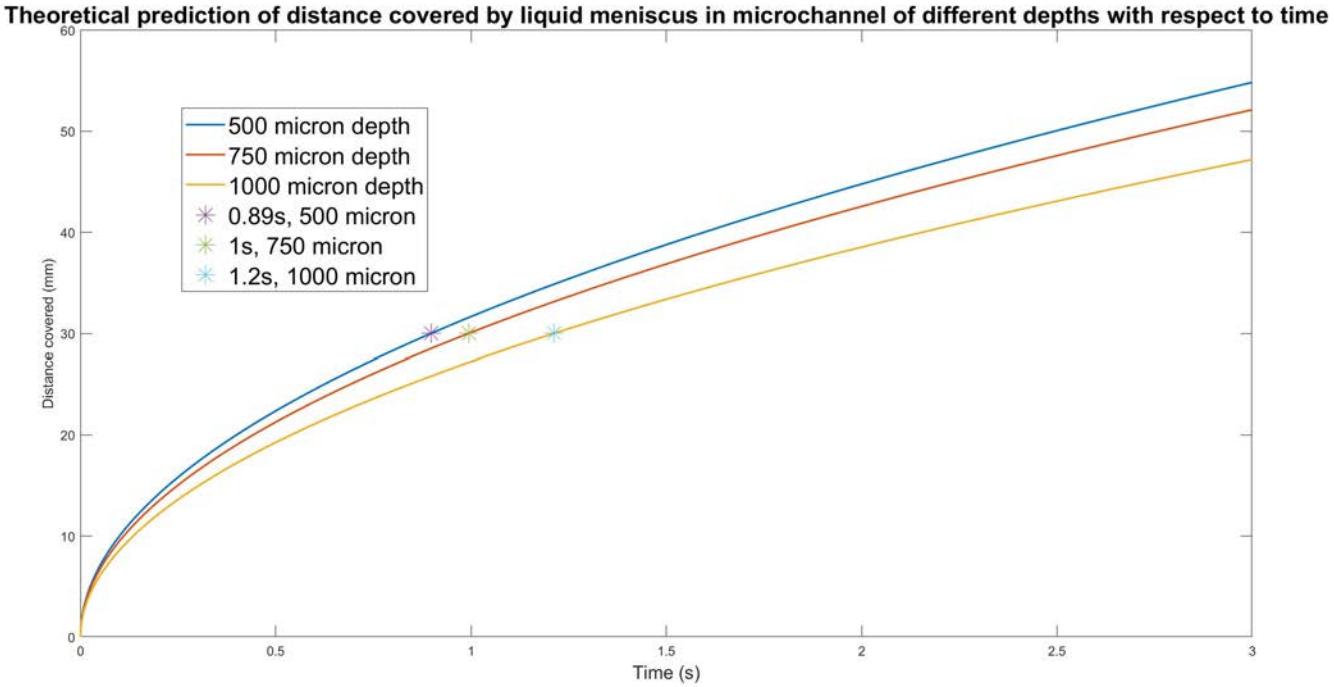

Figure 4.5: Distance covered by liquid filling front with respect to time in microchannels with $600\mu m$ width and different depths

The figure 4.5 shows that thoeretically the time taken to cover the length of $20mm$ is least with $500\mu m$ deep channels and most with $1000\mu m$ deep channels. The prediction is done using the value of the distance covered by the liquid filling front with respect to time as given in equation 2.11. The calculated time required to cover the length of $20mm$ for a constant width of $600\mu m$ can be shown below in table 4.3:

Table 4.3: theoretically calculated time to cover 20mm distance in $600\mu m$ wide channels

Depth	**Calculated time**
$500\mu m$	$0.89s$
$750\mu m$	$1s$
$1000\mu m$	$1.2s$

The designs were tested experimentally and the measurements were compared with the theoretical predictions calculated using equation 2.11. Per design three independent measurements were done and an errorbar plot is generated indicating the difference in the theoretical calculations and experimental results as shown in figure 4.6.

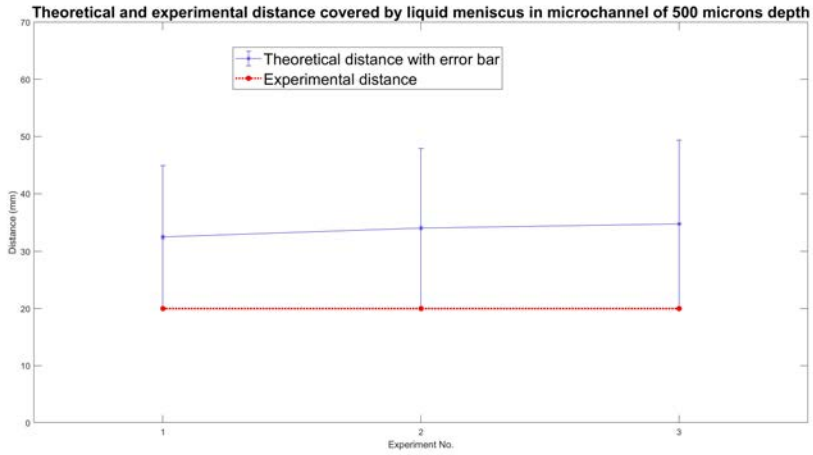

(a) errorbar graph for channel depth $500\mu m$

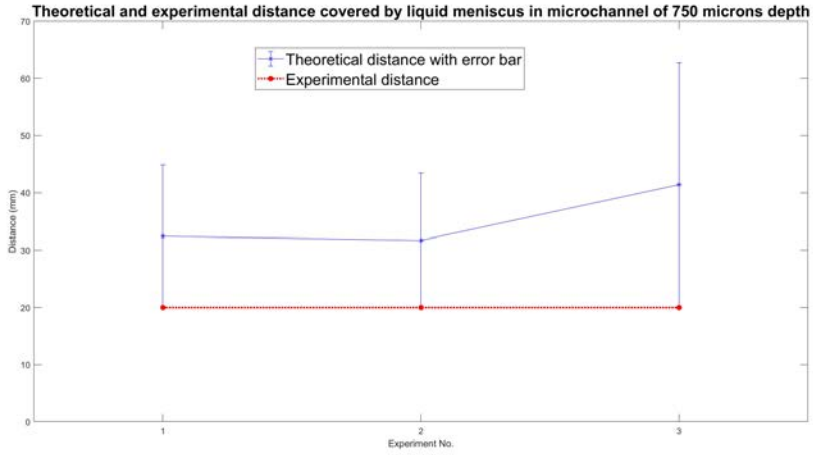

(b) errorbar graph for channel depth $750\mu m$

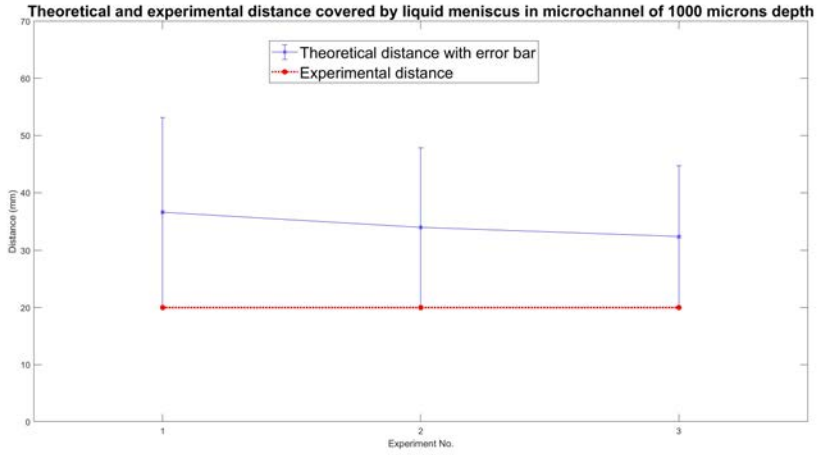

(c) errorbar graph for channel depth $1000\mu m$

Figure 4.6

Table 4.4

Depth	Experimental Length	Average Time	Average Error percentage
$500\mu m$	$20mm$	$1.13s$	52.2%
$750\mu m$	$20mm$	$1.38s$	43.3%
$1000\mu m$	$20mm$	$1.59s$	35.3%

The error decreases with increase in depth of the channels as seen in table 4.4. This is predictable as with increase in depth, the width will become the determining factor for calculating the driving capillary pressure and the hydraulic resistance as described by David Juncker and colleagues,2009 [7]. Thus, the error between the theoretical prediction and the experimental result will be less as the approximation taken for calculating the progression distance of the liquid-air interface will be more accurate. The liquid filling front progresses the slowest in the channel with maximum depth which is also the case with the experimentally determined values.

4.3 Flow Resistors

As discussed in section 3.4, flow resistors are a combination of straight and curved paths that are used to decrease the flow rate of the liquid in the channels. The flow rate as depicted in equation 2.9 depends on the hydraulic resistance and the driving pressure. The hydraulic resistance can be increased by decreasing the width of the channels, in meandering channels with combination of straight and curved paths the driving pressure is decreased because of bend pressure losses. This is because the liquid is continuously being bent and dragged along the curves resulting in loss of driving pressure. This can also be attributed to the increased friction factor in curved paths but is not a concrete argument as in numerous studies different results for friction factor in microchannels of arbitrary profile are documented. The flow resistor microfluidic feature is experimentally tested and the advancing meniscus position is timed after covering known lengths and perimeters. The lengths measured between the marked points as shown in figure 4.7 are described in section 3.4.2. The experimentally obtained time values are used to theoretically calculate the length covered in case the channel profile or path would have been fully straight instead of having a Flow resistor feature using equation 2.11. Then the two lengths (experimental length in meandering channels and theoretical length in straight channels) are plotted with respect to time to compare the difference and to indicate whether these flow resistors are useful in decreasing the flow rate of the liquid to make the flow slower in the channels.
Three different widths of the channels used for the experiments are $400\mu m$, $500\mu m$ and $600\mu m$ respectively. The design used for the devices with different widths is shown in the section 3.4. Figure 4.7 shows the points where the liquid position was timed. The points are marked by a 'cross' and then the time-elapsed while covering the length between two points is used to calculate the theoretically predicted distance the liquid will cover. Equation 2.11 is used for calculating this distance.

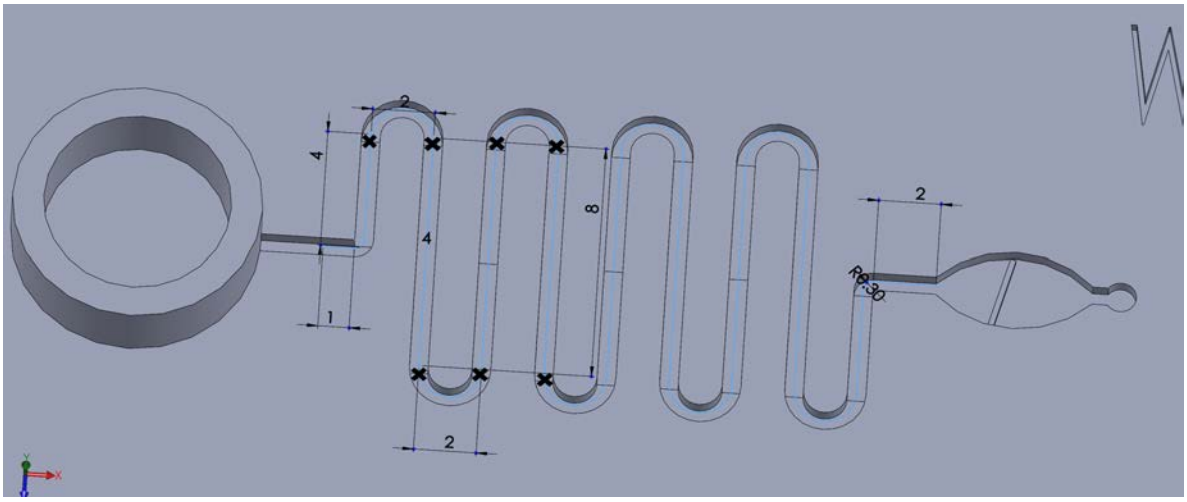

Figure 4.7: The flow path the liquid will advance travel through. The cross indicates the reference points where the time measurements are taken

Figures 4.8a to 4.8h shows the advancing liquid meniscus over time in flow resistors with rectangular cross-section having width $400\mu m$ and depth $500\mu m$. It was observed that the liquid travels much slower in the curved paths as compared to the straight paths.

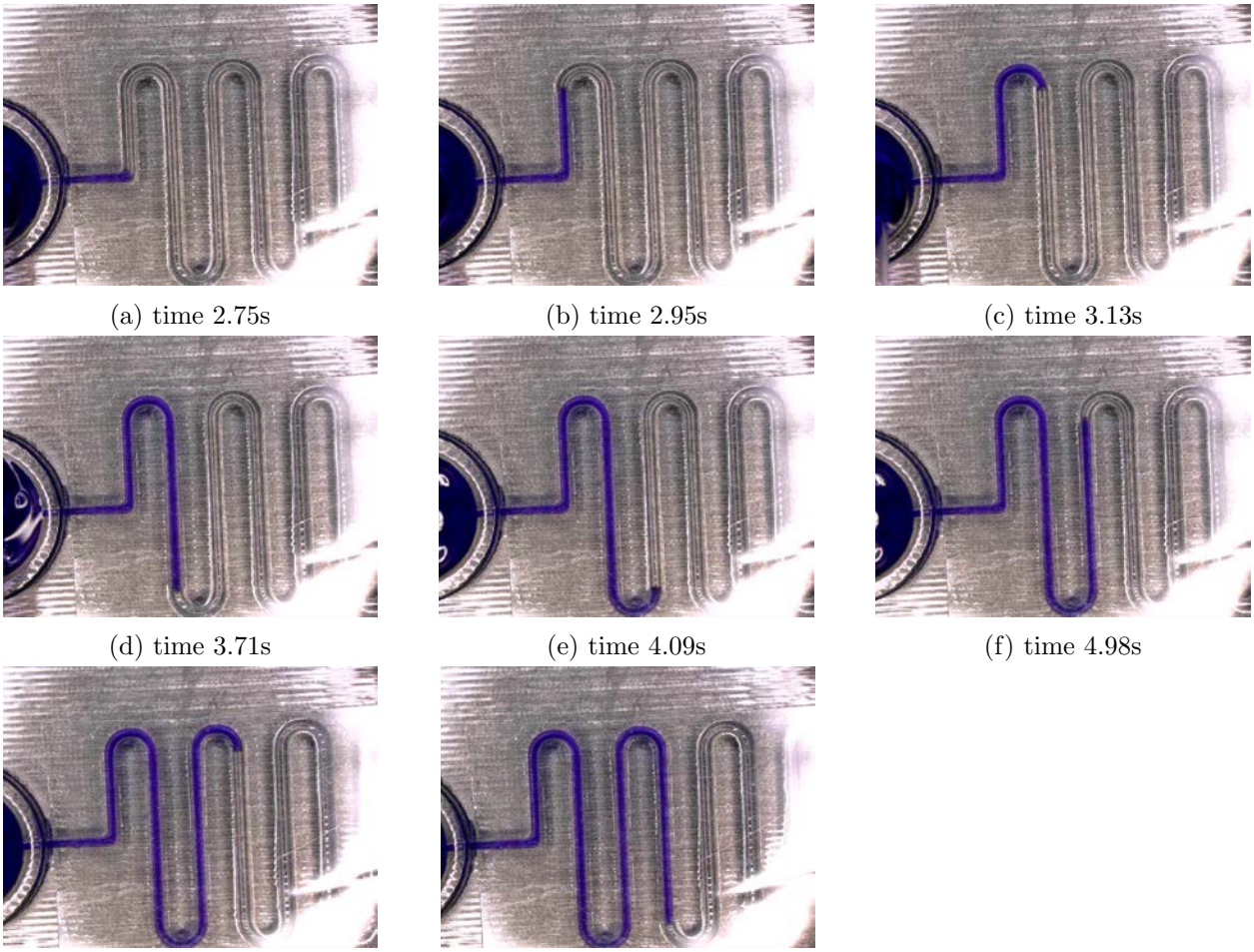

(a) time 2.75s (b) time 2.95s (c) time 3.13s

(d) time 3.71s (e) time 4.09s (f) time 4.98s

(g) time 5.78s (h) time 6.76s

Figure 4.8: Liquid inside the flow resistor of 400μm wide channel progressing at different times. The time measurements are taken at specific points also indicated earlier

The time elapsed as measured from the experiments is used to calculate the theoretical distance covered by the liquid filling front in straight rectangular channels of the same width and depth as that of the flow resistors and these theoretical lengths are compared with the experimentally observed results with respect to time. In section C.1 in appendix, the images showing the advancement of liquid filling front for 500μm and 600μm width of the flow resistors are shown. The plots in figure 4.9 show the comparison between the two path lengths (theoretical and experimental) travelled by the liquid filling front over time. As observed from figure 4.9, the time taken for the liquid to progress in flow resistor structures of having 400μm is the fastest whereas that of 600μm wide channels is slowest. 4 Experiments per device were carried out, the time taken for the liquid to cover this length as shown in section 3.4.4 is not consistent. The time taken in other experiments to cover this known length is quite high, indicating that flow resistor structures are functional in reducing the flow time of travelling liquid in the micro-system despite inconsistency in the time values.

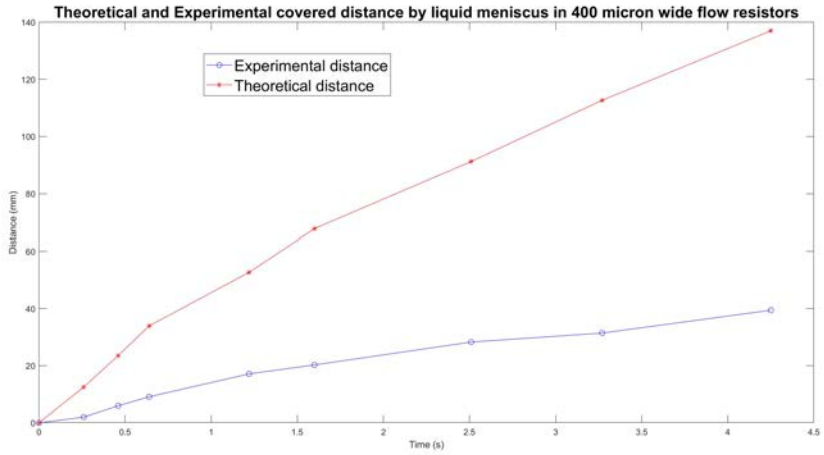

(a) Flow resistor microfluidic channel with width=400μm

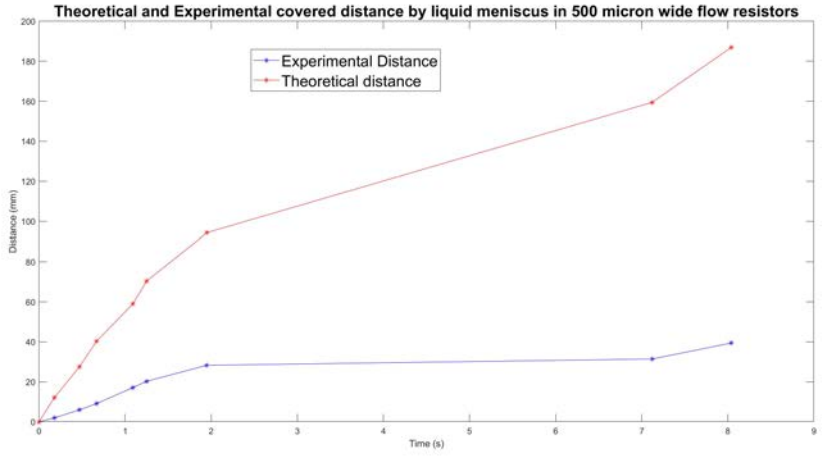

(b) Flow resistor microfluidic channel with width=500μm

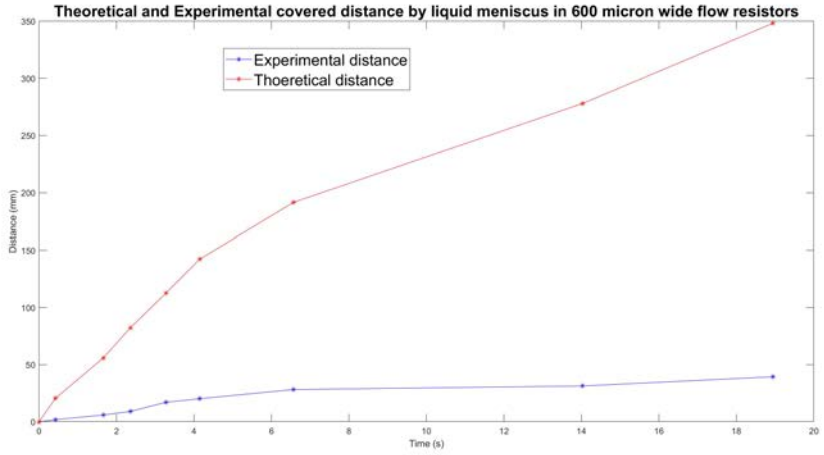

(c) Flow resistor microfluidic channel with width=600μm

Figure 4.9

4.4 Valves

The function of passive valves as explained in the theory section 2.2 has been studied with the designs as shown in section 3.4.The behaviour of the fluid when it meets a certain geometrical expansion is studied in the experiments using valve design as shown in section 3.4 and the different phases of the liquid-gas interface are recorded. These results are then compared with the ones already obtained by previous researchers, as explained in theory 2.2. Actuation methods to trigger the pinned liquid to make it progress further into the geometrical expansion acting as the passive valves have also been discussed. The 3 phenomenons observed in these experiments when the liquid meniscus reaches the valve are:

- wicking
- pivoting
- expansion

4.4.1 Valves with reservoir

Valves with reservoir add up a ρgh hydrostatic pressure term to the driving capillary pressure. The volume pipetted into the reservoir is approximately $35\mu L$. Since, the fluid used is dye mixed in water so the density of the liquid is bit more than de-mineralised water. However, the differences are small so an approximation with $\rho = 997kg/m^3$ is taken. The hydrostatic pressure build up in this case with h=2.5mm is $24.5Pa$ (compared to capillary pressure of $\approx 600Pa$ in $300\mu m$ wide and $500\mu m$ deep channels).The designs used for the experiments conducted have channels with rectangular cross-section. The width and the depth of the channels being $600\mu m$ and $500\mu m$ respectively. The results from the experiments are as follows:

$\beta = 30°$

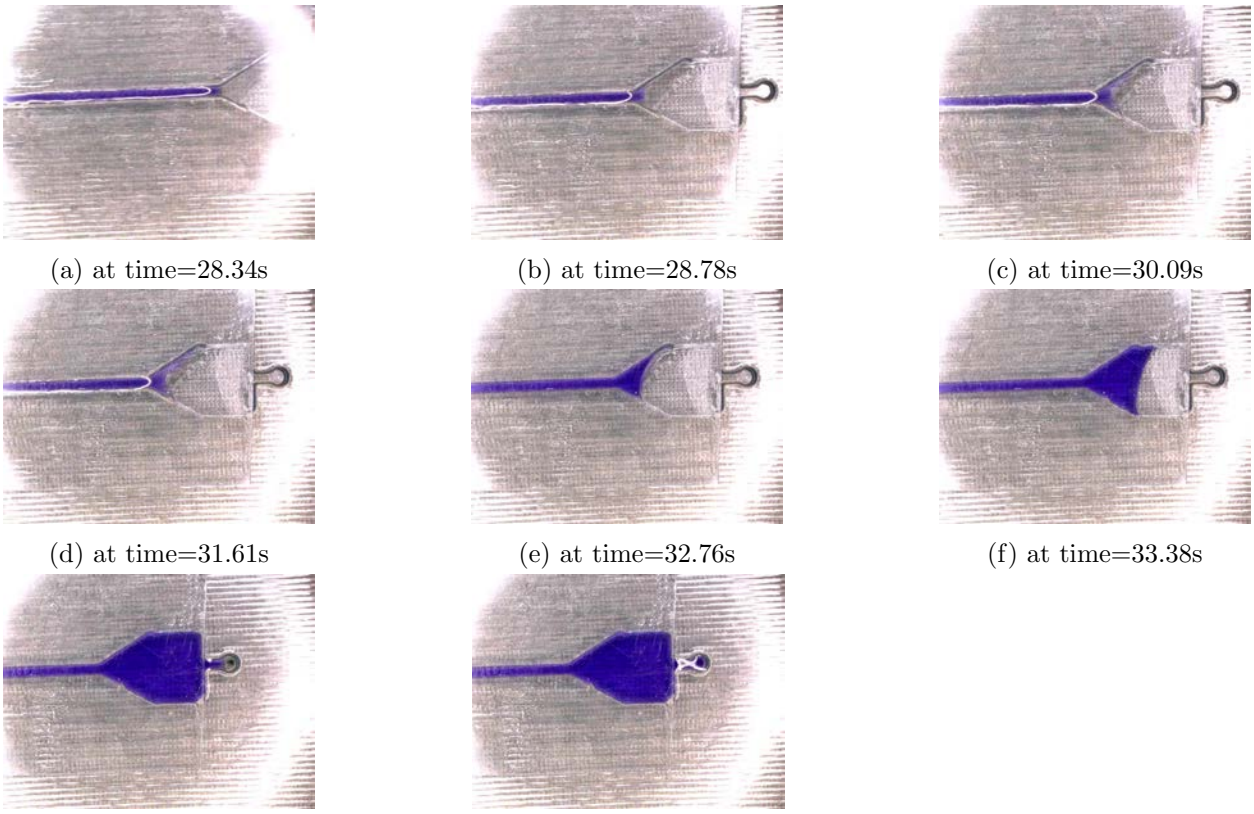

(a) at time=28.34s (b) at time=28.78s (c) at time=30.09s

(d) at time=31.61s (e) at time=32.76s (f) at time=33.38s

(g) at time=34.75s (h) at time=35.28s

Figure 4.10: different phases of the liquid-air interface when it reaches a geometrical expansion with expansion angle $\beta = 30°$

As observed in figures 4.10a to 4.10h, the liquid-air interface pins at the expansion for 2-3 seconds only, thus behaving as a delay valve instead of a stop valve. The factors or observations which might play a role are discussed later in this section. In total 7-8 experiments with the same width and expansion angles were carried out at different times. The variations were in the length of the microchannel which varied from 3mm to 30mm and the volume deposited in the reservoir. For channels with microchannel length between 3mm to 8mm the volume deposited in the reservoir was around $30\mu L$ instead of $35\mu L$. The results from all 7-8 experiments are aligned, with the delay varying from 0.5-3 seconds for expansion angle of $\beta = 30°$.

$\beta = 60°$

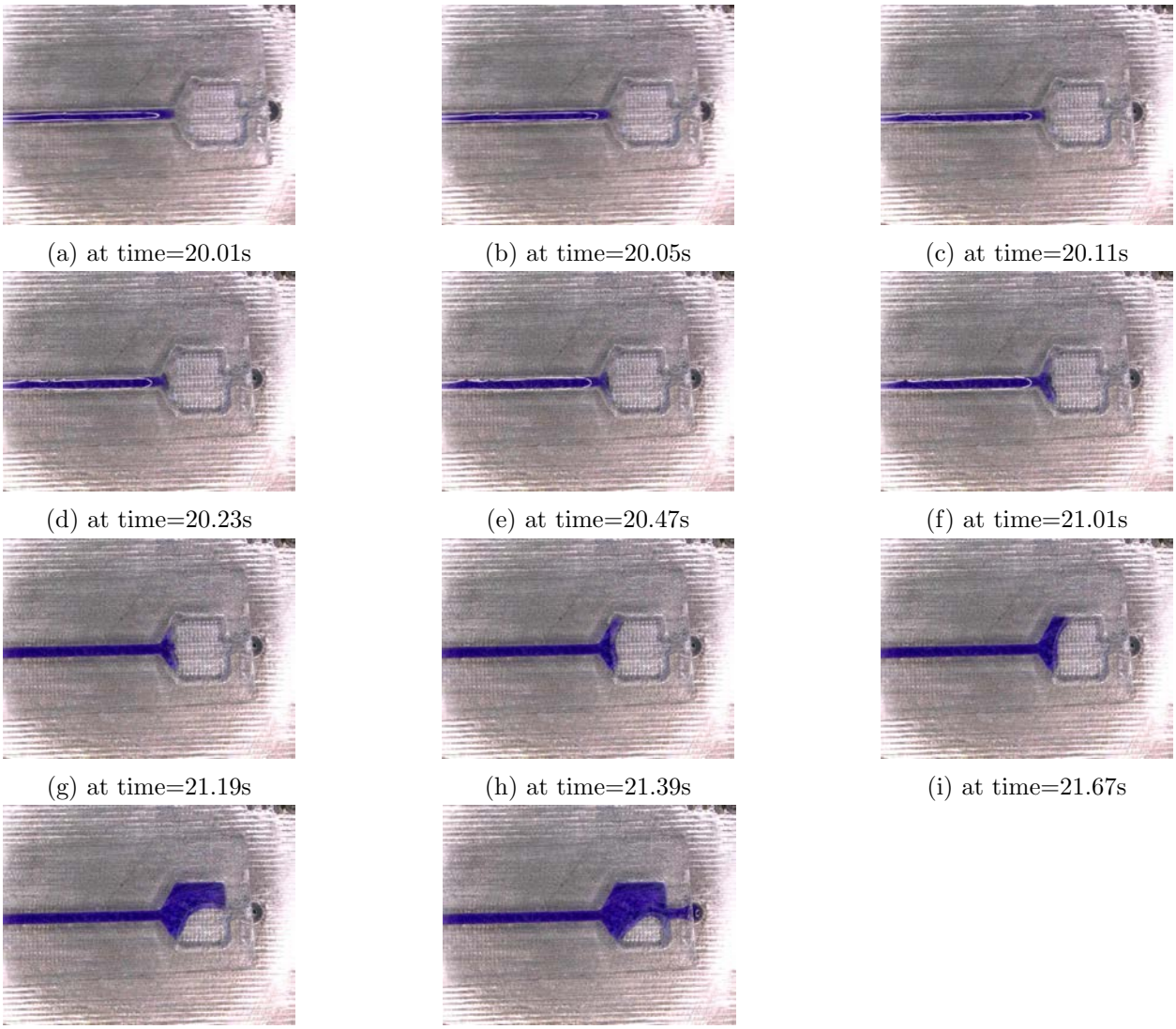

(a) at time=20.01s (b) at time=20.05s (c) at time=20.11s

(d) at time=20.23s (e) at time=20.47s (f) at time=21.01s

(g) at time=21.19s (h) at time=21.39s (i) at time=21.67s

(j) at time=23.67s (k) at time=24.26s

Figure 4.11: different phases of the liquid-air interface when it reaches a geometrical expansion with expansion angle $\beta = 60°$

From figures 4.11a to 4.11k it can be seen that the liquid pins at the expansion for less than 2 seconds. The valve thus behaves as a delay valve. The results for this case with valve expansion angle $\beta = 60°$ and channel width $600\mu m$ are reproducible as more than 7-8 experiments done with same designs with only the channel length varying (as discussed previously for $\beta = 30°$) yielded similar results with delay varying from 2-3 seconds.

$\beta = 90°$

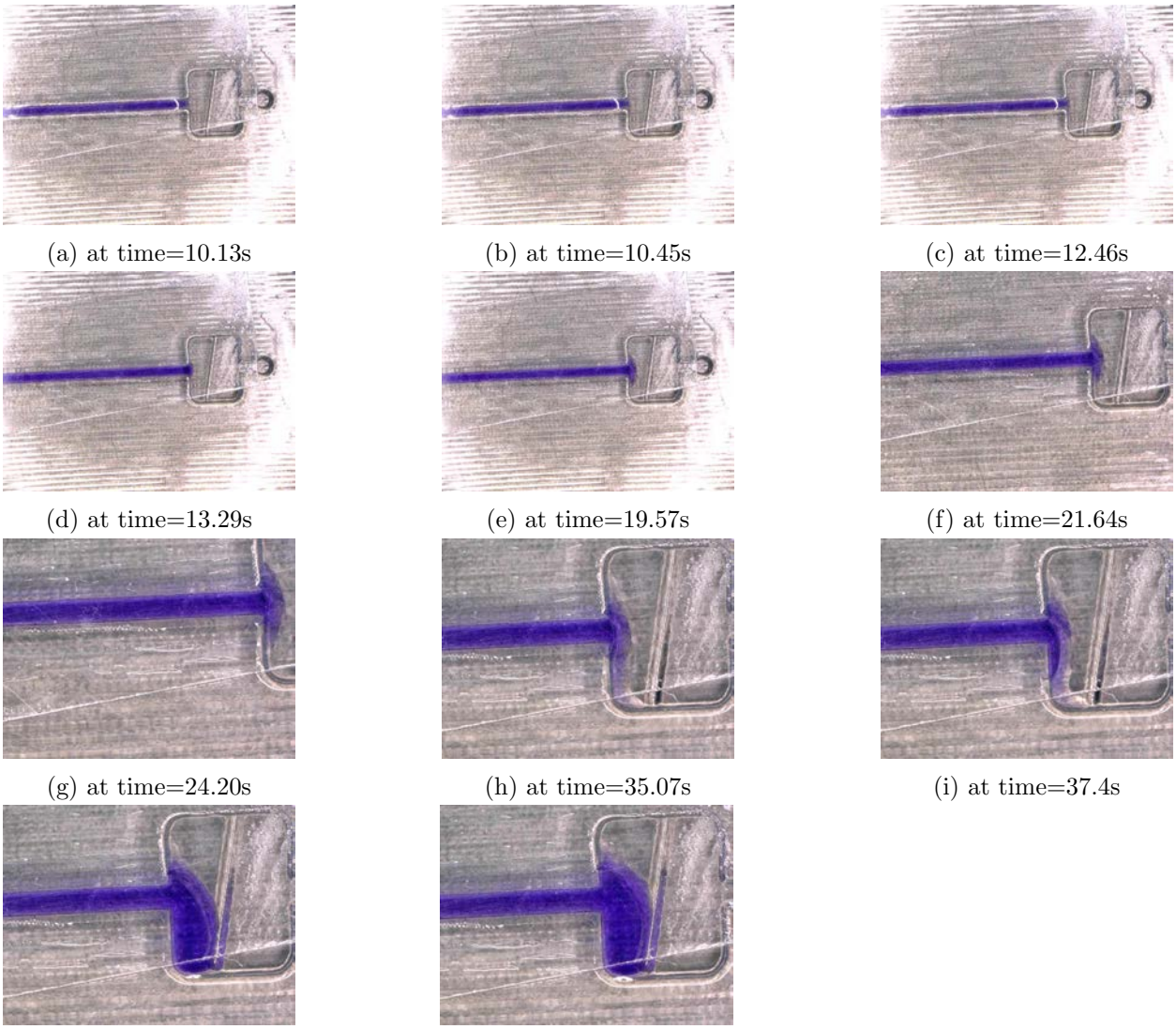

(a) at time=10.13s (b) at time=10.45s (c) at time=12.46s

(d) at time=13.29s (e) at time=19.57s (f) at time=21.64s

(g) at time=24.20s (h) at time=35.07s (i) at time=37.4s

(j) at time=38.45s (k) at time=40.20s

Figure 4.12: different phases of the liquid-air interface when it reaches a geometrical expansion with expansion angle $\beta = 90°$

From figures 4.12a to 4.12k it can be seen that the liquid pins at the expansion and then slowly expands. The delay in this case is much more as compared to the previous two results. The liquid pins for more than 25seconds at the expansion. In the case for $\beta = 90°$ the results for delay times in different experiments are not consistent. In some experiments the valve bursts quickly (within 10 seconds) whereas in other cases the valves pin the liquid meniscus at the expansion for minutes before bursting on its own. However, the self bursting of valves without any external pressure being applied for experiments done with the reservoir feature is a consistent observation.

$\beta = 120°$

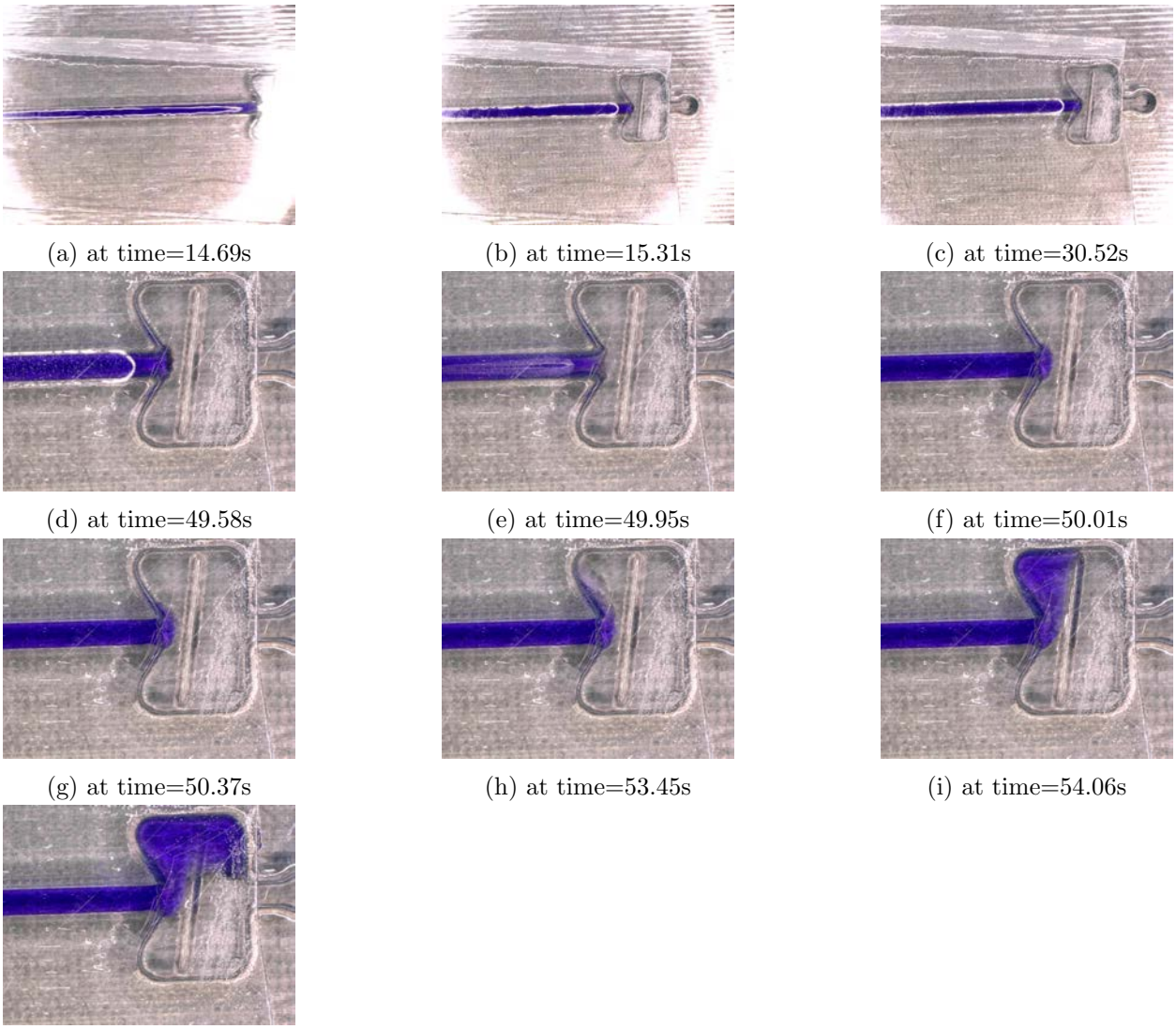

(a) at time=14.69s (b) at time=15.31s (c) at time=30.52s

(d) at time=49.58s (e) at time=49.95s (f) at time=50.01s

(g) at time=50.37s (h) at time=53.45s (i) at time=54.06s

(j) at time=55.08s

Figure 4.13: different phases of the liquid-air interface when it reaches a geometrical expansion with expansion angle $\beta = 120°$

From figures 4.13a to 4.13j it can be observed that the liquid pins at the expansion for around 40 seconds. The delay for $\beta = 120°$ is the maximum. Though the delay time varies in different experiments but it is observed that in all cases the delay time is maximum for $\beta = 120°$. This can also be related to pinning pressure as observed in the plots 4.24, 4.25, 4.26 and 4.27. The pinning pressure at the expansion is maximum for valves having $\beta = 120°$.

4.4.2 Valves without reservoir

In these set of experiments, the design does not have any reservoir to hold the liquid. The liquid is pipetted into the inlet and from there it wicks into the microchannel and progresses forward. The length of the microchannel is L=30mm and the volume pipetted into the inlet is $30\mu L$ ($5\mu L$ less as compared to experiments done with reservoir). It also needs to be noted that the total volume of the microsystem in terms of the volume of liquid it can hold is more for the devices used under these experiments. This has been discussed later after showing the results from all valve experiments. In these experiments different channel widths have been tested to observe the phenomena when the liquid-air interface reaches a geometrical expansion. Widths of $300\mu m$, $500\mu m$ and $800\mu m$ have been tested for different expansion angle (β) as discussed in section 3.4.

$\beta = 30°$

channels with $300\mu m$ width

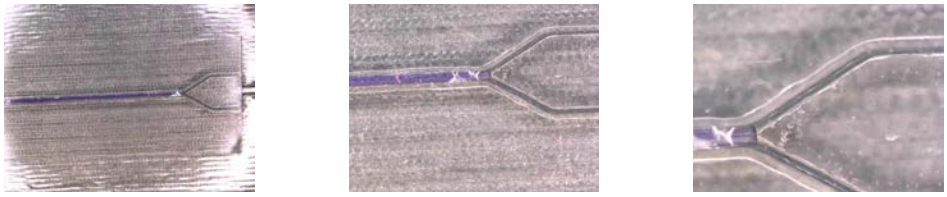

(a) interface at expansion, time=20.96s (b) interface pivots, time=32.16s (c) interface pins, time 92.06s

Figure 4.14: channel width=$300\mu m$ and expansion angle $\beta = 30°$

channels with $500\mu m$ width

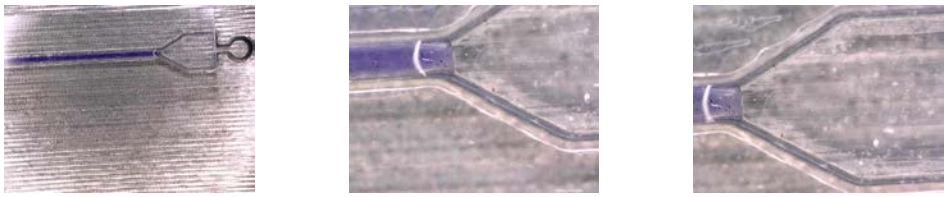

(a) interface at expansion, time=63.41s (b) interface pinned, time=76.81s (c) interface pinned, time=120.41s

Figure 4.15: channel width=$500\mu m$ and expansion angle $\beta = 30°$

channels with $800\mu m$ width

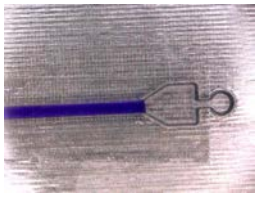

(a) Interface at expansion, time=13.68s

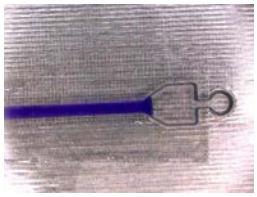

(b) interface expands, time=14.18s

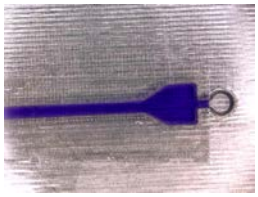

(c) liquid advances, time=16.25s

Figure 4.16: channel width=800μm and expansion angle $\beta = 30°$

$\beta = 60°$

channels with 300μm **width**

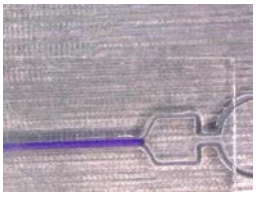

(a) interface at expansion, time=14.94s

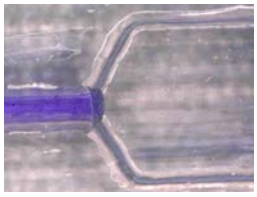

(b) interface pinned, time=190.0s

Figure 4.17: channel width=300μm and expansion angle $\beta = 60°$

channels with 500μm **width**

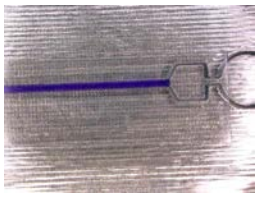

(a) interface pivots, time=7.73s

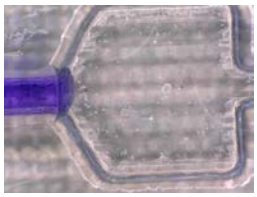

(b) interface pinned, time=40.09s

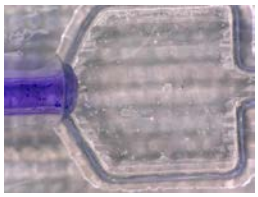

(c) interface pinned, time=127.13s

Figure 4.18: channel width=500μm and expansion angle $\beta = 60°$

channels with 800μm **width**

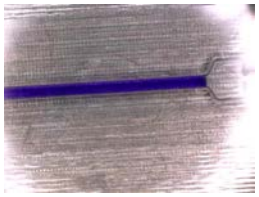

(a) interface pivots, time=7.73s

(b) interface expands, time=40.09s

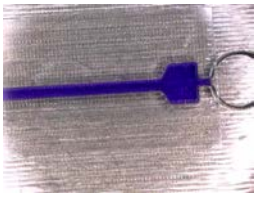

(c) liquid fills chamber,time=127.13s

Figure 4.19: channel width=800μm and expansion angle $\beta = 60°$

$\beta = 90°$

channels with 300μm **width**

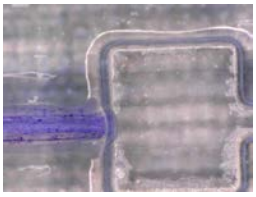

(a) interface pinned, time=125.0s

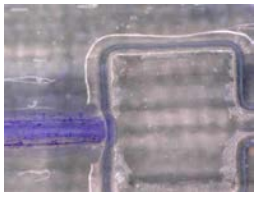

(b) interface pinned, time=180.0s

Figure 4.20: channel width=300μm and expansion angle $\beta = 90°$

channels with 500μm **width**

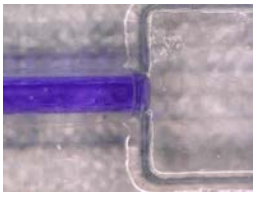

(a) Interface pinned, time=32.25s

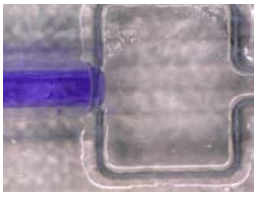

(b) interface pinned, time=120.05s

Figure 4.21: channel width=500μm and expansion angle $\beta = 90°$

Channels with 800μm **width**

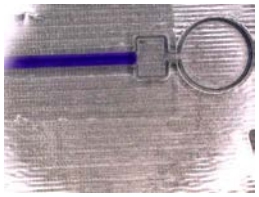

(a) Interface at expansion, time=8.79s

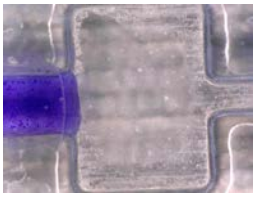

(b) Interface pinned, time=69.36s

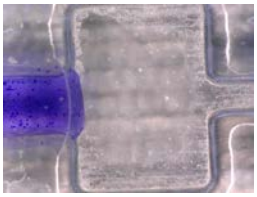

(c) interface pinned, time=221.46s

Figure 4.22: channel width=800μm and expansion angle $\beta = 90°$

$\beta = 120°$

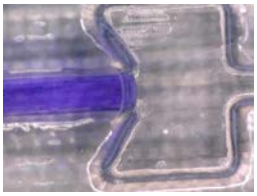

(a) Interface pinned, time=297s:channel width 500μm

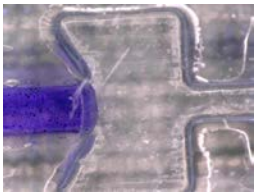

(b) liquid pinned, time=125s: channel width 800μm

Figure 4.23: expansion angle $\beta = 120°$ with channel widths 500μm and 800μm

Analysis

With the reservoir as mentioned earlier an extra pressure term adds up to the driving pressure. Though this term is quite small as compared to the driving capillary pressure but since the volume of the liquid pipetted into the reservoir is more than what the microsystem can hold it will lead to internal pressure being built in the device. The geometrical expansions in this case pins the liquid meniscus only temporarily where the valves act as delay valves and not stop valves. Whereas with designs without the reservoir the liquid meniscus pins for good (in most of the cases, refer table 4.5) as a pressure barrier develops at the expansion as mentioned in theory section 2.2, by applying external pressure as discussed next the pressure barrier is reduced and the liquid is triggered to advance forward. The plots in figures 4.24, 4.25 and 4.26 show how the driving pressure changes with length x in the design. These plots are made in MATLAB by using equations 2.6, 2.12 and 2.13. The channel length is 30mm and at x=30mm the channel expands into a chamber acting as a passive valve. The pinned pressure with different β and channel widths have been shown in the plots. 800μm wide channels require less external pressure to burst the valves, as can be observed in figure 4.26. For 800μm wide channels expanding into a chamber, the valve with expansion angles 30° and 60° acts as a delay valve as the liquid advances on its own without any external actuation. In table 4.5 the different observations from the studied images are listed. The observations for valves without reservoir is consistent as more than 10 experiments per design having same width and β are carried out and all of them bear the same result. The valves behave as stop valves for all cases except for 800μm wide channels having $\beta = 30°$ and $\beta = 60°$.

Table 4.5: Table depicting different observations for different parameters

Reservoir	**channel width**	**Expansion Angle**	**Delay or stop**
✓	$600\mu m$	$\beta = 30°$	Delay of 2 seconds
✓	$600mm$	$\beta = 60°$	Delay of 2 seconds
✓	$600mm$	$\beta = 90°$	Delay of 25 seconds
✓	$600mm$	$\beta = 120°$	Delay of 40 seconds
×	$300mm$	$\beta = 30°$	Stop
×	$500mm$	$\beta = 30°$	Stop
×	$800mm$	$\beta = 30°$	Delay of 1.5 seconds
×	$300mm$	$\beta = 60°$	Stop
×	$500mm$	$\beta = 60°$	Stop
×	$800mm$	$\beta = 60°$	Delay of 35-40 seconds
×	$300mm$	$\beta = 90°$	Stop
×	$500mm$	$\beta = 90°$	Stop
×	$800mm$	$\beta = 90°$	Stop
×	$300mm$	$\beta = 120°$	Stop
×	$500mm$	$\beta = 120°$	Stop
×	$800mm$	$\beta = 120°$	Stop

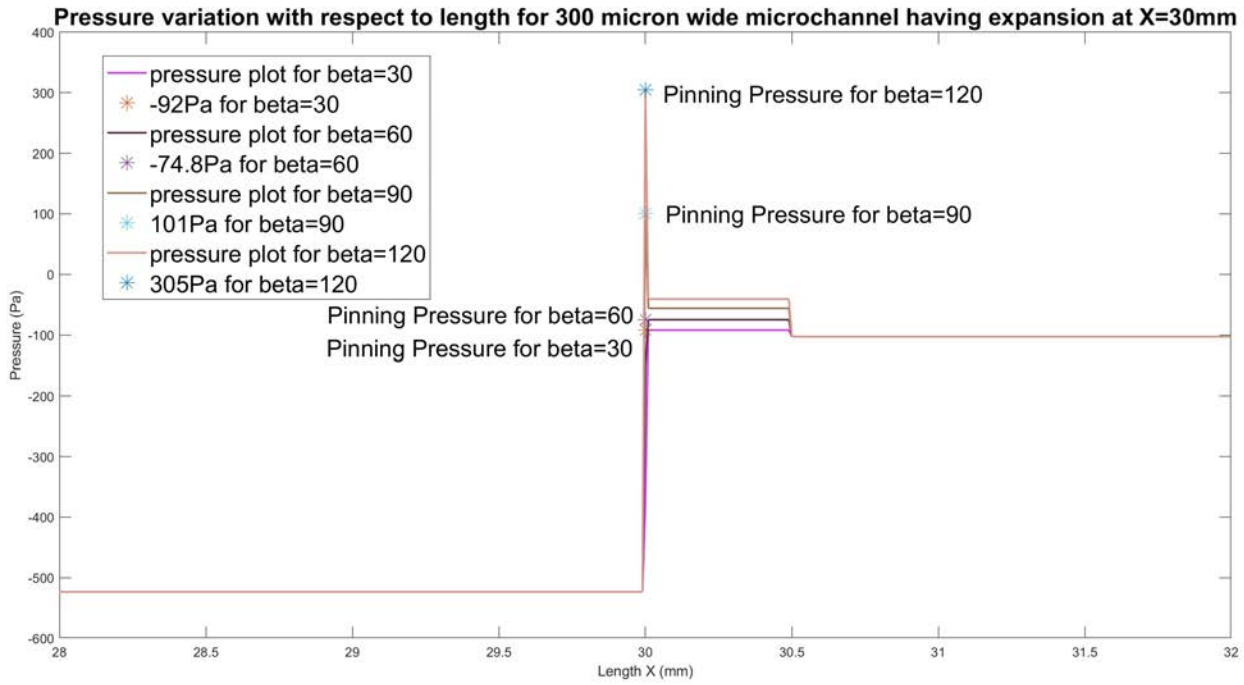

Figure 4.24: Driving Pressure plot in microfluidic device without reservoir with channel width $300\mu m$ and expansion at X=30mm

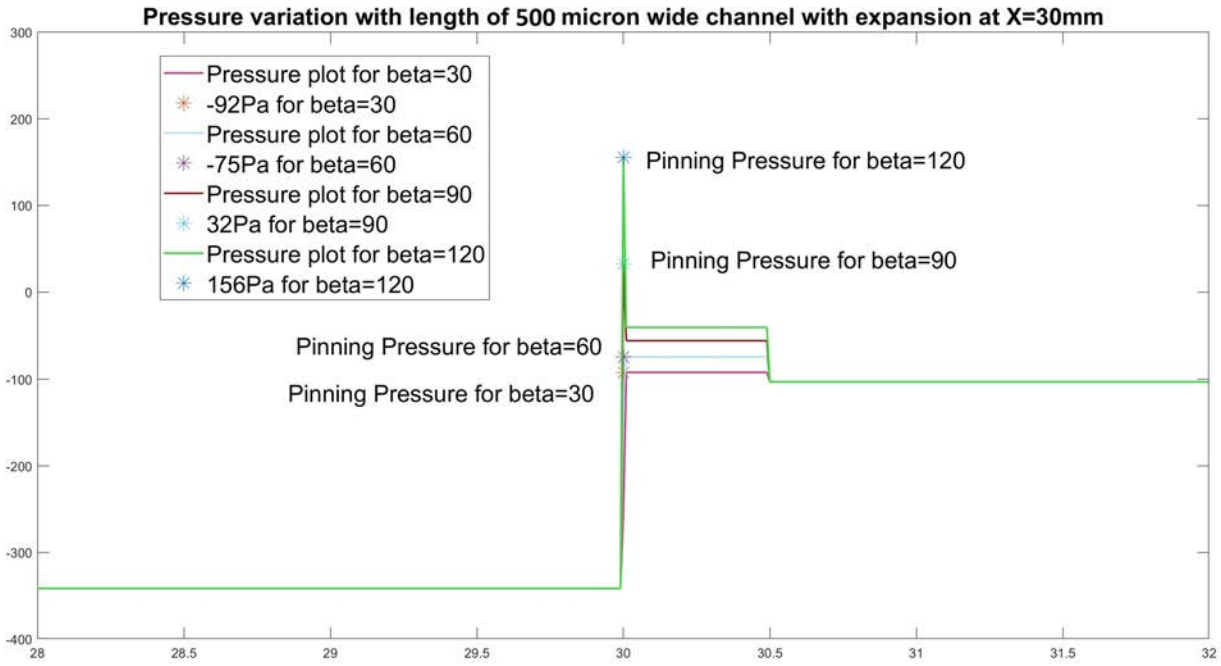

Figure 4.25: Driving Pressure plot in microfluidic device without reservoir with channel width $500\mu m$ and expansion at X=30mm

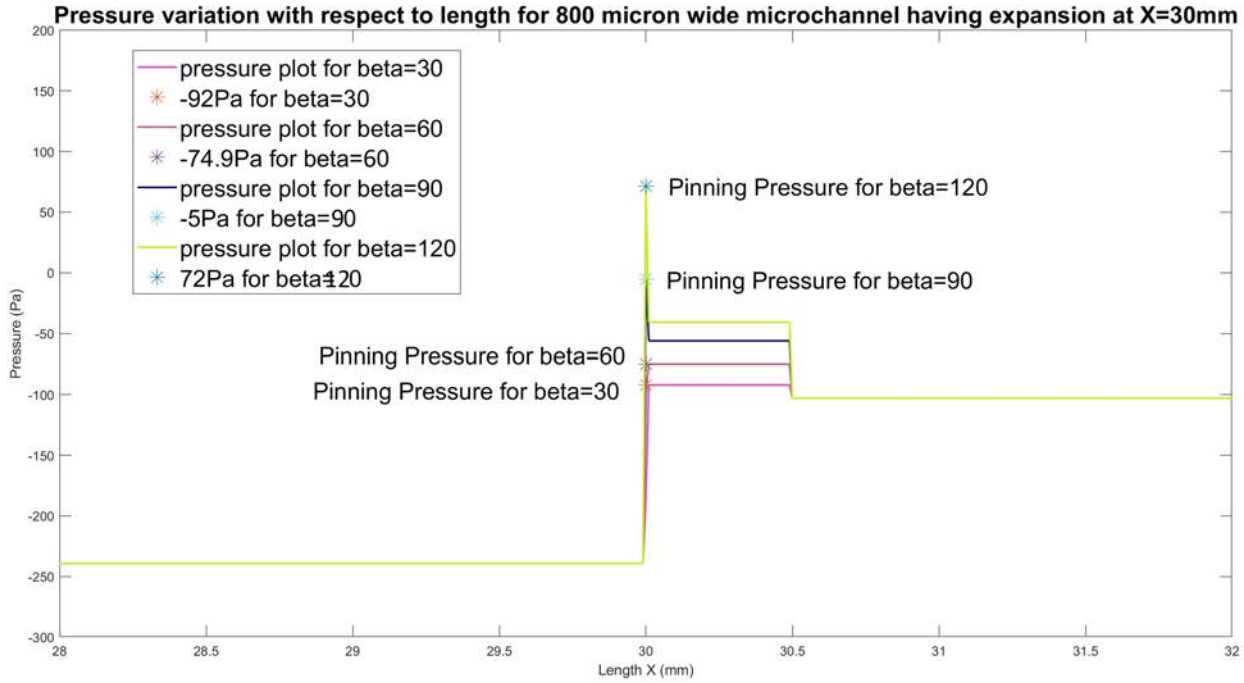

Figure 4.26: Driving Pressure plot in microfluidic device without reservoir with channel width $800\mu m$ and expansion at X=30mm

For the experiments done with a reservoir it was observed that the liquid does not instantly wick in the channels. The liquid is held in the reservoir for sometime and then rushes through the channels. The time measurement for experiments carried in section 4.2 is started when the liquid meniscus enters the channels. Figure 4.27 shows the pressure plot for valve with reservoirs having geometrical expansion at X=20mm. The reservoir decreases the positive pressure barrier at the expansion by $\approx 25Pa$. Theoretically the pinning pressure at the expansion for $\beta = 120°$ is 72 Pa (taking the resrvoir pressure into account). Hence, it can be inferred that this pressure is developed internally in the liquid over time ($\approx 40s$) which pushes the meniscus forward into the expansion. However, no study or research proves this observation. In appendix section C.3, experiment done with valve design with channel width $800\mu m$ and $\beta = 90°$ having geometrical expansion at X=3mm is shown.

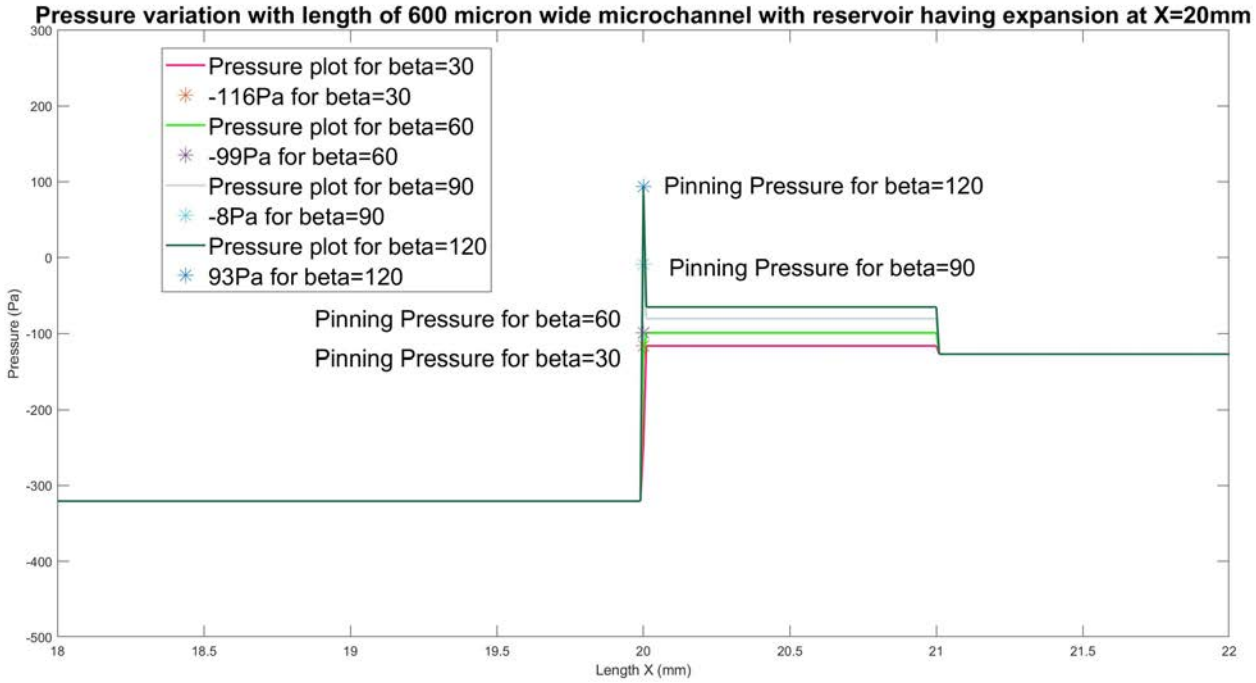

Figure 4.27: Caption

4.4.3 Pressure actuation with soft valves

As seen in experiments done without the reservoir feature, the liquid-air interface pins at the geometrical expansion acting as a stop valve for parameters and dimensions as seen in table 4.5. To actuate the pinned interface at the expansion an external pressure is required to overcome the pressure barrier. This can be done by using the soft valve property of the devices as discussed in 2.2.2. Since, the sealant is a hydrophobic tape which can be deformed on applying pressure reducing the depth and width of the expansion which will reduce the pressure barrier for the liquid at the expansion and the deformation will add a negative pressure drop which will wick the liquid-air interface into the expansion. In the next set of experiments the pinned liquid is actuated by applying some pressure at the pinned location with a PDMS puncher tip. It can be seen from figures 4.28a to 4.30c the liquid-air interface advances as the top sealing layer is deformed. However, the ampunt of pressure applied at the valve footprint or the deformation could not be quantified.

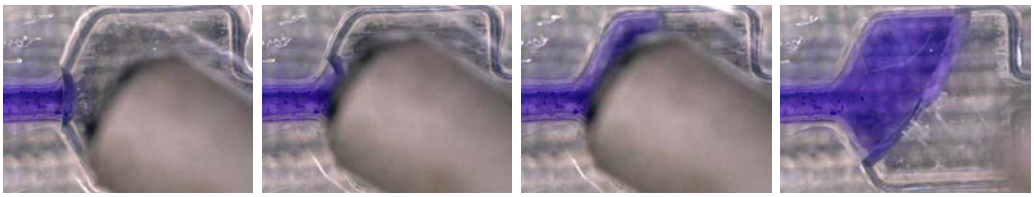

(a) time=144.24s (b) time=145.0s (c) time=146.56s (d) time=146.91s

Figure 4.28: actuation done for pinned liquid with $500\mu m$ channels and $\beta = 60°$ expansion angle

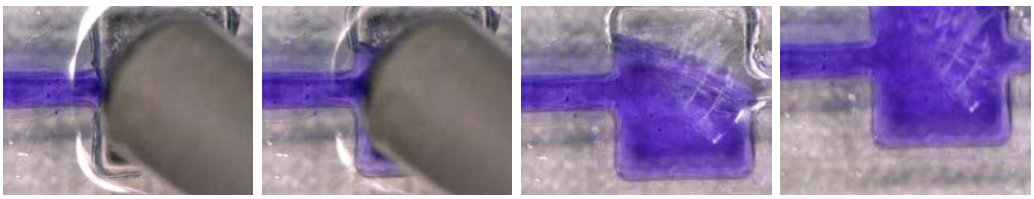

(a) time=127.59s (b) time=128.39s (c) time=128.59s (d) time=129.09s

Figure 4.29: actuation done for pinned liquid with $500\mu m$ channels and $\beta = 90°$ expansion angle

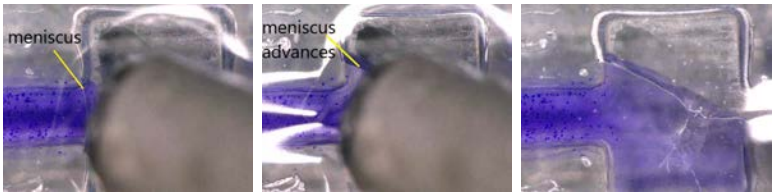

(a) time=227.99s (b) time=230.01s (c) time=231.0s

Figure 4.30: actuation done for pinned liquid with $800\mu m$ channels and $\beta = 90°$ expansion angle

4.5 Timing liquid flow using parallel channels with meniscus trigger microvalve

In this section the designs as shown in figures 4.31 and 4.33 are tested for timing the liquid by splitting the flow into two parallel channels and then merging the two paths to trigger the valve. The liquid filling front advances quickly in the fast channel and then pins at a geometrical expansion acting as a microvalve which is actuated by a meniscus trigger action from the liquid advancing from the slower channel having time delay structures. No external actuation step is required in this case as the liquid-triggers-liquid. The delay channels use the property of hydraulic flow resistance developed in the channels which is inversely proportional to the flow rate as shown in equation 2.9. The resistance depends on the width and depth of the rectangular channels as shown in equation 2.10. The liquid is split into two channels and the one flowing via the fast channel will get pinned at a geometrical expansion which acts as a valve (refer section 2.2.3). The liquid moving via the slow channel will progress through the delay structures as the pressure in the liquid-air interface in the channels still drives the liquid forward whereas for the pinned liquid interface the pressure barrier opposes advancement. The liquid movement depends on the driving pressure and resistance ratio as described in the article by Taher et al (2017) [29], since the pinned liquid needs to overcome the pressure barrier so the liquid will prefer to advance in the slow channels with delay structures . The liquid arriving later will trigger the pinned liquid at the expansion to move together into the mixing unit. As observed in section 3.4.4, the microvalves used in the design expand more from the faster channel. This is because the interface needs to be pinned at that location and slowly expand over time. The expanded inverted meniscus is triggered by the arriving liquid as observed in 4.34g and 4.34h.

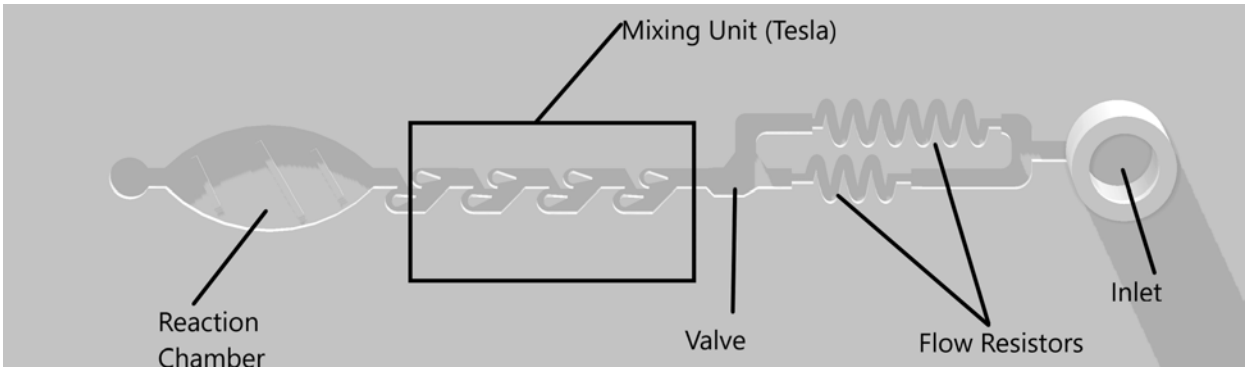

Figure 4.31: Delay Channel structure actuated with meniscus trigger

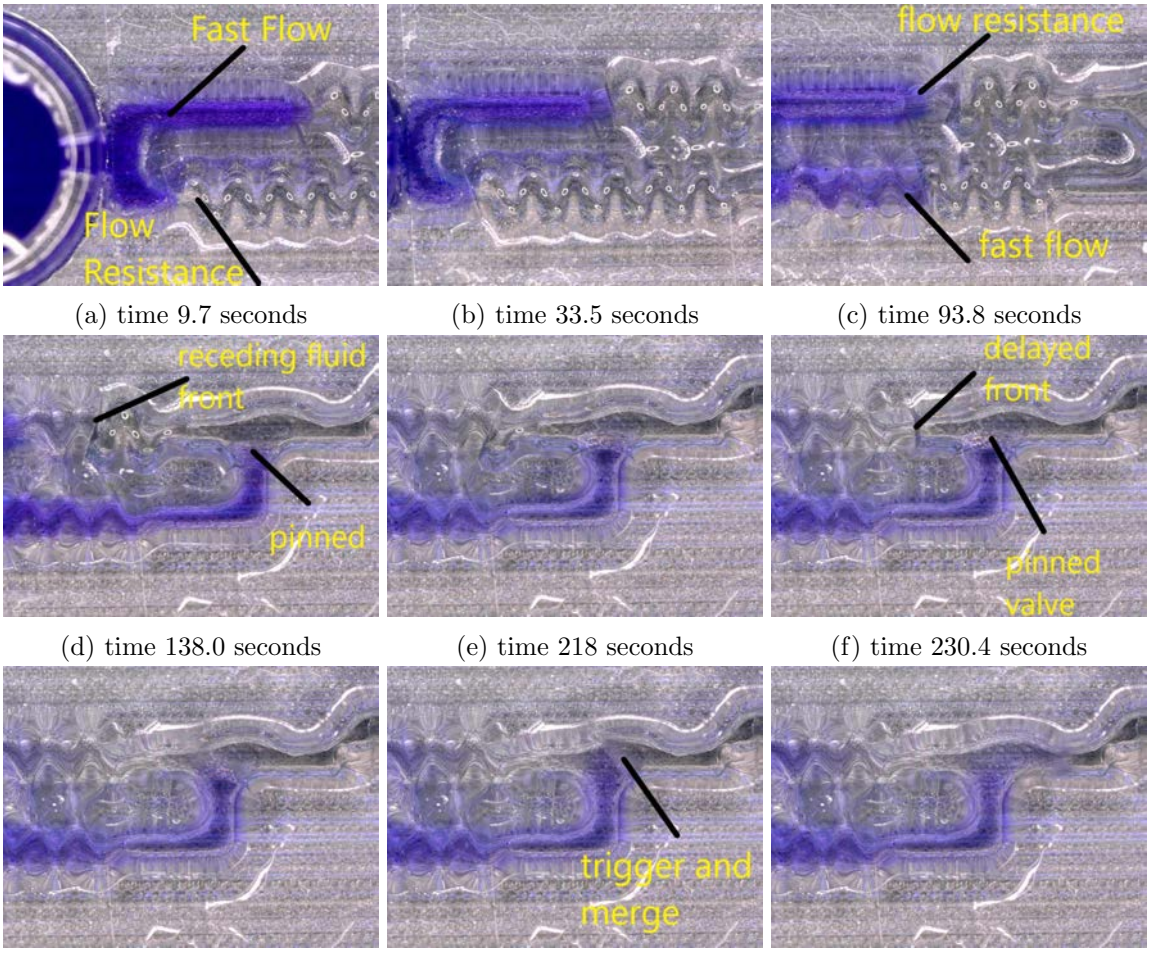

(a) time 9.7 seconds (b) time 33.5 seconds (c) time 93.8 seconds

(d) time 138.0 seconds (e) time 218 seconds (f) time 230.4 seconds

(g) time 231.0 seconds (h) time 231.05 seconds (i) time 231.2 seconds

Figure 4.32: Flow in delay channels and meniscus trigger

In the figure 4.32, we see the various phenomenons occurring. In figure 4.32a, the fluid moves faster in the wider channel as the resistance offered is quite less and when it reaches the delay structures the liquid starts to progress in the bottom channel as the flow rate obtained for liquid is more, this

can be seen in figure 4.32b. The liquid progressing in the bottom channel covers the entire length and is pinned at the geometrical expansion acting as a valve ,figures 4.32c and 4.32d. Since, the driving pressure is more in the top channel as compared to the burst pressure required to move the pinned liquid at the expansion so the upper channel starts filling slowly. In figure 4.32e the liquid progressing in the top channel can be seen. In figure 4.32f to 4.34h it is seen that the liquid pinned at the microvalve gets triggered from the slowly arriving liquid from the upper channel. In figure 4.34i it can be seen that they move together afterwards into the mixing unit (tesla mixers). Table 4.6 shows the progression of the liquid with time and the observations from the figures 4.32 are interpreted.

Table 4.6

Time	**Flow in Channel**	**Interpretation**
$0 - 9.7secs$	Channel 1	Flow in Wider channel
$33.5 - 138.0secs$	Channel 2	Liquid covers entire length of channel 2
$138.0 - 231.0secs$	Channel 1	Liquid pinned at channel 2 expansion, flow in channel 1
$231.05secs$	Meniscus trigger	two liquid phases merge and trigger the pinned liquid
$231.2secs$	Merge	two liquid phases merge and move together

Another experiment involving the meniscus trigger actuation done by splitting the liquid into two channels shows similar results. In this design the upper channel is the slow channel with flow resistor structures of width $300\mu m$ which cause time delay whereas the bottom channel is $500\mu m$ wide straight channel with no delay structures as shown in figure 4.33. This is a much simpler design as compared to the one used in the previous experiment and in this case we expect the trigger to occur in short time interval. We expect the liquid to travel really fast in the bottom channel and then pin at the geometrical expansion acing as a valve. The liquid in the top channel progresses slowly and then triggers the pinned liquid at the geometrical expansion. Then onward the liquids from the two channels merge and then progress together into the straight channel. The meniscus position at different times have been shown below in figure 4.34.

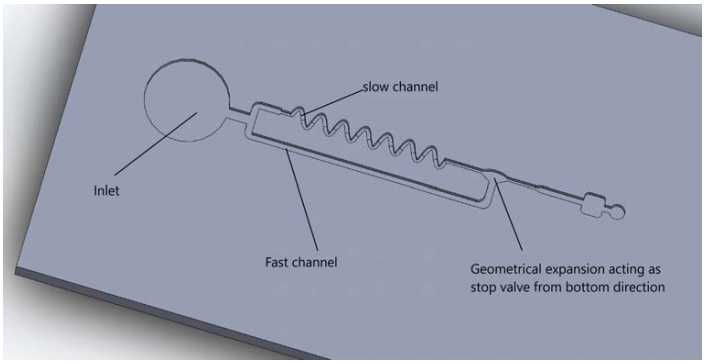

Figure 4.33: Design used for experiments of delay channels with meniscus trigger actuation

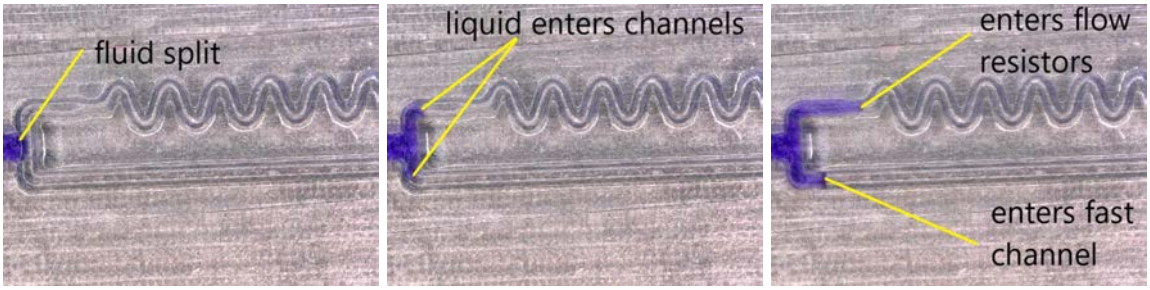

(a) fluid split marking t=0s

(b) t=0.42s

(c) t=0.66s

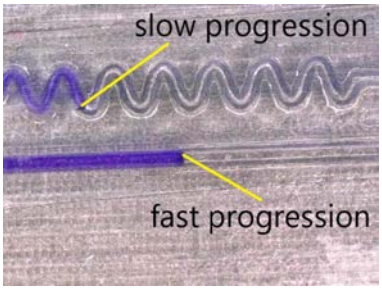

(d) t=1.95s

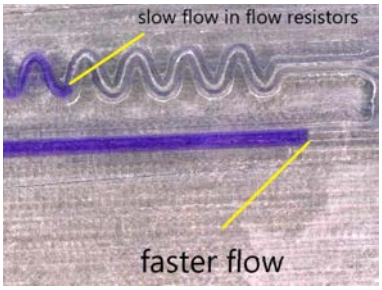

(e) t=3.09s

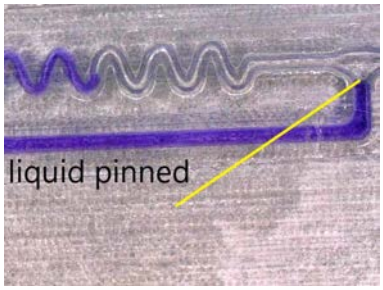

(f) t=3.73s

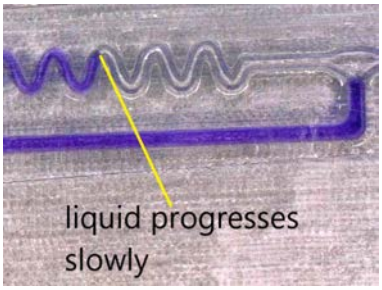

(g) t=3.87s

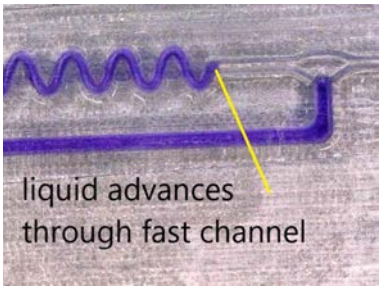

(h) t=6.06s

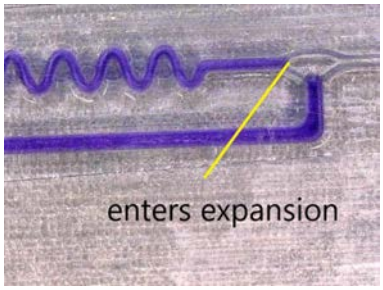

(i) t=6.44s

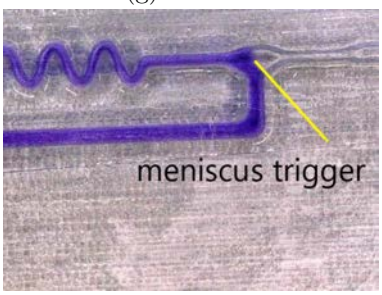

(j) t=7.52s

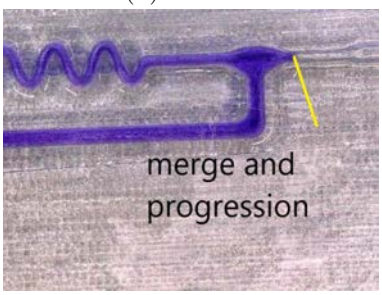

(k) t=7.58s

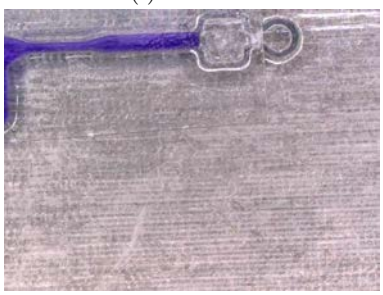

(l) t=9.09s

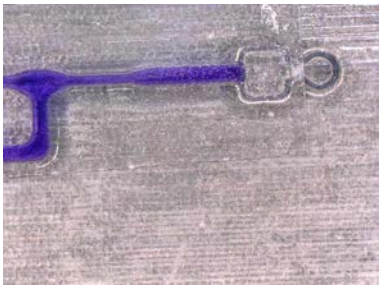

(m) t=25s

Figure 4.34: Flow in delay channels and meniscus trigger

Table 4.7 interprets the observations from figure 4.34 in an insightful way.

Table 4.7

Time	Flow in Channel	Interpretation
$0 - 0.66secs$	Channel 1 and channel 2	Flow in Wider channels
$0.66 - 3.72secs$	fast movement in channel 2	Liquid covers entire length of channel 2
$3.73secs$	Liquid pins at expansion in channel 2	slow movement in channel 1
$3.73 - 6.44secs$	liquid progresses slowly in channel 1	pinned liquid awaits trigger
$7.52secs$	Meniscus trigger	two liquid phases merge
$7.58secs$	Merger	two liquid phases progress together height

4.6 Phaseguides

Phaseguides as explained in theory section 2.3 are used to pin the liquid for sometime till the pressure required to move the liquid forward builds up. This has been a well studied and researched feature. This would be useful in the detection chamber of the POCT device where we do not want any voids due to corner-flows or air-bubble inclusions. Phaseguides act as delay valves, the liquid interface uniformly aligns before a phaseguide as seen in figure 4.35.

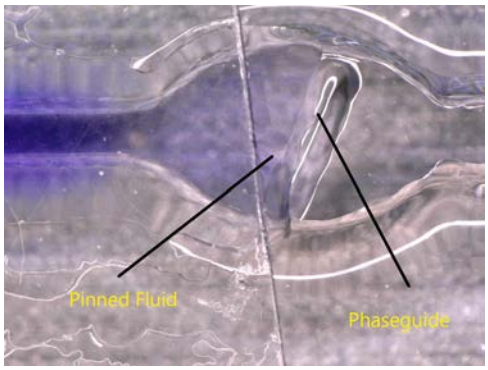

Figure 4.35: Phaseguides

The liquid aligns on the back of the phaseguide and stays there from time $198secs$ to $207secs$. The phaseguide pinning pressure calculated with equation 2.14 is shown in table 4.8 below. Another

Table 4.8

Width of Chamber	Height of Chamber	Height of Phaseguide	Pinning Pressure
$3.97mm$	$500\mu m$	$150\mu m$	$134Pa$

experiment with different chamber dimension shows the same result with the phaseguide structure. The liquid in this case also aligns with the phaseguide. The liquid stays in that position till the pinning pressure due to the phaseguide structure is reached. The chamber is 3mm long and 4mm wide as seen in the section 3.4.

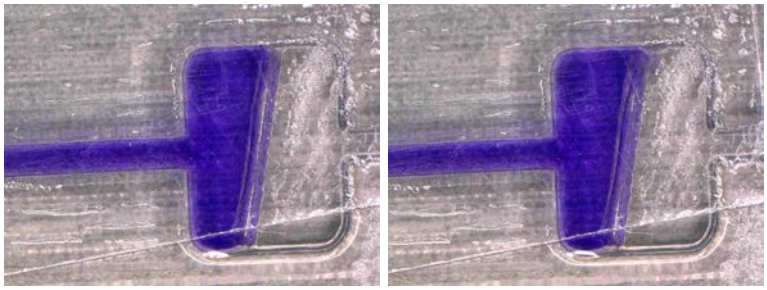

(a) time=42.23s (b) time=43.98s

Figure 4.36: Liquid aligning with phaseguide. After 43.98s the liquid advances forward

The pinning pressure due to the phaseguide using equation 2.14 is shown below in table 4.9. Despite

Table 4.9

Width of Chamber	**Height of Chamber**	**Height of Phaseguide**	**Pinning Pressure**
$4mm$	$500\mu m$	$150\mu m$	$135Pa$

the pinning pressure being quite high as shown in tables 4.8 and 4.9, the liquid aligns and pins at the phaseguide for sometime and then bursts to advance forward. This might be due to small void being created at the area where the phaseguide ridge touches the chamber walls. Since, the edges of the phaseguide are round because of the limitation of 3D printer so full contact with the wall is not possible. the liquid progresses via these valves. It is observed in multiple experiments that phaseguide bursting always occurs from the corners as seen in figure 4.37.

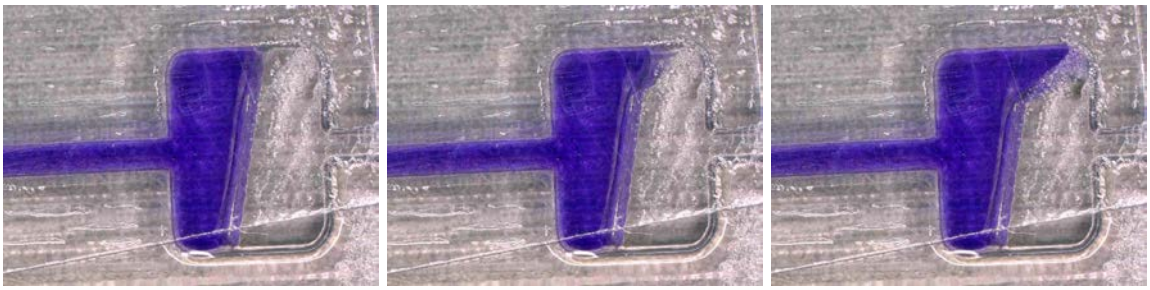

(a) (b) (c)

Figure 4.37: Liquid advances through the top corner of the phaseguide strcuture

The results obtained for different phaseguide experiments show consistency with some exceptions. Around 20 experiments were done using phaseguides in chambers of different widths. The parameters governing the pinning pressure due to phaseguide structure can be obtained using equation 2.14. The pinning pressure depends on the width of the chamber, ridge angle with the surface and height of phaseguide structure. Out of all these parameters only the width of the chamber is varied the rest of the parameters were kept same. In most of the cases phaseguide give a delay of 5 seconds on average but in few instances the liquid was pinned for minutes and even permanently pinned. The use of phaseguide structures in guiding the liquid flow and to align the liquid in a certain orientation for detections, reactions or dissolution to occur can be validated with these

set of experiments, however the pressure transition as is also the case with valves having different expansion angles (β) is still hard to explain.

Chapter 5

Conclusion

Proof-of-concept microfluidic devices fabricated with 3D printing technology with different functionalities like transporting, delaying, stopping, timing and triggering liquids in microchannels were developed and tested. These functionalities of capillary systems can bring the high-performances of microfluidic-based anaytical devices to near patient and environmental testing applications. The manipulation of liquid flow in the form of preventing corner-flow, pinning liquid interface at a specific location for few seconds to hours, delaying the liquid filling front with flow resistors, step-wise guiding the meniscus and to time a liquid using parallel microfluidic paths converging to a meniscus trigger microvalve can be done with 3D printing as shown with the set of experiments carried out in this project. These concepts will add functionality to passive microfluidic devices used for POCT applications. With the design freedom offered by 3D printing, complex capillary networks can be easily designed in a CAD software making the fabrication just a one step process from CAD file to an actual device in hand. With continuous development and progress being done in improving the resolution of the prints, material availability and fabrication of devices with consistency and uniformity makes 3D printing a strong contender for future projects in developing microfluidic systems for applications in Biological, chemical and environmental analysis.

All the microfluidic liquid manipulation concepts were developed and tested keeping in mind its application for the project 'Printing Makes Sense', in which a 3D printed microfluidic device was to be fabricated for detecting antibody concentration in a finger-prick blood sample (Volume$\leq 50\mu L$) with the help of biological sensors (LUMABS) developed in Chemical Biology lab of Eindhoven University of Technology (Arts et al,[1]). The model fluid used for experiments was not blood plasma but a dye-mixed water solution. For passively transporting the model fluid to different locations in device containing various reagents the functionality of the microchannels is tested. The theoretical prediction for the distance travelled by the liquid interface as a function of time for rectangular channels can be used as a rough approximation to design these channels. As seen in result section 4.2, the error percentage is really less for $300\mu m$ wide channels. More or less the error percentage is quite consistent for the experiments. In future it would be beneficial to use these optimized channel dimensions having least error with the theoretical predictions so that the time of transportation etc. can be approximated with theory. Another function used while designing capillary networks for POCT microlfuidic devices is to delay the liquid flow for the reagents to mix properly via diffusion. The use of flow resistors proves quite handy as the progression of the

liquid is slowed down with meandering channels. Providing a constriction or enlargement in the channel also act as flow resistors and decrease the velocity of the liquid, Berthier et al (2016) [28]. As shown in the figures of section 4.3, the liquid progression rate is substantially decreased. These flow resistors can keep the reagents in the channels for a long time as explained in 2.1.6 and 3.4.2. With the help of these flow resistors separate incubation step for immunoassays is not required. Passive valves are essential components for capillary microfluidic systems to control the sequence of bio/chemical analyses. The liquid can be pinned at an abrupt geometrical expansion for few seconds, minutes or hours. They are easy to fabricate with 3D printing and have been studied in detail in section 2.2 and results in 4.4 where different channel widths expanding into a valve with different expansion angles have been tested. The effect of reservoir on the delay or stoppage of the liquid filling front is also observed. Although, its empirical effects have been documented before but its physical understanding and transition of pressures is far from complete. However, from the results obtained from the section 4.4 it can be noted that the liquid can be stopped or delayed depending on the expansion angle β (refer section 2.2) and channel width at a specific location in the device. Greater the β value, more abrupt is the expansion, leading to positive pressure barrier being developed which will oppose the liquid interface from advancing. With advancement in deposition techniques like inkjet printing, the reagents can be deposited at a particular location where with abrupt geometrical expansion incoming sample liquid can be pinned for desired amount of time. This will give time for the reaction or mixing to occur. No extra incubation step needs to be provided and with soft-valve actuation as studied in 4.4.3 the pinned liquid can be triggered to flow into the expansion. The liquid progression can be controlled in steps for example if the sample fluid needs to first react with reagent 1 and after 15 minutes with reagent 2 then the liquid will first pin at the first expansion where reagent 1 is present, after staying for 15 minutes the valve can be actuated by applying pressure on the top of the expansion and then the pinned interface will progress towards the second expansion where reagent 2 is present where it can be triggered again in the same manner after 15 minutes. The triggering of the pinned liquid interface can also be made an automated process as seen in 4.5 where the valve does not need to be actuated by applying any external pressure. This result has been tested numerous times ($\approx 20 - 25$) over the span of this project and results have been consistent. Optimizing the delay path, channel width, microvalve design and channel lengths the result can be reproduced. Thus, the pinning and trigger can be timed in this way. Use of phaseguides to guide the liquid meniscus and to avoid corner-flow and non-uniform jumps etc. 4.6 proves quite useful in giving small delays and also to uniformly align the mixture in detection chambers where detection can be done optically or chemically.

From the results obtained in accordance with the background theory and previous works by researchers it can be concluded that 3D printed microfluidic devices can prove to be a versatile platform for one-step immunoassay and other POCT applications. Complex capillary circuits, mixing units, flow resistors and valves can be designed easily with a CAD software and then can be printed with high resolution. Further, the devices need to be tested with blood plasma, antibodies and biological sensors to further validate the microfluidic concepts described above.

Chapter 6

Recommendations

For future it would be a good practice to simulate the liquid flow in 3D printed devices with CFD analysis using simulation softwares like Ansys or COMSOL MultiPhysics. It will give better approximation for the distance covered by the liquid filling-front with respect to time as well as the flow velocity at different spatial points in the channel. The experimental results can then be compared with the numerically computed ones and then analysed for discrepancies.

The sealant used for testing these devices is a simple fix but not an ideal solution. Since, for the project "Printing makes sense", the biological sensors along with other reagents are to be incorporated onto the device with inkjet printing, so open microfluidic devices were printed and then sealed with a well-plate tape as it adheres well to the printed top surface, is inert and does not result in leakage as was the case when double-sided tapes and mechanical bolts were used to bind the cover-plate (refer section 3.3). The tape is hydrophobic and with rounding of the corners of the top edge of the rectangular microchannels (a limitation of 3D printing) it does not completely cover the top of the microchannel leaving some voids. The progressing liquid enters these voids as these act as small capillaries. This also slows down the progression rate of the liquid filling-front. Another phenomena observed with these tapes was that the top surface of the liquid moves much slower than the bottom surface (refer section 2.1.4). As the top layer is in contact with a hydrophobic surface which opposes the liquid-air interface to move forward because of positive resisting pressure being developed ($\theta_c > 90°$), so due to viscous forces being developed the liquid progression is non-uniform and thus, the time taken for the liquid filling-front to cover the desired length is much more as compared to the theoretically predicted value. Due to this phenomena the capillary pressure calculation formula as used in equation 2.6 will be effected as the meniscus curvature (R_1 and R_2) cannot be approximated in the manner done earlier. This is also one of the reasons for higher error percentage with higher microchannel widths. Hydrophilic tapes or monolithic devices would be a good solution for future use. In the article by MIT researcher Beckwith et al (2018) [25], monolithic 3D printed microfluidic device for recapitulation of Dynamic Tumor Microenvironments was developed. The device did not require any additional sealing or cover-plate.

The contact angle as used to calculate the capillary pressure in the channels is assumed to be same as the equilibrium contact angle which is not correct. Measuring the dynamic contact angle with Keyence VHX-5000 microscope when the liquid meniscus is progressing and then taking the average of different values of these measured dynamic contact angles at different points for calculating the

capillary pressure would reduce the error percentage. The method used for coating the prints with Pluronic F-127 is quite primitive. The prints are immersed in the Pluronic coating solution for 2-days. However, this may lead to non-uniformity as it might be possible that some hard to reach areas like microchannels and grooves will not be coated properly. Sometimes the parts are not uniformly coated with this technique as during contact angle measurements few outlier values are observed. When the liquid flow is studied under Keyence VHX-5000 microscope the meniscus appears flat or less concave in some regions as compared to others, this indicates that the dynamic contact angle of the liquid with the solid substrate is not consistent. Hence, better coating methods need to be adapted for this purpose. With developments in inkjet printing, CVD (chemical vapor deposition) and PVD (physical vapour deposition) techniques the devices can be coated uniformly. Since, the transition of driving pressure when the liquid arrives at a certain geometrical expansion acting as a valve is still not clear it would be good to test the pressure required to actuate the soft-valve with a pressure sensor (Inline pressure sensor by Elveflow) . This pressure can then be compared to the pinning pressure value as theoretically calculated in plots shown in section 4.4. A lot of internal pressure sensors can also be used to determine the pressure being build up in the liquid particles. Pressure analysis of the valves will be insightful and will help in framing concrete dynamics of the liquid-air interface at the expansion which can further be used to design future devices for actual POCT applications.

Bibliography

[1] *Arts, R., Ludwig, S. K. J., van Gerven, B. C. B., Estirado, E. M., Milroy, L. G., and Merkx, M. (2017). Semisynthetic bioluminescent sensor proteins for direct detection of antibodies and small molecules in solution. ACS Sensors, 2(11), 1730-1736. DOI: 10.1021/acssensors.7b00695*

[2] *Arts, R., den, H. I., Zijlema, S. E., Thijssen, V., van, . B. S. H., and Merkx, M. (January 01, 2016). Detection of Antibodies in Blood Plasma Using Bioluminescent Sensor Proteins and a Smartphone. Analytical Chemistry, 88, 8, 4525-32.*

[3] *van, R. M., Ni, Y., Vervoort, D. F. M., Arts, R., Ludwig, S. K. J., and Merkx, M. (February 06, 2018). Dual-Color Bioluminescent Sensor Proteins for Therapeutic Drug Monitoring of Antitumor Antibodies. Analytical Chemistry, 90, 5, 3592-3599.*

[4] *S.Mukherji, D.Mondal (2017). Lab-on-Chip (LOC) Devices for Point-of-Care (POC) applications.*

[5] *Daniel Mark, Stephen Haeberle, Gunter Roth, Felix Von Stetten and Roland Zengerle (25th January,2010). Microfluidic Lab-on-a-chip platforms:requirements, characteristics and applications*

[6] *Mitra, D. (2013). Microfluidic Modules for Enabling Point-of-Care Biopsy-based Cancer Diagnostics.*

[7] *Ayokunle Olanrewaju,Maiwenn Beaugrand,Mohamed Yafia and David Juncker (August 21, 2018). Capillary microfluidics in microchannels:from microfluidic networks to capillaric circuits*

[8] *Jean Berthier, David Gosselin, Noemie villard, Catherine PUDDA, Francois Boizot, Guillaume Costa, Guillaume Delapierre (28 November,2014). The Dynamics of Spontaneous Capillary Flow in Confined and Open Microchannels*

[9] *Die Yang, Marta Krasowska, Craig Priest, Mihail N. Popescu, and John Ralston. Dynamics of Capillary-Driven Flow in Open Microchannels*

[10] *Y. Zhu, K. Petkovic-Duran (September 28, 2009). Capillary flow in Microchannels*

[11] *Arman Javadi, Mehdi Habibi, Fereshte Samadi Taheri, Sebastien Moulinet & Daniel Bonn (4 Febraury,2013).Effect of wetting on capillary pumping in microchannels.*

[12] *Zisman, W. A., Fowkes, F. M., American Chemical Society., & American Chemical Society. (1964). Contact angle, wettability, and adhesion: The Kendall award symposium honoring William A. Zisman.*

[13] *Kruss Scientific (1999). Model for Surface energy calculation.*

[14] *Shakhmin, A., Hall, M. P., Machleidt, T., Walker, J. R., Wood, K. V., Kirkland, T. A. (October 18, 2017). Coelenterazine analogues emit red-shifted bioluminescence with NanoLuc Electronic supplementary information (ESI) available. See DOI: 10.1039/c7ob01985h. Organic Biomolecular Chemistry, 15, 40, 8559-8567.*

[15] *P.F.Man, C.H. Mastrangelo, M.A.Burns and D.T.Burke,Center for Integrated Sensors and Circuits Department of Electrical Engineering and Computer Science, Department of Chemical Engineering Department of Human Genetics University of Michigan, Ann Arbor, MI 48109-2122, USA (1998). Microfabricated capillarity-driven stop valve and sample-injector*

[16] *B.Eker,M.Hitzbleck,R.D.Lovchik,Y.Temiz and E.Delmarche. IBM Research GmbH,Saumerstrasse 4,8803 Ruschlikon,Switzerland, A Microfluidic Architecture for efficient Reagent integration, Reagent release and Analyte detection in limited sample volume*

[17] *Hansang Cho*, Ho-Young Kim†, Ji Yoon Kang*, and Tae Song Kim* *Microsystem Research Center, †Thermal/Flow Control Research Center Korea Institute of Science and Technology, Seoul 136-791, Korea. Capillary passive valve in microfluidic systems*

[18] *Martina Hitzbleck and Emmanuel Delamarche,IBM Research-Zurich,2013. Advanced Capillary Soft Valves for Flow control in Self-Driven Microfluidics*

[19] *Jessica Melin,KTH Stockholm, 2004. Novel Microsystem Techniques for Liquid Manipulation and Pressure Sensing*

[20] *Paul Vulto,Susann Podsun, Philipp Meyer, Carsten Hermann, Andreas Manz and Gerald A.Urban,2011. Phaseguides: a paradigm shift in microfluidic priming and emptying*

[21] *Francesca Garbarino, Kasper Kistrup, Giovanni Rizzi and Mikkel Fougt Hansen, DTU Nanotech, Technical University of Denmark, 2017. Burst pressure of phaseguide structures of different heights in all-polymer microfluidic channels*

[22] *Ender Yildirim, Sebastiaan J. Trietsch, Jos Joore, Albert van den Berg, Thomas Hankemeier and Paul Vulto,2014. Phaseguides as tunable passive microvalves for liquid routing in complex microfluidic networks.*

[23] *Ender Yildirim, Cankaya University,2016. Modelling and Analysis of a Microfluidic Capillary Valve*

[24] *Edward W. Washburn,1921. The Physical Review- The Dynamics of capillary flow*

[25] *Beckwith, A. L. (January 01, 2018). Monolithic, 3D-Printed Microfluidic Platform for Recapitulation of Dynamic Tumor Microenvironments. Journal of Microelectromechanical Systems, 27, 6, 1009-1022.*

[26] *Hampson, S. M., Rowe, W., Christie, S. D. R., Platt, M. (March 01, 2018). 3D printed microfluidic device with integrated optical sensing for particle analysis. Sensors and Actuators, B: Chemical, 256, 1030-1037.*

[27] *Samper, I. C., Gowers, S. A. N., Rogers, M. L., Murray, D.-S. R. K., Jewell, S. L., Pahl, C., Strong, A. J., ... Boutelle, M. G. (January 01, 2019). 3D printed microfluidic device for online detection of neurochemical changes with high temporal resolution in human brain microdialysateElectronic supplementary information (ESI) available. See DOI: 10.1039/c9lc00044e. Lab on a Chip, 19, 11, 2038-2048.*

[28] *Berthier, J., Gosselin, D., Pham, A., Delapierre, G., Belgacem, N., Chaussy, D. (January 26, 2016). Capillary Flow Resistors: Local and Global Resistors. Langmuir, 32, 3, 915-921.*

[29] *Taher, A., Jones, B., Fiorini, P., Lagae, L. (January 01, 2017). A valveless capillary mixing system using a novel approach for passive flow control. Microfluidics and Nanofluidics, 21, 8, 1-10.*

[30] *Kim, S.-J., Lim, Y. T., Yang, H., Kim, K., Kim, Y. T. (February 01, 2010). Passive regulation of volume-flow ratio for microfluidic streams with different hydrophilicity and viscosity. Electrophoresis, 31, 4, 709-713.*

[31] *Safavieh, R., Juncker, D. (November 07, 2013). Capillarics: Pre-programmed, self-powered microfluidic circuits built from capillary elements. Lab on a Chip - Miniaturisation for Chemistry and Biology, 13, 21, 4180-4189.*

[32] *Gervais, L., de, R. N., Delamarche, E. (June 24, 2011). Microfluidic Chips for Point-of-Care Immunodiagnostics. Advanced Materials, 23, 24.)*

[33] *Au, A.K.; Lee, W.; Folch, A. Mail-order microfluidics: Evaluation of stereolithography for the production of microfluidic devices. Lab Chip 2014, 14, 1294–1301.*

[34] *Sharafeldin, M., Jones, A., Rusling, J. F., Sharafeldin, M., Rusling, J. F., Rusling, J. F., Rusling, J. F. (August 07, 2018). 3D-printed biosensor arrays for medical diagnostics. Micromachines, 9, 8.)*

[35] *Macdonald, N. P., Cabot, J. M., Smejkal, P., Guijt, R. M., Paull, B., Breadmore, M. C. (January 01, 2017). Comparing Microfluidic Performance of Three-Dimensional (3D) Printing Platforms. Analytical Chemistry, 89, 7, 3858-3866.*

[36] *Alistar, M. (January 01, 2019). Mobile Microfluidics. Bioengineering (basel, Switzerland), 6, 1.)*

[37] *Rogers, C. I., Qaderi, K., Woolley, A. T., Nordin, G. P. (January 01, 2015). 3D printed microfluidic devices with integrated valves. Biomicrofluidics, 9, 1.)*

[38] *Gowers, S. A. N., Curto, V. F., Seneci, C. A., Wang, C., Anastasova, S., Vadgama, P., Yang, G.-Z., ... Boutelle, M. G. (January 01, 2015). 3D Printed Microfluidic Device with Integrated Biosensors for Online Analysis of Subcutaneous Human Microdialysate. Analytical Chemistry, 87, 15, 7763-7770.*

[39] *Sander van den Driesche, Frieder Lucklum, Frank Bunge, Michael J. Vellekoop. (January 01, 2018). 3D Printing Solutions for Microfluidic Chip-To-World Connections. Micromachines, 9, 2.)*

[40] *Risch, P., Kotz, F., Helmer, D., Rapp, B. E., Microfluidics, BioMEMS, and Medical Microsystems XVII 2019. (January 01, 2019). 3D printing of highly fluorinated methacrylates for the rapid prototyping of transparent and chemically-resistant microfluidic devices. Progress in Biomedical Optics and Imaging - Proceedings of Spie, 10875.*

[41] *Kim, Y., Castro, K., Bhattacharjee, N., Folch, A. (March 14, 2018). Digital Manufacturing of Selective Porous Barriers in Microchannels Using Multi-Material Stereolithography. Micromachines, 9, 3, 125.*

[42] *Akbari, M., Sinton, D., Bahrami, M. (January 01, 2009). Pressure Drop in Rectangular Microchannels as Compared With Theory Based on Arbitrary Cross Section. Journal of Fluids Engineering, 131, 4, 41202.*

Appendices

Appendix A

LUMABS

A.1 LUMABS and BRET interference

A novel ratiometric bioluminescent sensor molecule for suitable antibody detection called LUMABS has been developed at the Chemical-Biology department of TU/e (Arts et al,2016) [2]. The detection mechanism is based on the shift in emitted wavelength and corresponding colour change [3](M.Merkx et al,2018). Using smartphone, the researchers were able to detect antibody concentrations down to the picomolar range. The LUMABS detection has been quite efficient in well-plates but would also be suitable for integrating the mechanism in a microfluidic Point-of-care testing device.

Luciferase catalyzes the oxidation of furimazine(substrate) which produces luminescense ([14] Mary P. Hall et al,2012). The LUMABS system comprises of luciferase enzyme (NanoLuc, emits blue light) which is coupled by a flexible epitope linkage to a mNeonGreen protein that emits green light when energy transfer (BRET) with luciferase as a donor occurs (fig A.1).When the interaction between NanoLuc and mNeonGreen is broken, the emitted light will shift from green-blue to blue. The latter is possible because specific epitopes that are recognized by antibodies whose concentration we need to measure will bind to the epitope linkage resulting in disruption and disassembly of the BRET partners, causing a shift in the wavelength of emitted light. The modular design of the LUMABS makes it relatively easy to adapt them to different types of antibodies, by modifying the epitope sequences and no further optimization of the sensor is required. In this way multiple antibody types can be detected [2](Arts et al,2016).

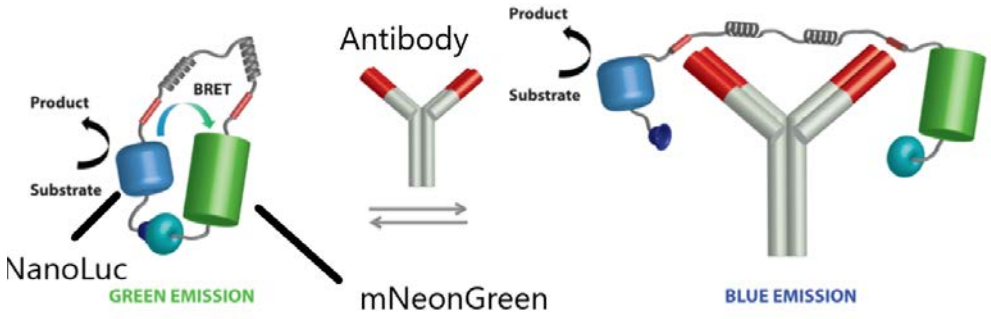

Figure A.1: LUMABS system with binding of antibody to the epitope linkage resulting change in configuration and interrupting the BRET interference

The image A.1, shows how the reaction happens. The antibody binds to the LUMABS system and the distance between the donor luciferase and mNeonGreen changes resulting in the wavelength shift of the emitted spectrum. The colour changes from green-blue to blue. The reaction happens in the presence of the substrate Furimazine as mentioned earlier.The enzyme NanoLuc acts as a donor and catalyzes the oxidation of Furimazine giving blue colored luminescence with peak at 460 nm, this energy is tranferred to the mNeonGreen(BRET) protein which gives brighter green colored luminescence with the peak of the emission spectrum at 517 nm, figure A.2.

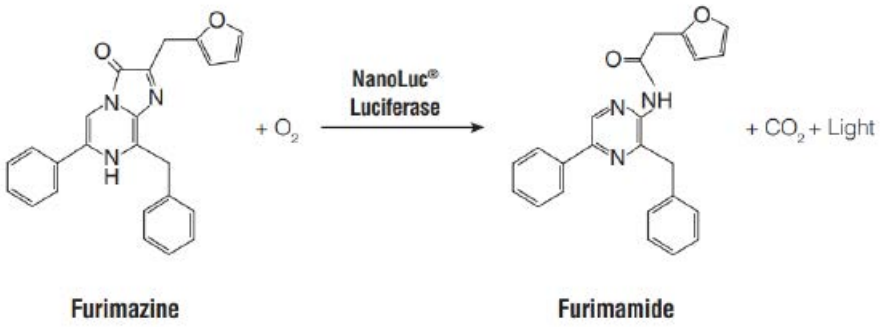

Figure A.2: Oxidation of Furimazine into Furimamide in the presence of NanoLuc Luciferase enzyme giving light emissions

This reaction is an equilibrium reaction, so the concentration of the substrate should be enough to shift the reaction forward and to get a stable signal for long. The shift can be very well detected with a Smartphone camera and the concentration can be measured with respect to the intensity of the signal, figureA.3.

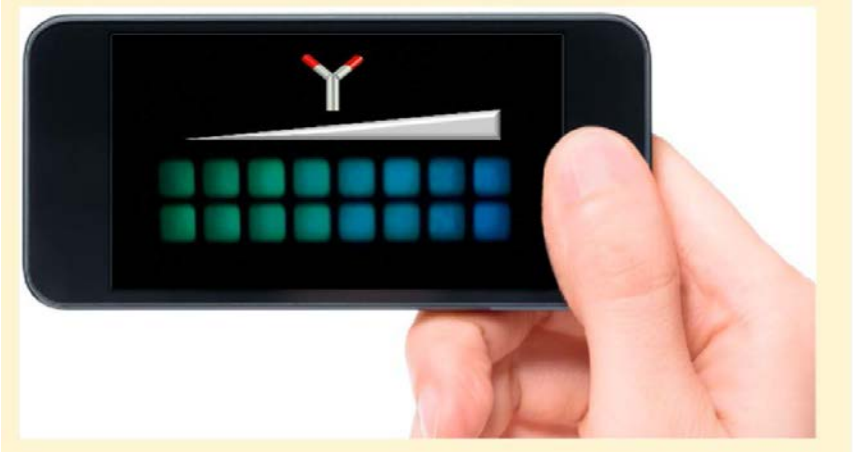

Figure A.3: Shift in color due to the interruption of BRET partners with binding of antibodies measured with a smartphone camera

A.2 Incorporating LUMABS reagents on Microfluidic Devices

The above-mentioned detection mechanism would be entrancing to test on a microfluidic device because of the high light output, sensitivity and relative simplicity of detection on doing the assay. The advantage of a microfluidic device is to transport the testing fluid of very small volume passively, reagent requirement is also very less, low-cost, high production and ease of disposability. The reagents which are the seonsor molecules (LUMABS system:NanoLuc,mNeonGreen and eptiope linkage) and the substrate molecules (Furimazine) can be deposited onto the device with depositing techniques like inkjet printing on the desired testing areas and the testing fluid can be transported passively (capillary action) via microchannels. Flow manipulation can be done on the device itself for better signal detection. Delays can be implemented on the device for retaining a fluid in a chamber, proper mixing of the reagents via diffusion, to prevent a chamber from filling or draining and to stop the flow somewhere. This can be done using capillary stops as will be discussed with a case later. Since, the fluid needs to be transported via capillary action so the surface should be hydrophilic (fluid loving with contact angle less than 90°). The surface properties can be modified with different types of treatments and coatings (plasma treatment, PVD,CVD etc.) if needed. The design of the microchannels, surface properties, resolution and modification freedom are key parameters for choosing the correct fabrication scheme.

In the project "Printing Makes Sense", printing techniques like Plasma printing, inkjet printing and 3D printing were proposed to fabricate a POCT device for detecting CRP (C-reactive protien) antibody which can differentiate common cold from pneumonia.

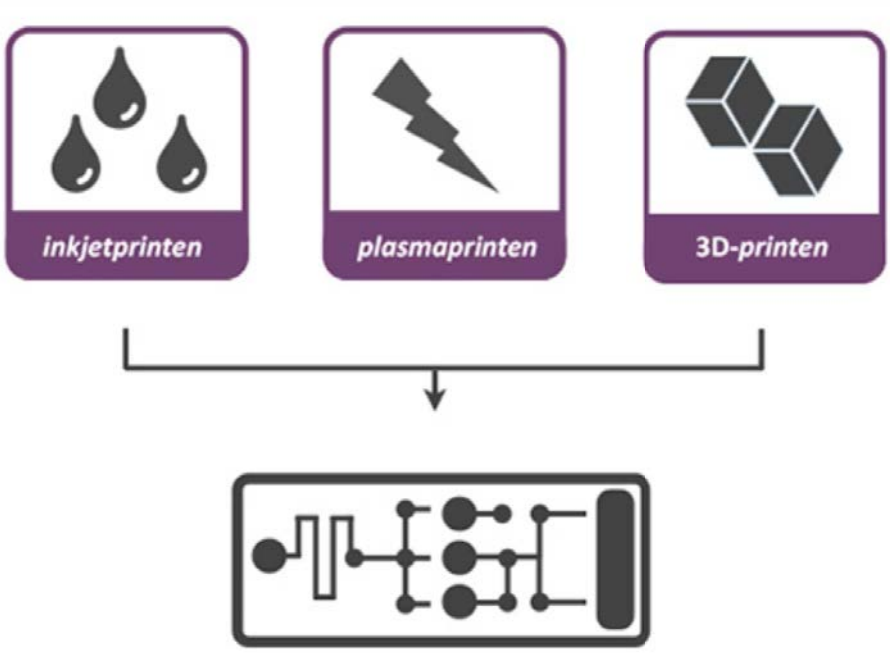

Figure A.4: Overview of the printing techniques from the RAAK-pro funded project "Printing Makes Sense".

Appendix B

Objet30 Prime

For this project the 3D printers present at Fontys University of Applied Science were used. The prints were first tested for resolution, surface roughness, wetting properties and optical transparency. Considering the requirements for the project Objet30 printer by Stratasys was used in the project for fabricating Microfluidic devices. The advantages of the Objet30 Printer are as follows:

- Better resolution in z-axis. This enables to print fine structures with minimal layer thickness.
- The prints are optically transparent with VeroClear resin
- Different print settings for different applications.
- The surface can be modified for better wetting with different coatings and surface treatments.
- The surface can be made more smooth and uniform using simple coatings.
- Post-processing of prints is simple and does not change the dimensions or structure of the prints.

Figure B.1: Objet30 Polyjet printer at Fontys Objex lab

The details about the resolution and different print settings have been explained briefly in the next

section B.1 and in the section B.4 the experiments conducted and results obtained with different print settings and surface treatments have been discussed.

B.1 VeroClear resin and Print Resolutions

VeroClear, a transparent PolyJet photopolymer, offers strength, stiffness and impact resistance ideal for concept modeling, design verification and functional testing of clear parts. VeroClear simulates PMMA (polymethyl methacrylate), commonly known as acrylic, and enables the visualization of internal components and features ideal for form and fit testing of see through parts such as eyewear, light covers and medical devices.
For this project a Microfluidic device with open microchannels is printed and then covered with a sealant. So, the need for proper cleaning and post processing treatments is not that crucial and for our purpose. Simple post-processign techniques like removing the support material by hand and then placing the prints in an alkaline solution (NaOH $2-4\%w/v$) is sufficient to dissolve the support material as explained next B.2. Figure B.2 shows the specifications of the Objet30 printer given by Stratasys Ltd. USA.

3D PRINTER SPECIFICATIONS	
Model Materials	Rigid Opaque: VeroWhitePlus™, VeroBlackPlus™, VeroGray™, VeroBlue™ Transparent: VeroClear™ Simulated Polypropylene: Rigur™ and Durus™ High Temperature
Support Material	SUP705 gel-like photopolymer support
Maximum Build Size (XYZ)	294 x 192 x 148.6 mm (11.57 x 7.55 x 5.85 in.)
System Size and Weight	82.6 x 60 x 62 cm (32.5 x 23.6 x 24.4 in.); 106 kg (234 lbs.)
Resolution	X-axis: 600 dpi; Y-axis: 600 dpi; Z-axis: 900 dpi
Accuracy	0.1 mm (0.0039 in.) varies depending on part geometry, size, orientation, material and post-processing method
Minimum Layer Thickness	28 microns (0.0011 in.); 16 microns for VeroClear material (.0006 in.)
Build Modes	High quality: 16-micron (.0006 in.) resolution High speed: 28-micron (.001 in.) resolution
Software	Objet Studio™ intuitive 3D printing software
Workstation Compatibility	Windows XP/Windows 7/Windows 8
Network Connectivity	Ethernet TCP/IP 10/100 base T
Operating Conditions	Temperature 18-25°C (64-77°F); relative humidity 30-70%
Power Requirements	Single phase: 100-120V; 50-60Hz; 7A or 200-240V; 50-60Hz 3.5A
Regulatory Compliance	CE, FCC/RoHS

Figure B.2: Caption

B.2 Post Processing

After the parts have been taken out of the printer they are immersed in an alkaline solution made up of $2-4\%$ (w/v) NaOH solution. This is used for dissolving the support material as it is soluble in Alkaline solution. The excess support is flushed after rinsing the parts with water and clean drying them with air spray. Additional UV exposure is not necessary since the exposure is quite controlled in the printing process itself which is a plus point in Polyjet printing. The exposure to the UV light is controlled by the support material and this varies with the print settings.

B.3 Resolution

The resolution of the printer is quite fine as compared to other printing techniques. The z-axis resolution is around $30\mu m$ whereas for the x-axis and y-axis the resolution depends on the dots per inch of resin deposited and cured by the UV laser lamp, see figure B.2.

Print Settings There are two types of print settings for OBJET30 Printer namely:

- Glossy
- Matte

Further the prints can be printed in a High Quality or High Speed mode. High Quality prints are much more finer and more precise as compared to High Speed prints. The roughness and the differences in Optical Contact Angle with different surface treatments and print settings have been discussed in detail in the following section B.4 and 3.1.1.

B.4 Results for different Print settings and orientations

Variation in dimensions The parts printed with different print settings and orientations were studied under OLYMPUS BX-51 microscope and also Keyence VHX-5000 microscope. The variation in the dimensions and the surface structure were observed and taken into consideration for designing final microfluidic devices for testing the passive flow with different microfluidic features. The rectangular channels shown in the figure B.4 are $600\mu m$ and $700\mu m$ respectively. The measured widths are $660\mu m$ and $741\mu m$ respectively giving a variation of $6-10\%$. This is well documented [27].

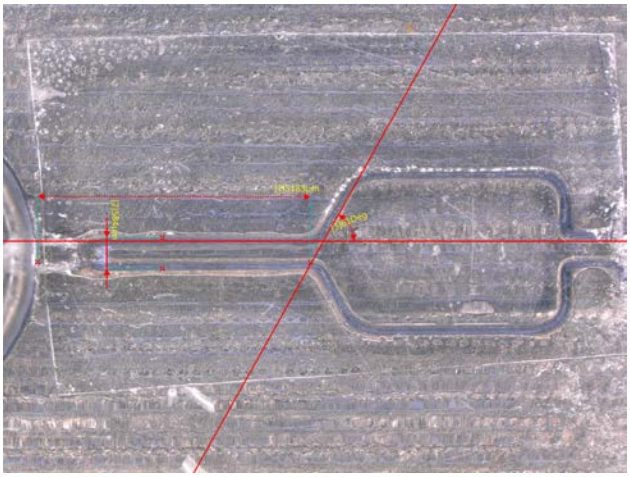

(a) 60° expansion with channel width measurements

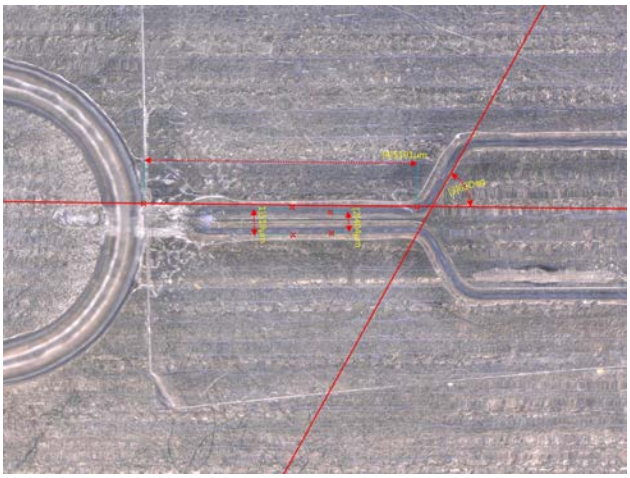

(b) 60° expansion with channel width measurements

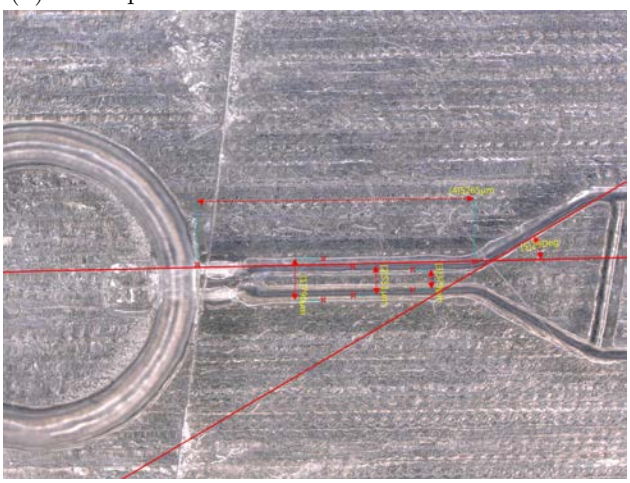

(c) 30° expansion with channel width measurements

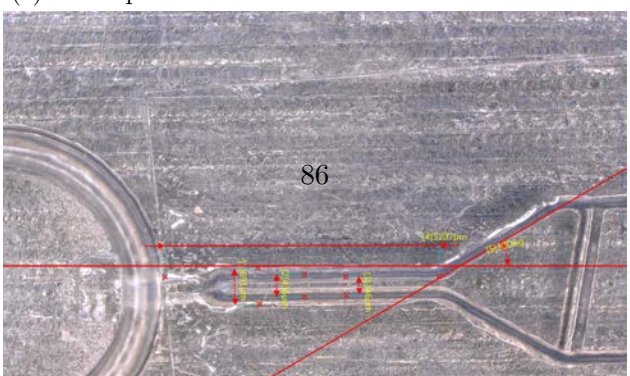

(a) The profile of the microchannel with rectangular cross-section

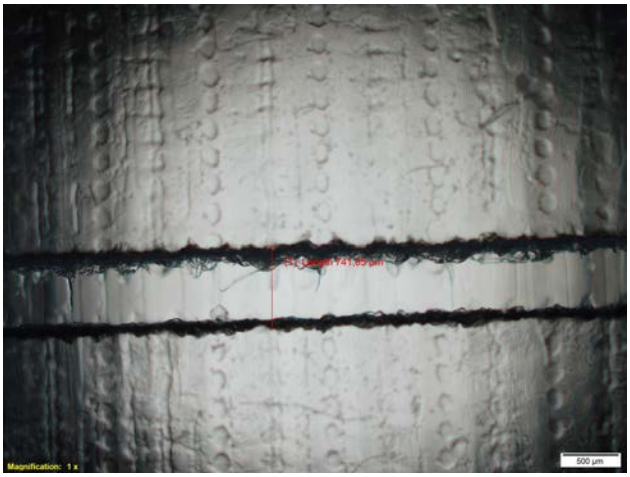

(b) The profile of the microchannel with rectangular cross-section

Figure B.4: Objet30 prints being measured under OLYMPUS BX-51 microscope

Glossy and Matte Glossy prints require less support material compared to Matte prints. Matte prints are useful for printing hollow and closed structure. Monolithic devices which do not require any external sealant can be printed well with Matte print settings. Removing excess support material trapped in the closed channels or holes is always a challenge. For microfluidic devices the excess support material clogs the Microchannels. GLossy prints on the other hand requires less support material and are printed fast as well compared to Matte prints.

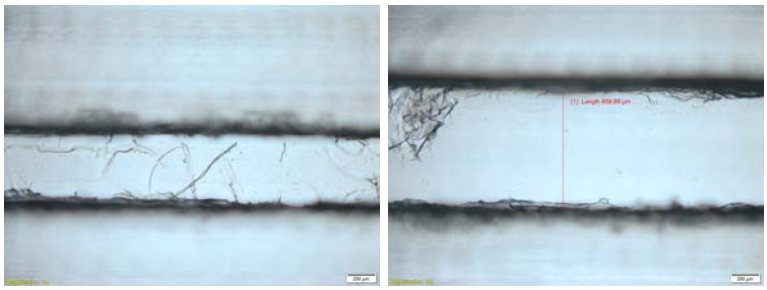

(a) 500μm channel printed with Matte setting

(b) 800μm channel printed with Matte setting

Figure B.5: Images of microchannels printed with Matte High quality settings taken with an Optical microscope (Olympus BX-51)

In figure B.5, we see that the channels still have little trapped support material. These prints haven't been put in an alkaline solution yet. These images show how the prints look like after taking out from the printer and rinsing with water. Compared to the prints shown in figure B.5 which were pritned with Matte settings the ones printed with Glossy print settings are shown below in figure B.6. The Glossy High Speed prints are clear of any support material since in Glossy High speed prints, no or minimal support material is used.

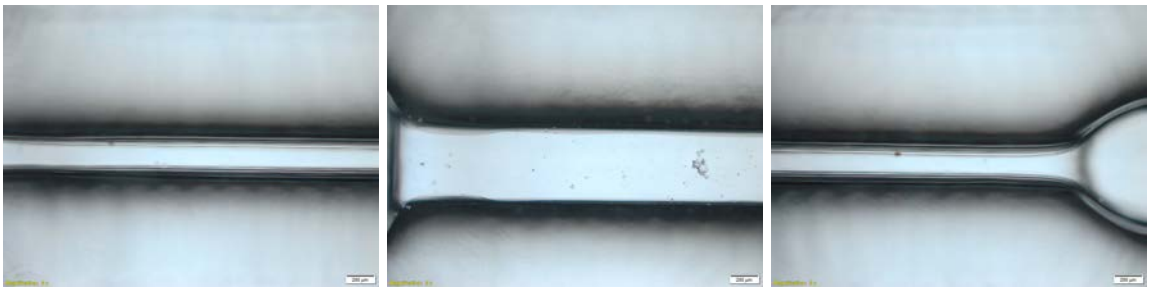

(a) Microchannel 1 printed with Glossy High Speed settings

(b) Microchannel 2 printed with Glossy High Speed Settings

(c) Microchannel 3 printed with Glossy High Speed setting

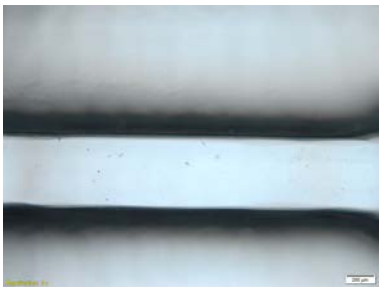

(d) Microchannel 4 printed with Glossy High Speed setting

Figure B.6: Objet30 prints being measured under OLYMPUS BX-51 microscope

After examining the 4 different combinations of prints namely:

- Glossy High Quality

- Glossy High Speed
- Matte High Quality
- Matte High Speed

It was observed that the ideal print and tray settings for this project would be Glossy High Quality. This is less support material is used as compared to Matte counterparts and also the intricate features like holes or reservoir channels are protected. The accuracy is also more in High Quality tray settings as compared to High Speed one. An example proving this finalization is that of Microfluidic device with a reservoir. The channel transporting the liquid from the reservoir goes through and underneath the walls of the reservoir as shown in figure B.7. When printed with Glossy High Speed setting the channels underneath the walls got polymerized and cured with UV light exposure as they were not shielded by support material. When printed with Glossy High Quality setting the channel underneath was open as it was shielded by the optimal support material. Hence, taking all these scenarios into consideration Glossy High Quality setting was used for fabricating the devices.

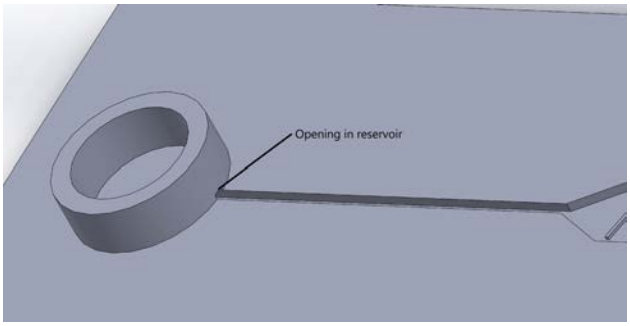

(a) $500\mu m$ wide channel with reservoir

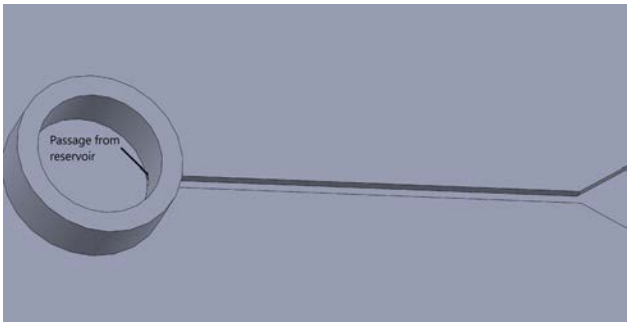

(b) Opening through the reservoir to transport fluid in the device

Figure B.7: CAD models printed for testing the best print setting for future designs

Orientation of Prints Different orientations of the prints were tested. The layer thickness for the prints is around $40\mu m$. When printed in horizontal orientation, the bottom surface of the channels and chambers has one layer because the depth does not vary however the walls of the channels and chambers have layer like structures. This gives rise to small capillaries on the wall. The fluid is also observed to flow faster via the walls and edges. When printed in vertical orientation

the walls are printed in one layer whereas the bottom surface where the liquid will be propagating has layered structure acting as small capillaries. The number of layers on the wall when printed in horizontal orientation is given by:

$$n = \frac{d}{t}$$

$$n = \text{Number of layers}, d = \text{Depth of microchannels}, t = \text{layer thickness}$$

The number of layers on the bottom surface of the mocrochannel or chamber is given by:

$$N = \frac{W}{t}$$

$$N = \text{Number of layers}, W = \text{Width of channel or chamber}, t = \text{Layer thickness}$$

Figure B.8a shows the design used for conducting these tests. The vertical and horizontal orientation used for doing these tests can be seen in figure B.8b.

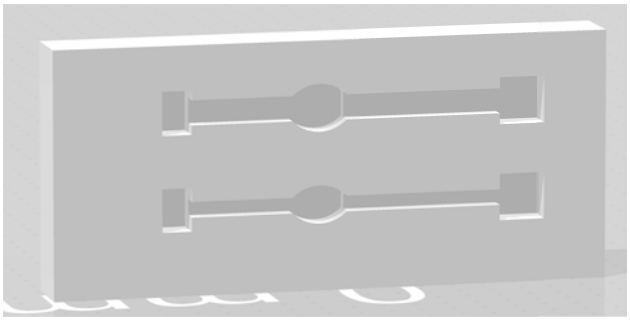

(a) Design used for conducting these tests

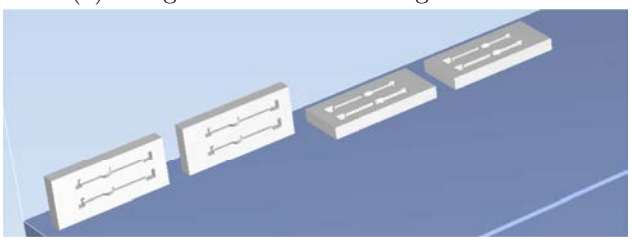

(b) parts lying in vertical and horizontal orientation on the tray

Figure B.8: Printing with different orientations

The printed parts were studied under Olympus BX-51 optical microscope to observe the structure on the channels and chambers. As can be seen in figure B.9, the parts printed in horizontal orientation have a single flat layer for the bottom surface whereas parts printed in vertical orientation as seen in figure B.10 have layer like structure on the bottom surface. This is the same for both Matte and Glossy print settings.

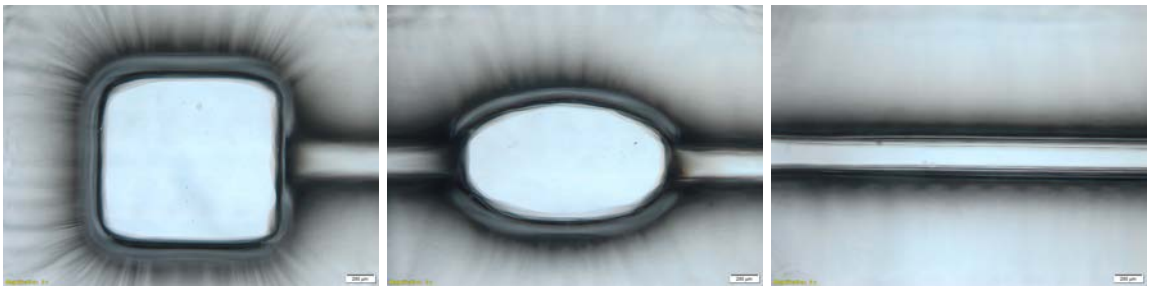

(a) chamber 1 (b) chamber 2 (c) channel 1

Figure B.9: Prints in Glossy print setting printed in horizontal orientation

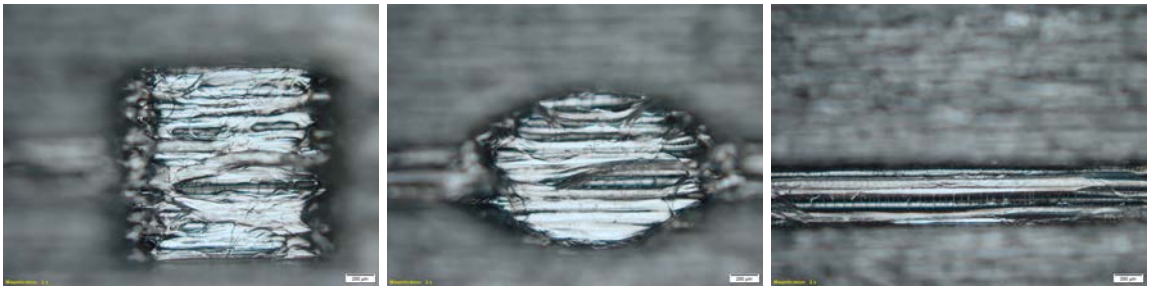

(a) chamber 1 (b) chamber 2 (c) channel 1

Figure B.10: Prints with glossy print setting printed in vertical orientation

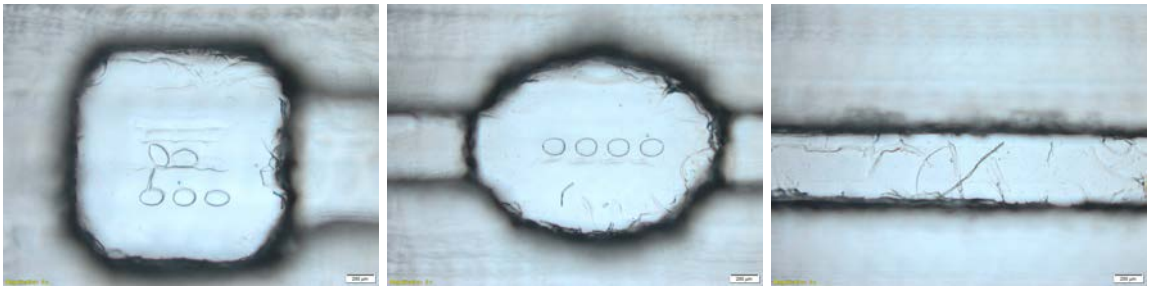

(a) chamber 1 (b) chamber 2 (c) channel

Figure B.11: Prints in Matte print setting printed in horizontal orientation

(a) chamber 1 (b) chamber 2 (c) channel 1

Figure B.12: Prints with Matte print setting printed in vertical orientation

B.4.1 Roughness

When OCA (optical contact angle) was measured on the VeroClear parts it was observed that the angle continuously decreases with time. This is because the parts seem to be quite rough. The OCA drop has been studied at different times and a plot is obtained as shown B.13.

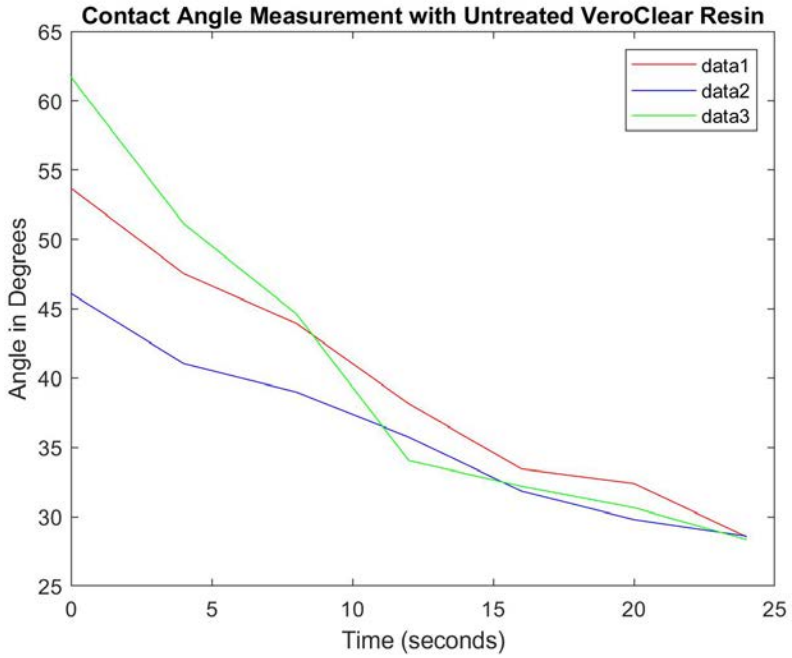

Figure B.13: Angle drop measured with water on VeroClear print

As, observed in the figure above B.13 the 3 different datasets from the measurements all converge to the same contact angle of around 28.5° with water. However this is not a reliable measurement result since the contact angle decreases further with time.

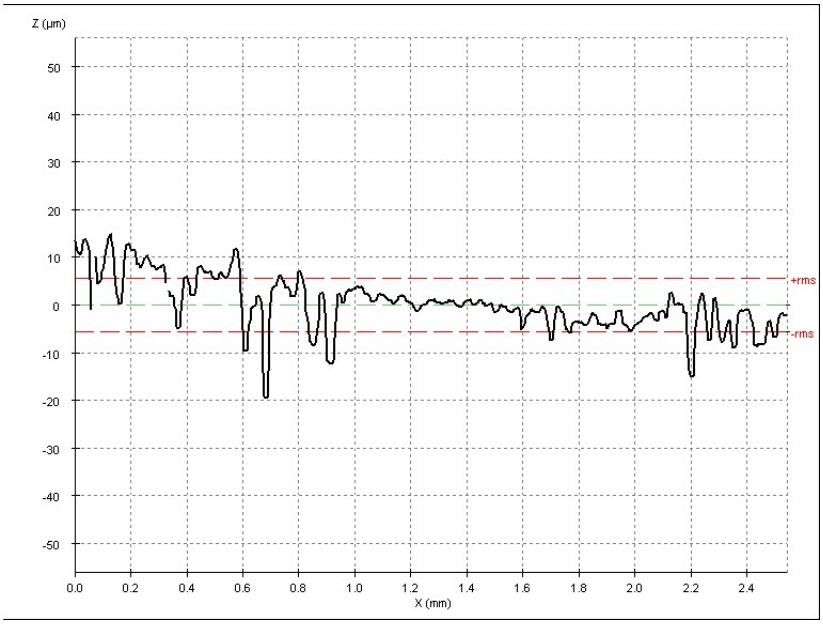

Figure B.14: Surface profile taken on top surface of a 3D printed block

Observations from Profilometery tests The samples were measured under a 3D optical profilometer (SensoFar-TNO) to know the roughness of the surface. The profile was chosen on the top surface and was measured over the entire length of the device.
As observed in figure B.14 the peaks range form -20μm to 15μm and the RMS value being approximately $5\mu m$.Due to this surface roughness we observe that the contact angle decreases continuously. Howevr when measured on the bottom smoother surface the R_a value is around $6\mu m$ indicating that the bottom surface where the fluid flows is quite smooth compared to the top surface.

Appendix C

Images for various results

C.1 Flow resistor Images

C.1.1 Flow resistors with width=$400\mu m$ and depth $500\mu m$

In this experiment the flow resistor structure as shown in the 3.4 section is used. The liquid is timed when it reaches the known lengths in the path of the channel of the flow resistor. Figure C.1a to C.1h shows the liquid at different positions at different times. These time values are used to calculate the length covered by the liquid in a straight channel of $400\mu m$ width and $500\mu m$ depth to give a comparison and to validate the application of flow resistors to make the flow of liquid really slow.

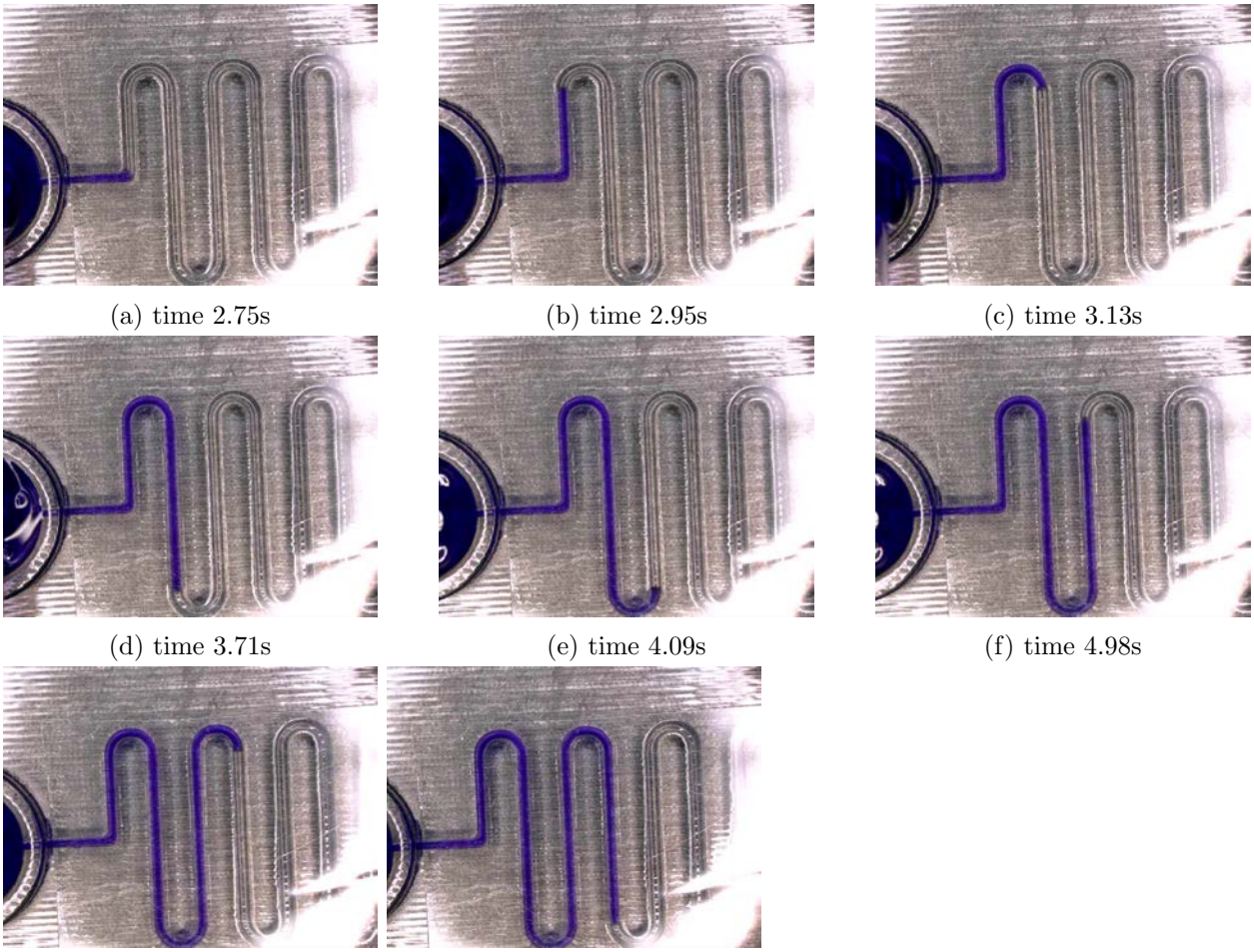

(a) time 2.75s (b) time 2.95s (c) time 3.13s

(d) time 3.71s (e) time 4.09s (f) time 4.98s

(g) time 5.78s (h) time 6.76s

Figure C.1: Liquid inside the flow resistor of $400\mu m$ wide channel progressing at different times

In figure C.2 comparison between the length covered by the liquid or the meniscus position with respect to time for flow in straight channels and that in flow resistors has been plotted. A Curve is also fitted onto the experimentally covered length to give a rough approximation of how the meniscus position will advance over time in future. The curve is fitted with linear regression of degree 2 since the meniscus position obeys Lucas-Washburn equation where $X \propto Time^{1/2}$, here X=meniscus position. This will give a rough approximation of how long this flow resistor channels should be to keep the reagents incubated for proper mixing to occur.

$$Time = 1.4153X^2 + 36.2742X - 0.5867$$

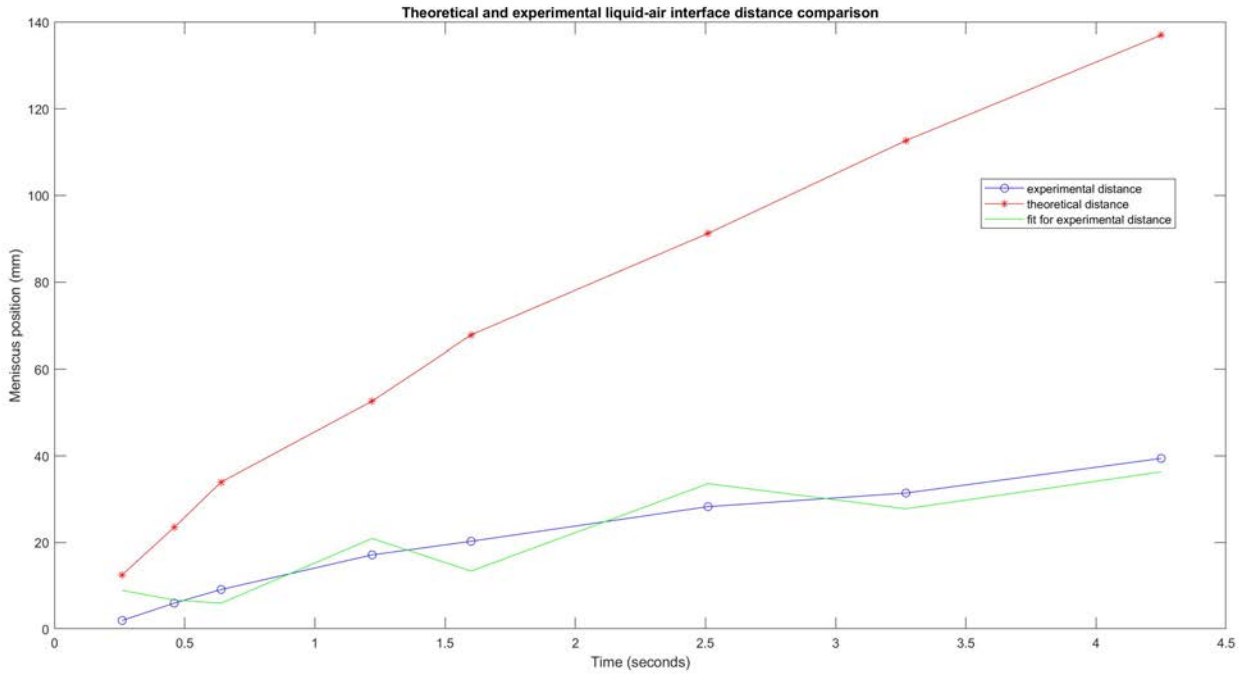

Figure C.2: Comparison between meniscus position in straight channel and flow resistor (experimental) with curve fitted onto the experimental plot of meniscus position

C.1.2 Flow resistors with width=$500\mu m$ and depth=$500\mu m$

Next, the flow resistors with width $500\mu m$ were tested. The meniscus position was recorded at different times where the liquid covered known lengths. The advancing meniscus position can be shown in figures C.3a to C.3i. These time values are then used to calculate the length covered by the liquid in straight square channel of width $500\mu m$. In figure C.4 a comparison is made between the meniscus position in straight channels calculated theoretically and that in the flow resistors determined experimentally. A curve is fitted by doing linear regression with degree 2 as discussed previously in accordance with the Washburn equation. The curve fitted on to the experimental plot of the meniscus position is:

$$Time = -8.315X^2 + 48.07X + 5.178$$

Here X= meniscus position in mm.

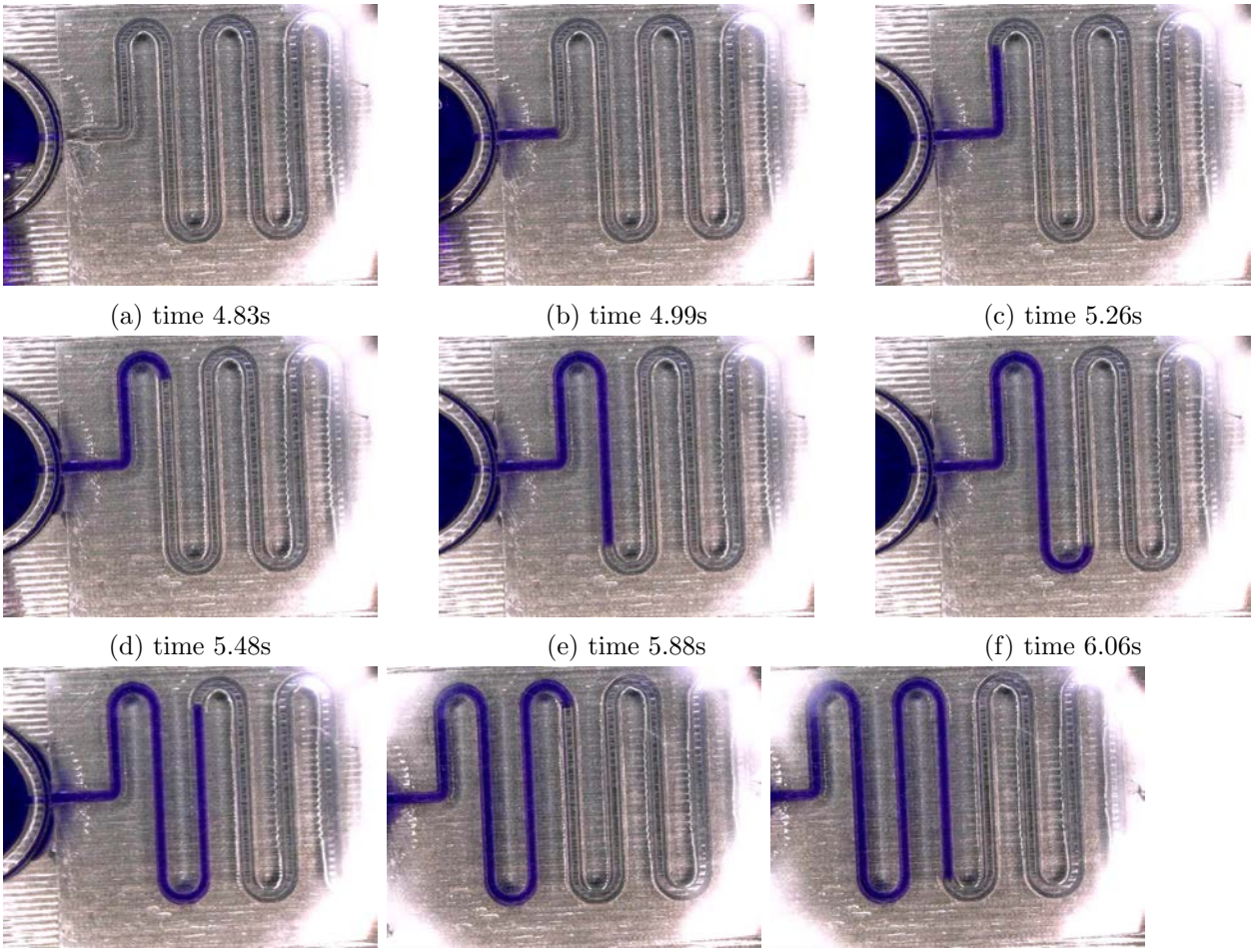

(a) time 4.83s (b) time 4.99s (c) time 5.26s

(d) time 5.48s (e) time 5.88s (f) time 6.06s

(g) time 6.70s (h) time 11.93s (i) time 12.85s

Figure C.3: Liquid inside the flow resistor of $500\mu m$ wide channel progressing at different times

It can be seen from figure C.4 that the curve fitted to the experimental plot is quite off but would be a good approximation to get a rough idea of how the liquid will propagate. With the same flow resistor design 3 independent experiments were done but the results obtained were quite aligned to each other.

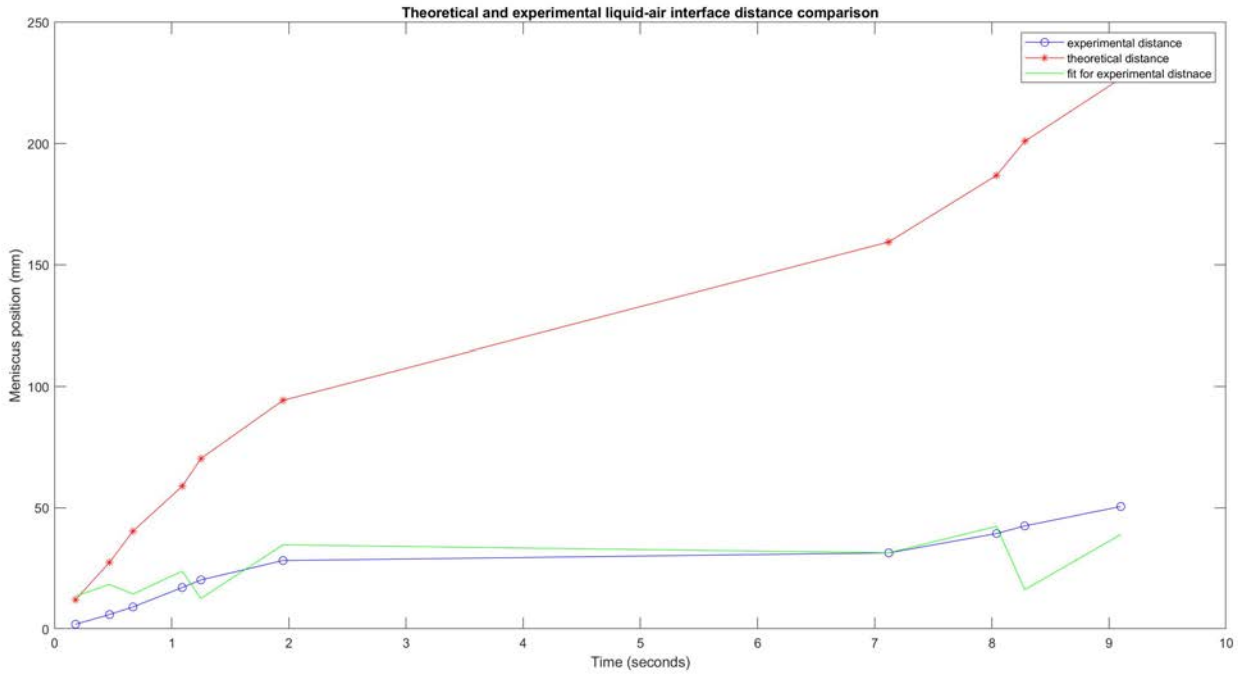

Figure C.4: Comparison between meniscus position in straight channel and flow resistor (experimental) with curve fitted onto the experimental plot of meniscus position

C.1.3 Flow resistors with width=$600\mu m$ and depth=$500\mu m$

In the last setting flow resistor with $600\mu m$ width is tested for comparing the advancing meniscus position at different times with flow in straight rectangular channel of the same width. Figures C.5a to C.5j show the advancing meniscus position at different times.In figure C.6 the meniscus position in flow resistors is plotted along with the theoretical calculation of the meniscus position in straight rectangular channels of $600\mu m$ width. A curve is also fitted to give an approximate prediction for future meniscus position with time. The equation for the curve fitted with linear regression is:

$$Time = -1.463X^2 + 15.203X - 0.435$$

here X=meniscus position in mm.

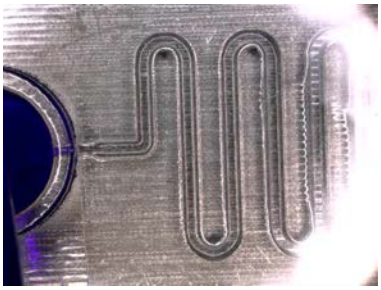

(a) time 3.33s

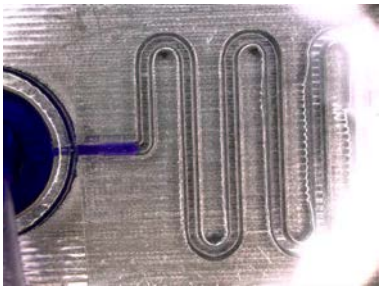

(b) time 3.77s

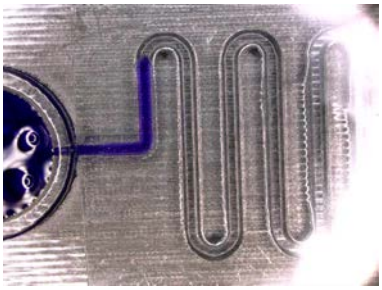

(c) time 5.0s

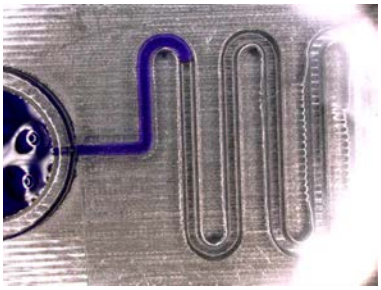

(d) time 5.72s

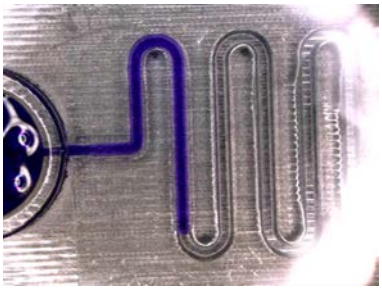

(e) time 6.62s

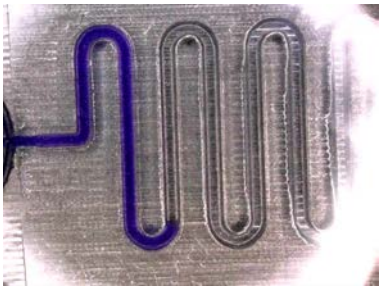

(f) time 6.06s

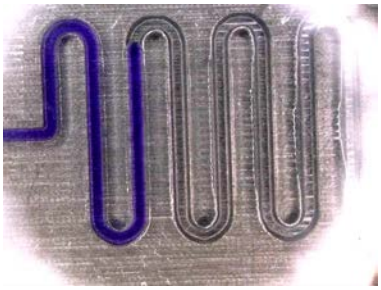

(g) time 9.89s

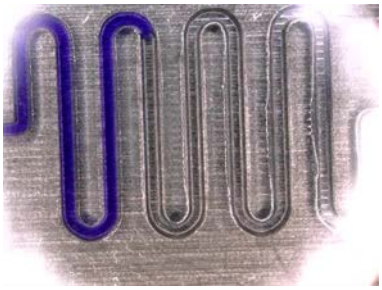

(h) time 17.26s

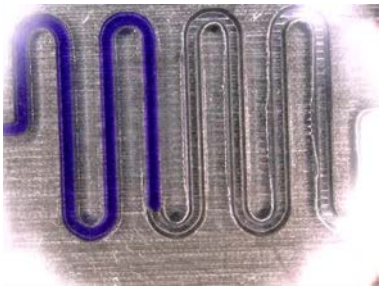

(i) time 22.15s

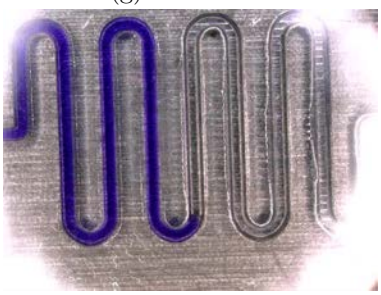

(j) time 24.64s

Figure C.5: Liquid inside the flow resistor of $600\mu m$ wide channel progressing at different times

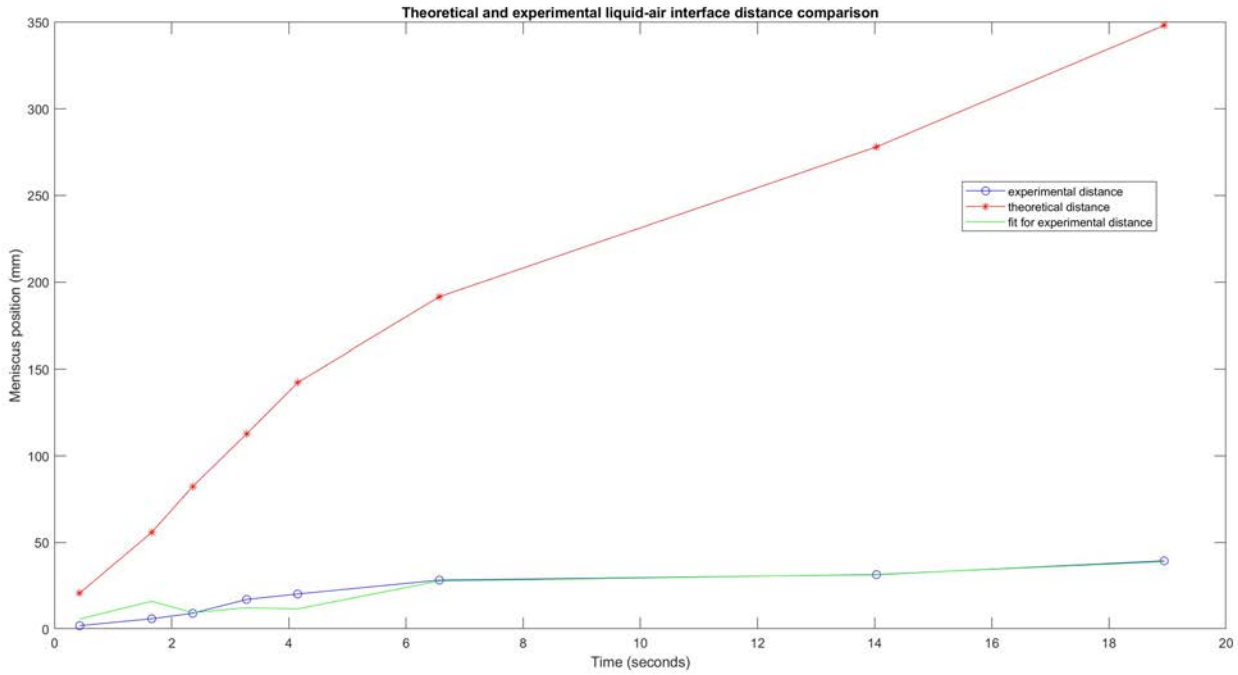

Figure C.6: Comparison between meniscus position in straight channel and flow resistor (experimental) with curve fitted onto the experimental plot of meniscus position

C.2 Images

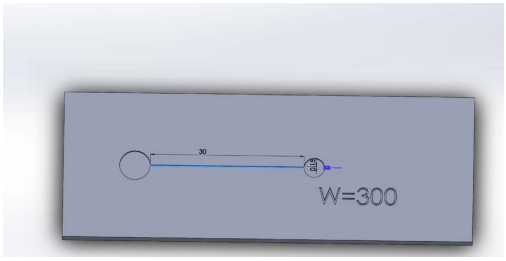

(a) Width 300μm

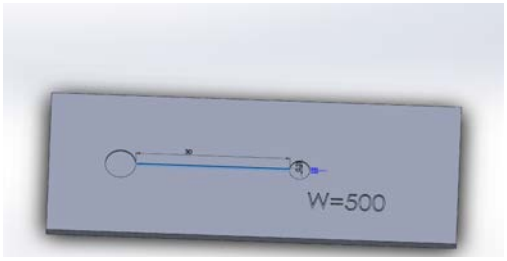

(b) Width 500μm

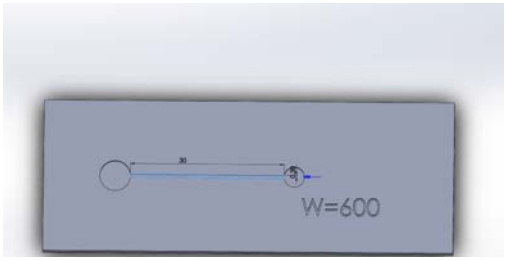

(c) Width 600μm

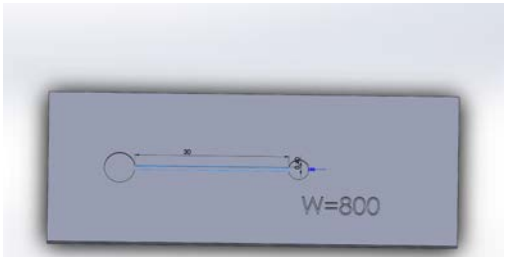

(d) Width 800μm

Figure C.7: Designs used for measuring flow in rectangular channels

(a) Microchannel with depth 500μm and width 600μm

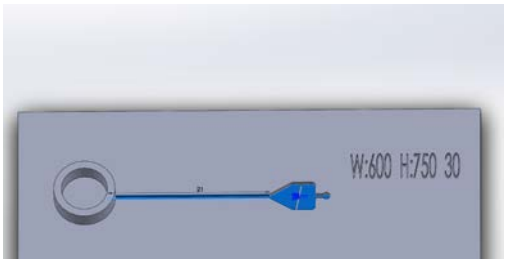

(b) Microchannel with depth 750μm and width 600μm

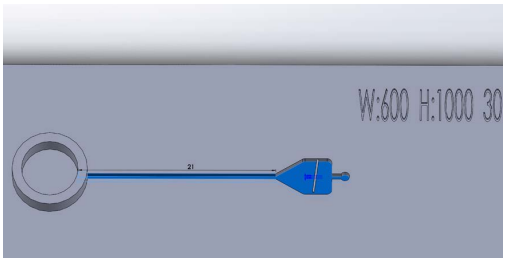

(c) Microchannel with depth 1000μm and width 600μm

Figure C.8: Microchannels with different depths

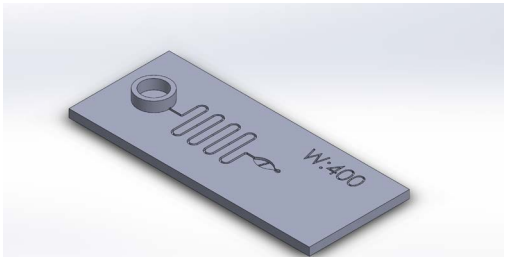

(a) Width 400μm

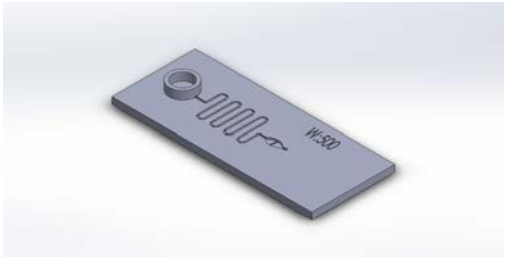

(b) Width 500μm

(c) Width 600μm

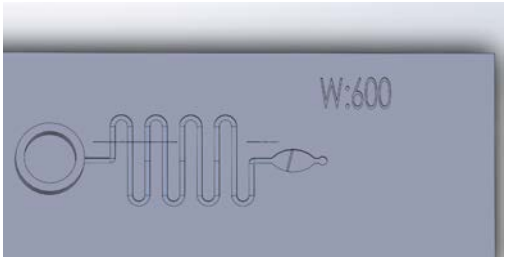

(d) The flow profile of the flow resistor

Figure C.9: Designs used for measuring flow in rectangular channels

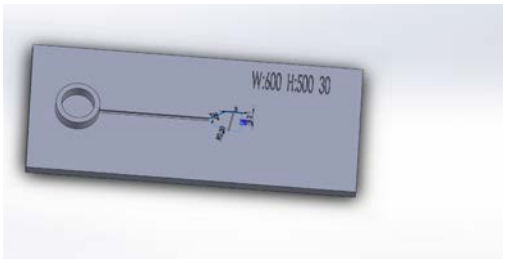

(a) Valve with $\beta = 30°$

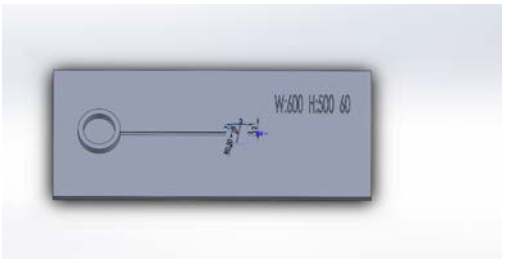

(b) Valve with $\beta = 60°$

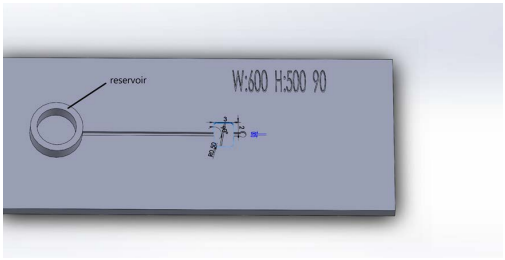

(c) Valve with $\beta = 90°$

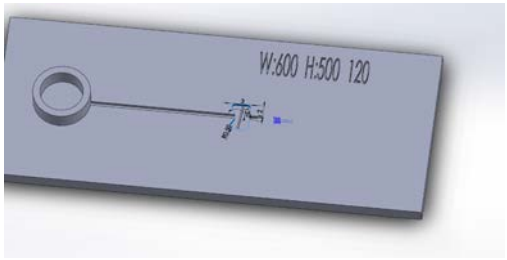

(d) Valve with $\beta = 120°$

Figure C.10: Geometrical expansion at X=21mm in the channel

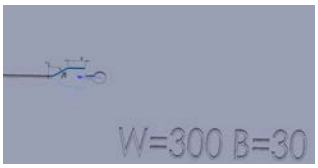

(a) Expansion $\beta = 30°$

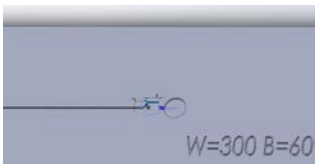

(b) Expansion $\beta = 60°$

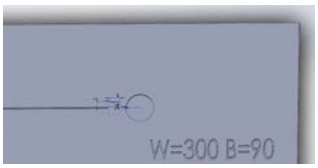

(c) Expansion $\beta = 90°$

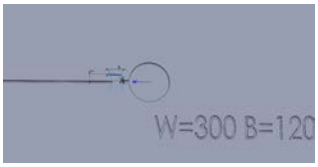

(d) Expansion $\beta = 120°$

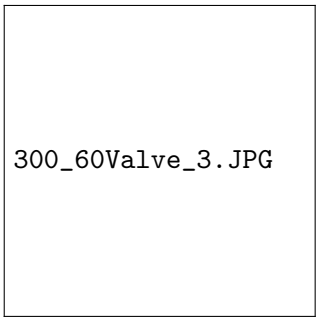

(e) Inlet and channel dimensions

Figure C.11: Valve designs with 300μm wide microchannels with geometrical expansion at L=30mm

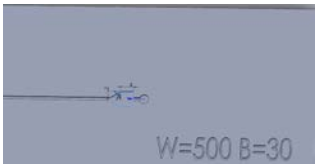

(a) Expansion $\beta = 30°$

(b) Expansion $\beta = 60°$

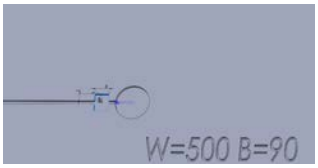

(c) Expansion $\beta = 90°$

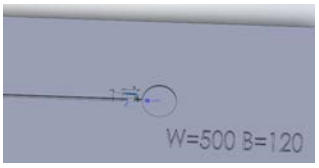

(d) Expansion $\beta = 120°$

(e) Inlet and channel dimensions

Figure C.12: Valve designs with $500\mu m$ wide microchannels with geometrical expansion at L=30mm

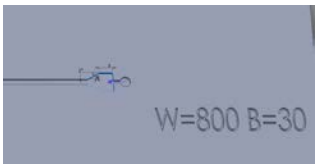

(a) Expansion $\beta = 30°$

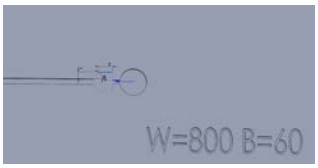

(b) Expansion $\beta = 60°$

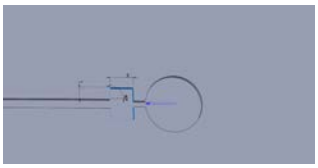

(c) Expansion $\beta = 90°$

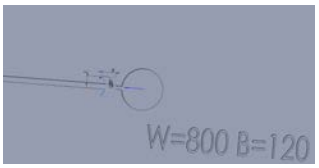

(d) Expansion $\beta = 120°$

(e) Inlet and channel dimensions

Figure C.13: Valve designs with $800\mu m$ wide microchannels with geometrical expansion at L=30mm

C.3 valves 3mm

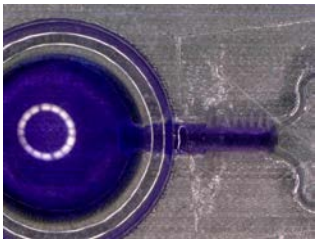

(a) time=40.5s

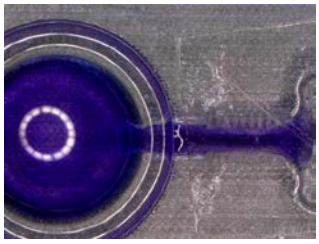

(b) time=41.14s

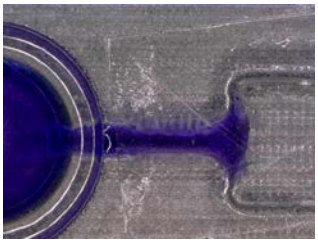

(c) time=56.3s

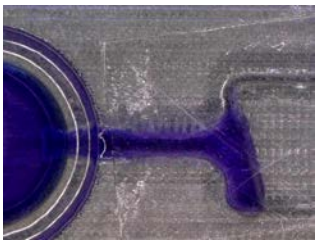

(d) time=63.58s

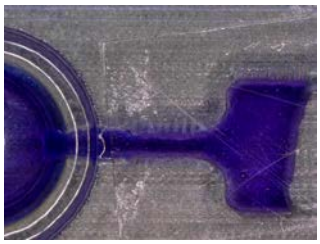

(e) time=64.53s

Figure C.14: Valve with $\beta = 90°$ with expansion at x=3mm